JAIST Repository
https://dspace.jaist.ac.jp/

Title	光熱免疫療法のための生物模倣ナノ複合体の開発
Author(s)	NINA, SANG
Citation	
Issue Date	2026-03
Type	Thesis or Dissertation
Text version	ETD
URL	https://hdl.handle.net/10119/20600
Rights	
Description	Supervisor: 都 英次郎, 先端科学技術研究科, 博士

JAIST
JAPAN
ADVANCED INSTITUTE OF
SCIENCE AND TECHNOLOGY

Japan Advanced Institute of Science and Technology

Doctoral Dissertation

Development of Biomimetic Nanocomplexes for Cancer Photothermal Immunotherapy

Sang Nina

Supervisor: Eijiro MIYAKO

Graduate School of Advanced Science and Technology

Japan Advanced Institute of Science and Technology

(Materials Science)

March 2026

Abstract

Cancer remains one of the leading causes of human mortality, resulting in nearly ten million deaths each year. According to global statistics, approximately one in ten people die from cancer, and this proportion continues to rise. The high incidence and fatality rates of cancer impose a heavy economic burden on families and public healthcare systems and represent a major barrier to the extension of human lifespan. Although conventional treatment modalities—including surgery, radiotherapy, chemotherapy, endocrine therapy, and immunotherapy—have achieved certain efficacy in early-stage or non-metastatic tumors, challenges such as drug resistance, recurrence, and metastasis persist, keeping the mortality rate alarmingly high. Therefore, developing more effective therapeutic strategies to achieve complete tumor eradication, suppress metastasis, and prolong patient survival remains of great significance.

In recent years, photothermal immunotherapy (PTI) which integrates photothermal therapy (PTT) with immunotherapy—has emerged as a highly promising strategy for the treatment of malignant tumors. PTT employs materials with high photothermal conversion efficiency to convert near-infrared (NIR) light energy into heat, thereby enabling localized ablation of tumor tissues. However, even materials with excellent photothermal properties, such as carbon nanotubes and liquid metals, suffer from poor solubility, strong aggregation tendency, and lack of efficient tumor-targeted delivery, which greatly hinder their biomedical applications. To address these challenges, biomimetic membrane modification has been

proposed as an effective approach. Coating photothermal materials with biologically derived membranes rich in phospholipids and proteins (e.g., cell membranes or plasma membranes) can markedly improve their dispersibility and biocompatibility, while conferring immune evasion and active tumor-targeting capabilities—thereby enhancing their therapeutic performance and in vivo stability.

Furthermore, the construction of biomimetic nanoplatforms provides new opportunities for multimodal synergistic therapy. When combined with chemotherapy, these platforms can improve the selective delivery and antitumor efficacy of drugs. When integrated with immunotherapy, they can effectively activate and sustain systemic antitumor immune responses, induce long-term immune memory, and consequently inhibit tumor recurrence and metastasis. Based on these insights, This dissertation focuses on the construction of multifunctional nanoplatforms based on biomimetic strategies, aiming to enhance tumor targeting, therapeutic efficacy, and immune activation through photothermal–immunotherapy synergy. A series of multimodal nanocomplexes derived from carbon-based and liquid metal (LM) materials were systematically developed for effective cancer treatment.

In the first part, a tumor cell–membrane–coated biomimetic carbon nano horn (CNH) nanoplatform loaded with paclitaxel (PTX) was fabricated to achieve combined photothermal therapy, chemotherapy, and immunotherapy for colorectal cancer. The platform exhibited excellent photothermal conversion efficiency under near-infrared irradiation, enabling light-controlled drug release and precise tumor ablation. Moreover, the membrane coating markedly

improved colloidal stability, immune evasion, and tumor-targeting capability, while its intrinsic components helped activate certain antitumor immune responses.

In the second part, a bacteria-membrane–wrapped liquid metal (LM) nanosystem was developed, which effectively improved LM dispersibility and reduced aggregation. Taking advantage of the bacterial membrane's adjuvant properties, this system significantly amplified immune activation and enhanced photothermal performance. The nanoplatform promoted dendritic-cell maturation and antigen presentation, strengthened systemic antitumor immunity, and achieved efficient tumor eradication and long-term immune protection through photothermal–immunomodulatory synergy.

In the third part, a whole-blood–camouflaged LM nanoplatform (B–LM–DMX–αCD25) was designed by co-loading the STING agonist DMXAA and anti-CD25 antibody for efficient photothermal immunotherapy of triple-negative breast cancer (TNBC). This multifunctional system integrated Treg depletion, PTT-induced immunogenic cell death (ICD), and STING activation within a single nanoplatform, achieving cascade amplification of antitumor immunity. The coordinated mechanism effectively reprogrammed the immunosuppressive tumor microenvironment, resulting in complete regression of orthotopic TNBC and significant inhibition of lung metastasis.

In summary, this dissertation proposes a systematic design strategy for biomimetic functional nanoplatforms that integrate photothermal effects with immune modulation, providing a new theoretical and technological foundation for the development of efficient,

controllable, and low-toxicity cancer therapies.

Keywords: Cancer therapy, Biomimetic nanoplatforms, Photothermal immunotherapy, Carbon nanohorns; Liquid metal nanoparticles.

Referee-in-chief: Prof. Dr. Eijiro MIYAKO

Japan Advanced Institute of Science and Technology (JAIST)

Referees: Prof. Dr. Kazuaki MATSUMURA

Japan Advanced Institute of Science and Technology (JAIST)

Prof. Dr. Motoichi KURISAWA

Japan Advanced Institute of Science and Technology (JAIST)

Prof. Dr. Takumi YAMAGUCHI

Japan Advanced Institute of Science and Technology (JAIST)

Prof. Dr. Naoki TAKAYA

University of Tsukuba (UTsukuba)

TABLE OF CONTENTS

LIST OF FIGURES

LIST of TABLES

Chapter 1 General introduction.

1.1 Introduction

1.1.1 Cancer epidemiology and therapeutic challenges

Cancer has become one of the leading causes of death worldwide, with both incidence and mortality rates continuing to rise over the past decades. According to the latest data released by the International Agency for Research on Cancer (IARC), a branch of the World Health Organization (WHO), there were approximately 20 million new cancer cases and 9.7 million cancer-related deaths globally in 2022, with around 53.5 million individuals surviving five years after diagnosis. Epidemiological data indicate that nearly one in five people will develop cancer during their lifetime, and one in nine men and one in twelve women will die from the disease, reflecting the high prevalence of cancer and its substantial burden on global public health[1].

In terms of cancer types, lung cancer has long ranked first in global incidence, with approximately 2.5 million new cases per year, accounting for 12.4% of all new cancer cases worldwide. Lung cancer is also a leading cause of cancer-related death and the most common cancer among men, with an estimated 1.8 million deaths (18.7%), followed by colorectal cancer (9.3%), liver cancer (7.8%), female breast cancer (6.9%), and stomach cancer (6.8%)[2]. Since 2020, breast cancer incidence among women has surpassed that of lung cancer, becoming the most frequently diagnosed cancer globally, with around 2.3 million new cases, accounting for 11.6%–11.7% of all cases. Breast cancer is not only among the most common cancers

worldwide but also a leading cause of cancer death in women, resulting in approximately 685,000 deaths, representing one-quarter of female cancer cases and one-sixth of female cancer deaths. Across 185 countries, breast cancer is the most common cancer among women in 159 countries and the leading cause of cancer death in 110 countries[3] Furthermore, cancer incidence and mortality vary significantly across regions and countries of different income levels. High-income countries generally have higher rates of early diagnosis and treatment accessibility, leading to relatively better five-year survival rates, whereas low-income countries face higher mortality due to limited medical resources, late diagnosis, and delayed treatment[2, 4].

The global cancer burden is expected to continue rising. By 2050, new cancer cases may exceed 35 million every year, representing an approximately 77% increase compared to 2022, with cancer-related deaths nearly doubling[5]. This growth is closely linked to population aging and also reflects the impact of lifestyle changes, environmental pollution, and an increasing prevalence of chronic diseases. Age remains the primary risk factor for cancer, with the majority of cases occurring in individuals over 50 years old, though the rising incidence among younger populations is also a growing concern[1]. In addition, tumor heterogeneity and increased treatment resistance complicate therapy, as recurrence and metastasis remain the leading causes of death even after standard treatments such as surgery, chemotherapy, or radiotherapy. Conventional therapeutic approaches generally suffer from low selectivity, high systemic toxicity, and limited efficacy against micrometastases, with these limitations[6] particularly pronounced in patients with recurrent or metastatic disease.

Therefore, given the increasing global cancer burden and the limitations of existing treatment modalities, the development of affordable, highly effective, and widely applicable novel therapeutic strategies has become an urgent need.

1.1.2 Cancer treatment and management

Currently, the most widely employed conventional cancer therapies include surgery, chemotherapy, and radiotherapy. These strategies can be applied individually or in combination, either concurrently or sequentially, depending on tumor stage, resectability, biological characteristics, comorbidities, and the overall functional status of the patient. Surgical resection is generally the preferred approach for early-stage tumors, whereas radiotherapy and chemotherapy play critical roles in curative, adjuvant, or palliative settings[7].

Chemotherapy employs various cytotoxic agents to inhibit tumor cell survival through mechanisms such as blocking DNA and RNA synthesis, disrupting mitosis, or forming covalent bonds with nucleic acids and proteins to interfere with proliferative processes[8]. Cytotoxic chemotherapy has been widely applied in adjuvant, neoadjuvant, and palliative contexts, effectively controlling tumor progression and improving patient quality of life. However, its limitations are evident: the non-specific effects on normal rapidly proliferating cells often result in severe adverse effects and systemic toxicity, imposing significant physical and psychological burdens on patients and, in some cases, potentially promoting tumor progression[9-11].

To overcome the limitations of conventional chemotherapy, targeted small-molecule drugs have been developed in recent years. These agents selectively inhibit key signaling pathways

involved in tumor growth, proliferation, and survival, thereby enhancing therapeutic efficacy while reducing toxicity[12]. Furthermore, the focus of cancer drug development has gradually shifted from directly suppressing tumor cell function—such as blocking neoantigen generation or cell surface receptor signaling—toward indirectly inhibiting tumors by modulating host immune responses[13]. For example, antibody-drug conjugates (ADCs) combine the targeting specificity of monoclonal antibodies with cytotoxic payloads, enabling precise delivery and tumor cell killing[14].

In addition to these approaches, modern therapies—including hormone therapy, anti-angiogenic therapy, immunotherapy, cell-based therapy, and gene therapy—are continuously evolving and being optimized[15] With technological advancements, the design and synthesis of novel anticancer agents have become increasingly sophisticated, accompanied by more advanced drug delivery platforms. Addressing the clinical challenges of cancer metastasis and recurrence, treatment paradigms are progressively shifting from monotherapies to multimodal combination strategies[16]. Looking ahead, the development of innovative therapies that combine high efficacy with low toxicity while meeting individualized and precision medicine requirements remains a central challenge in the field of cancer treatment.

1.1.3 Immunotherapy

The adaptive and innate immune systems work in concert to perform immune surveillance during tumor development and regulation. Upon receiving tumor antigen signals, immune cells can recognize and eliminate malignant cells. Innate immune cells—including natural killer

(NK) cells, eosinophils, basophils, and phagocytes—participate in tumor suppression either by directly killing tumor cells or by triggering adaptive immune responses. The adaptive immune system, primarily mediated by B and T lymphocytes, contributes through humoral and cell-mediated immunity, with B cells mainly responsible for antibody production and T cells for cytotoxic responses[17].

In recent years, cancer immunotherapy has emerged as a breakthrough treatment modality following surgery, radiotherapy, and chemotherapy. By activating or reprogramming the host immune system, immunotherapy enables recognition and clearance of tumor cells[18]. Early immunotherapeutic approaches primarily utilized cytokines and tumor vaccines to stimulate immune cell activity. For example, high-dose interleukin-2 (IL-2) and interferon-α2b (IFN-α2b) can elicit a range of downstream effects[19]. More recent strategies include immune checkpoint inhibitors (ICIs), adoptive cell transfer (ACT), oncolytic virus therapies, and next-generation tumor vaccines, representing a major advancement in the treatment of cancer.

Immune checkpoint inhibitors (ICIs) represent one of the most important modalities in cancer immunotherapy. Immune checkpoints are co-inhibitory signaling molecules that maintain immune tolerance, but they are frequently exploited by cancer cells to evade immune surveillance. ICIs aim to disrupt these co-inhibitory pathways, thereby relieving the suppression of effector T cells within the tumor microenvironment and promoting immune-mediated recognition and clearance of malignant cells. The most widely targeted immune checkpoints are cytotoxic T lymphocyte-associated antigen-4 (CTLA-4), programmed cell

death receptor-1 (PD-1), and programmed cell death ligand-1 (PD-L1)[20]22. CTLA-4 is an inhibitory receptor expressed on T cells, structurally similar to the co-stimulatory receptor CD28 but with higher affinity. CTLA-4 competes with CD28 for binding to B7 molecules (CD80/CD86) on antigen-presenting cells, thereby suppressing T cell activation and proliferation. Blocking CTLA-4 with monoclonal antibodies can induce robust immune responses and lead to tumor cell death, effectively “releasing the brakes” on immune cells to enhance antitumor immunity. The anti-CTLA-4 monoclonal antibody ipilimumab was approved by the FDA in 2011 for the treatment of advanced melanoma, becoming the first clinically approved immune checkpoint inhibitor[21].

Programmed cell death-1 (PD-1) was initially identified as a transmembrane protein on T cells involved in programmed cell death. Subsequent studies revealed that PD-1 is not merely a marker of cell death but a critical negative regulator of immune responses. Engagement of PD-1 with its ligand PD-L1 suppresses T cell proliferation, cytokine production, and cytotoxic activity, inducing T cell exhaustion and attenuating antitumor immunity[20]. PD-L1 is expressed in various normal tissues to maintain peripheral immune tolerance and prevent autoimmunity. However, in the tumor microenvironment, many malignant cells overexpress PD-L1 to exploit this regulatory mechanism and evade immune surveillance. Consequently, ICIs targeting the PD-1/PD-L1 pathway have emerged as one of the most groundbreaking antitumor therapies in recent years, demonstrating significant clinical efficacy in multiple cancers, including melanoma, non-small cell lung cancer, and renal cell carcinoma[22-24].

Adoptive cell transfer (ACT) refers to the therapeutic strategy of isolating immune cells from a patient or donor, expanding or genetically modifying them ex vivo, and reinfusing them into the host to enhance antitumor efficacy. Representative forms of ACT include tumor-infiltrating lymphocyte (TIL) therapy, chimeric antigen receptor T cells (CAR-T), T cell receptor-engineered T cells (TCR-T), and natural killer (NK) cell therapy[25]. TIL therapy involves the ex vivo expansion of tumor-resident, antigen-specific T cells and has demonstrated efficacy in certain solid tumors. In contrast, CAR-T and TCR-T rely on genetic engineering to enhance T cell recognition and cytotoxicity against specific tumor antigens. The most widely applied CAR-T target is CD19, a pan-B cell antigen, which has been developed into several approved therapies, including tisagenlecleucel and axicabtagene ciloleucel. Tisagenlecleucel is primarily used for refractory B-cell precursor acute lymphoblastic leukemia and diffuse large B-cell lymphoma, whereas axicabtagene ciloleucel is mainly indicated for relapsed/refractory diffuse large B-cell lymphoma[26-27]. NK cells possess the unique advantage of killing tumor cells without the need for antigen presentation[28].

In addition to ACT, oncolytic virus therapy selectively replicates within and lyses tumor cells while simultaneously activating systemic antitumor immune responses[29]. Tumor vaccines can induce long-term, antigen-specific immune surveillance[30-31]. Despite these advances, the clinical application of immunotherapy remains limited by the immunosuppressive microenvironment of solid tumors, immune-related adverse events (e.g., cytokine release syndrome), significant interpatient variability, and high manufacturing costs[32]. Tumor cells further exacerbate these challenges by downregulating antigen-presenting

machinery, upregulating inhibitory pathways, and recruiting immunosuppressive cell populations[33].

With the development of gene-editing technologies, advanced nano delivery platforms, and combination therapy strategies, these limitations are expected to be gradually overcome. Overall, cancer immunotherapy has not only significantly improved long-term survival for a subset of patients but has also advanced the paradigm of immunity-centered precision medicine, holding promise to become a central pillar in comprehensive cancer treatment in the future.

1.1.4 Tumor microenvironment (TME)

Studies have shown that the tumor microenvironment (TME) not only serves as a “fertile soil” for tumor growth but also represents a critical regulatory node for immunotherapy and targeted therapy. Detailed characterization of the TME, including its cellular composition, signaling networks, and dynamic changes, is essential for understanding mechanisms of tumor immune evasion and for optimizing immunotherapeutic strategies. Based on the infiltration patterns of cytotoxic immune cells, tumors can be classified as immunologically inflamed, immune-excluded, or immune-deserted. Inflamed tumors (“hot tumors”) typically exhibit high T cell infiltration, elevated PD-L1 expression, and high tumor mutational burden (TMB), and thus respond favorably to immune checkpoint inhibitors (ICIs). Immune-excluded tumors display cytotoxic T lymphocytes (CTLs) restricted to the tumor margin, resulting in poor infiltration into the tumor parenchyma. Immune-deserted tumors (“cold tumors”) are characterized by very low $CD8^+$ T cell density, insufficient antigen presentation, and low PD-

L1 expression, rendering them largely unresponsive to ICIs[34-35].

The hallmark of the TME is chronic inflammation, driven by sustained expression of pro-inflammatory cytokines and chemokines such as TNF-α, IL-6, and IL-1β. This chronic inflammatory milieu not only promotes tumor proliferation, invasion, and angiogenesis but also impairs effector T cell function through the recruitment of regulatory T cells (Tregs) and myeloid-derived suppressor cells (MDSCs)[36]. Immune cells within the TME exhibit substantial heterogeneity. For example, macrophages can polarize into antitumor M1 or protumor M2 phenotypes, with tumor-associated macrophages (TAMs) being key contributors to immunosuppressive TMEs. TAMs inhibit T cell activity through secretion of TGF-β and IL-10, recruit Tregs via chemokines such as CCL5, CCL20, and CCL22, and facilitate tumor invasion and metastasis by secreting matrix metalloproteinases (MMP2, MMP9) and urokinase-type plasminogen activator (uPA) to degrade the extracellular matrix[37]. MDSCs suppress T cell function by downregulating TCR ζ-chain, expressing high levels of arginase 1 (ARG1), producing nitric oxide (NO), and further enhancing immunosuppression through TGF-β signaling. Tregs in the TME similarly attenuate effector T cell function by secreting IL-10, IL-35, and TGF-β, as well as by competing for CD80/CD86 on antigen-presenting cells via CTLA-4[36, 38].

In summary, the TME constitutes a complex and dynamic immune regulatory network in which immunosuppressive cells and inflammatory factors collectively shape “cold tumors” or immune-resistant states. A thorough understanding of these mechanisms and their targeted

modulation may provide novel strategies to reshape antitumor immune responses and improve immunotherapy outcomes.

1.1.5 Photothermal therapy (PTT)

In recent years, photothermal therapy (PTT) based on photothermal agents has emerged as a promising approach to overcome the limitations of conventional cancer treatments. PTT exhibits high specificity, minimal invasiveness, prolonged therapeutic effects, and favorable safety profiles, which has garnered widespread attention[39]. Numerous nanomaterials have been engineered and applied for PTT, with functionalized nanomaterials demonstrating great potential in the development of selective and non-invasive cancer therapies. Although current research remains in its early stages, biological studies on PTT have already yielded encouraging results and progress.

Compared with ultraviolet (UV) and visible light, near-infrared (NIR) lasers offer deeper tissue penetration and are thus employed as non-invasive optical tools for imaging and light-mediated tumor therapy. Photothermal agents convert NIR laser irradiation into localized heat sufficient to induce irreversible damage to tumor cells. The NIR region, also known as the "biological window," is characterized by minimal absorption by water and biomolecules, allowing effective PTT application while sparing surrounding healthy tissues[40]. This strategy induces precise spatiotemporal heating, providing potent therapeutic effects against tumors situated in critical regions, and can be combined with existing treatment modalities to reduce adverse effects.

Photothermal agents (PTAs) are molecules or nanomaterials that exhibit high photothermal conversion efficiency (PCE) at therapeutic wavelengths, excellent biocompatibility (including minimal dark toxicity in non-irradiated tissues), and robust photostability. PTAs can generally be classified into the following categories: (i) organic dyes, such as indocyanine green (ICG) and heptamethine cyanines; (ii) organic nanoparticles, including semiconducting polymer nanoparticles and porphyrin–lipid conjugates; (iii) gold-based nanomaterials; (iv) carbon-based nanomaterials, such as carbon nanotubes and graphene oxide; and (v) other inorganic materials, including metal oxide nanoparticles and quantum dots.

Organic nanomaterials typically exhibit good biocompatibility and biodegradability; however, they have inherent limitations, such as relatively low photothermal conversion efficiency, poor photothermal stability, and complex synthesis[41]. In contrast, inorganic nanomaterials often display excellent NIR absorption due to their intrinsic optical properties, such as localized surface plasmon resonance (e.g., gold nanomaterials), narrow emission spectra, and facile surface functionalization with diverse groups including carboxyl, hydroxyl, and epoxy groups (e.g., carbon-based nanomaterials)[42]. These properties confer high photothermal efficiency and stability. Nevertheless, the non-biodegradability and potential long-term toxicity of inorganic nanomaterials remain unresolved challenges.

Mechanistically, PTAs act as photothermal enhancers to locally heat target cells or tissues. Upon irradiation with light of a specific wavelength, PTAs absorb energy and are excited from the ground singlet state to the excited singlet state. The excited-state PTAs then undergo non-

radiative vibrational relaxation, returning to the ground state through collisions with surrounding molecules. This process transfers energy to the local tumor microenvironment, elevating its temperature. PTT induces a variety of physiological and biological changes in tumor tissues[43]. On one hand, it can cause intracellular alterations such as DNA damage and protein denaturation[44]. On the other hand, localized heating enhances vascular and cellular membrane permeability, maximizing PTT efficacy and potentially increasing the accumulation of chemotherapeutic or other combination agents[40].

This underlies the promising synergy between PTT and chemotherapy, as each modality can overcome the limitations of the other. Chemotherapy efficacy is often hindered by tumor heterogeneity, drug resistance, lack of specificity, and systemic toxicity, whereas PTT alone cannot eliminate cancer cells outside the irradiated region, leaving residual cells that may metastasize or recurrence[45-46]. By combining chemotherapy with PTA-mediated PTT using biomimetic nanoparticles, one can achieve thermal ablation of tumor cells along with heat-triggered intratumoral drug release. This strategy allows lower drug doses to achieve satisfactory antitumor effects while minimizing dose-related side effects.

In addition, PTT itself can activate the immune system during tumor ablation by inducing danger signals from dying cells, making the combination of PTT and immunotherapy a topic of considerable interest. Numerous studies have demonstrated that PTT triggers immune responses through immunogenic cell death (ICD), thereby enhancing the efficacy of immunotherapy. This augmented immune response can be explained by several mechanisms:

(i) local immune cells effectively destroy tumor tissues, (ii) tumor-specific antigens are released and act as in situ vaccines, and (iii) pro-inflammatory cytokines activate the immune system[40, 47]. Nevertheless, these immune responses are often insufficient, and tumor recurrence and metastasis following PTT remain major challenges[48].

Based on these mechanisms, combining PTT with immunotherapy offers a promising strategy to modulate the immunosuppressive tumor microenvironment (TME) and overcome the recurrence and metastasis limitations of PTT monotherapy. A representative study developed a combinatorial therapeutic platform based on poly(lactic-co-glycolic acid) (PLGA) nanoparticles co-encapsulating the photothermal agent indocyanine green (ICG) and the Toll-like receptor 7 (TLR7) agonist imiquimod (R837). When combined with cytotoxic T-lymphocyte–associated antigen-4 (CTLA-4) checkpoint blockade, this platform integrates photothermal therapy with immune checkpoint inhibition. The PLGA-ICG-R837 nanoparticles, composed entirely of three clinically approved components, achieve efficient primary tumor ablation under near-infrared (NIR) laser irradiation while releasing large amounts of tumor-associated antigens. Under the immunostimulatory effect of R837, these antigens function as in situ vaccines, eliciting robust antitumor immune responses, effectively clearing residual tumor cells, inhibiting metastasis, and preventing recurrence. Importantly, this strategy can induce long-lasting immunological memory, providing durable protection against tumor re-challenge and demonstrating broad applicability across multiple tumor models[49]. Another study reported that PTT combined with single-walled carbon nanotubes and anti–CTLA-4 antibodies effectively suppressed secondary tumor growth and lung metastasis in mouse

models[50].

In summary, this combinatorial therapy does not simply reflect additive effects of individual modalities but represents a synergistic interaction. PTT enhances cellular uptake of nanomedicines and triggers localized drug release within the irradiated area, facilitating therapeutic delivery. Moreover, the release of tumor-specific antigens may further stimulate the integration of PTT and immunotherapy. Therefore, combining PTT with chemotherapy and immunotherapy not only overcomes the limitations of PTT alone but also fully exploits the advantages generated during PTT, thereby promoting other combinatorial treatment strategies and ultimately enhancing overall therapeutic efficacy.

1.1.6 Nanomedicine-based photothermal therapy

Despite significant advances in PTT for cancer treatment, PTT using only laser devices or non-specific small-molecule photothermal agents remains limited due to low photothermal conversion efficiency, concerns about biocompatibility of photothermal agents, low tumor accumulation, and thermoresistance in certain cancer types. The rapid development of nanotechnology has facilitated the broad application of PTT in cancer diagnosis and therapy. Using nanomaterials either as PTT photothermal agents or as carriers for PTAs can improve therapeutic outcomes and reduce side effects by enhancing photothermal conversion efficiency, increasing agent accumulation in tumor tissues, and enabling combination with other therapeutic modalities.

Nanomedicine is an emerging drug delivery system that leverages nanotechnology to

enhance drug bioavailability, stability, targeting, and therapeutic efficacy. These drugs typically refer to nanoscale (1–200 nm) carriers or molecules, including conventional small molecules, peptides, proteins, nucleic acids, or other bioactive compounds[51]. Compared with free-form drugs, nanomedicines offer several advantages, providing more effective drug delivery :1) Surface functionalization of nanomedicine: Physical and chemical modifications of nanoparticle surfaces can improve water solubility, stability, drug-loading capacity, tumor-targeting precision, and dispersion of photothermal materials[52]. 2) Passive and active targeting: Nanomedicines can passively accumulate in tumors via the enhanced permeability and retention (EPR) effect, overcoming targeting limitations of conventional photothermal agents. Through ligand–receptor interactions, nanoparticles can actively target tumor cells or TME components, offering higher photothermal conversion efficiency and enabling integration with multimodal imaging and diverse therapeutic functions for more effective cancer treatment[49]. Compared with early laser treatments, external laser-generated heat can damage surrounding healthy tissues, whereas functionalized nanoparticles convert specific light wavelengths into heat confined to the tumor, providing a more precise treatment[53].

Drug delivery: The high surface area of nanomaterials allows effective drug delivery. Photothermal nanoparticles can (i) improve cell membrane permeability; (ii) enhance drug cytotoxicity; and (iii) trigger site-specific drug release, facilitating the combination of PTT with other antitumor drugs[49, 54].

Many studies have demonstrated that, when combined with phototherapy or

chemotherapeutic drugs, nanomaterials enhance antitumor efficacy compared with PTT alone. Common nanomedicines used in tumor PTT include lipid-based nanoparticles, polymeric nanoparticles, and inorganic nanoparticles[51]. In a clinical study, researchers used laser-activated gold–silica nanoshells (GSNs) in combination with MRI–ultrasound fusion imaging to perform focal ablation of low- to intermediate-risk prostate tumors. Among 16 patients, after GSN injection and high-precision laser ablation, multiparametric MRI (mpMRI) was performed 48–72 hours post-treatment, and mpMRI/ultrasound-targeted fusion biopsies were conducted at 3 and 12 months. Results showed that 94% (15/16) of patients achieved successful GSN-mediated focal laser ablation, with no significant changes in International Prostate Symptom Scores (IPSS) or Sexual Health Inventory for Men (SHIM) before and after treatment. The procedure demonstrated good feasibility and safety, with no severe complications or impairment of genitourinary function[55]

Overall, compared with conventional therapies, nanomedicine provides a more reliable strategy for clinical translation of PTT, promoting the development of precise, low-toxicity, and efficient multimodal tumor therapies.

1.1.7 Biomimetic nanoparticles for targeted therapy

Another challenge in photothermal nanoparticle therapy is the limited biocompatibility of photosensitizers, as well as their lack of functional groups and poor bioavailability. Some photothermal materials, despite exhibiting high photothermal conversion efficiency, are restricted in application due to poor solubility, hydrophilicity, aggregation tendency, and

limited biocompatibility. Successful PTT relies on the sufficient accumulation of photoresponsive nanoparticles within tumors to achieve effective heating upon irradiation.

Traditional nanoparticles (NPs) are often coated with biologically inert polyethylene glycol (PEG), which provides spatial stability as a flexible polymer brush layer and reduces opsonization. Compared with unmodified NPs, PEGylation prolongs blood circulation half-life, reduces clearance by the mononuclear phagocyte system (MPS), and increases tumor delivery[56]. However, PEGylation can induce “anti-PEG” immune responses, leading to accelerated blood clearance (ABC), whereby a second dose of PEGylated NPs administered days after the first is rapidly removed from circulation[57]. Beyond potential immunogenicity, PEGylation achieves only passive tumor delivery, necessitating alternative coatings to improve NP specificity and tumor accumulation. Evidence suggests that, regardless of surface modification, only a limited fraction (<5%) of intravenously injected PEGylated NPs successfully reach tumors[58]. This suboptimal delivery may be due to conventional ligand–PEG strategies failing to recapitulate the abundance, diversity, and complexity of proteins on natural cell membranes, which are critical for enhanced target cell binding, leading to immune recognition and clearance.

To overcome these limitations, researchers have begun designing biomimetic nanoparticles using various cell membrane coatings. Cell membranes are extracted from desired cells in vitro and wrapped around the nanoparticle exterior to reduce opsonization and clearance while maximizing tumor delivery. Membrane-coated nanoparticles present a highly

complex combination of surface receptors, proteins, and phospholipids derived from natural cell membranes, enabling effective bio interfaces[59-61]. For example, red blood cell (RBC) membranes have been used to coat poly(lactic-co-glycolic acid) (PLGA) NPs, generating biomimetic NPs. Compared with PEGylated or uncoated controls, RBC-PLGA NPs exhibit significantly improved stability and prolonged blood circulation due to the presence of the CD47 "self-marker" protein, which inhibits phagocytosis by immune cells[58].

Building on biomimetic nanoparticles, surface modification with specific ligands based on target cell receptor expression can maximize active tumor targeting while minimizing clearance by the MPS[62-63]. For instance, macrophages express α4 integrin, which can actively bind to vascular cell adhesion molecule-1 (VCAM-1) overexpressed on MDA-MB-231 cells. In one study, gold nanodendrites (AuNDs) were loaded with ICG, coated with RAW 264.7 macrophage membranes, and further modified with the mitochondria-targeting cationic compound triphenylphosphonium (TPP). This strategy successfully delivered ICG specifically to the mitochondria of MDA-MB-231 human breast cancer cells, achieving PTT, photodynamic therapy (PDT), photoacoustic imaging, and fluorescence imaging, as well as effective laser-mediated PTT and PDT[64]. Other cell membranes, such as those derived from cancer cells, can also be used alone or in combination as coating sources, leveraging membrane-expressed proteins to facilitate cell–cell interactions, immune evasion, and active tumor targeting. Cell experiments have demonstrated that, compared with uncoated nanoparticles, membrane-coated nanoparticles exhibit improved circulation and tumor delivery, supporting efficient and effective photothermal therapy[60, 65]. Furthermore, PTT/chemotherapy

combination therapy mediated by biomimetic nanoparticles is highly effective. The membrane layer prevents premature drug release, enhances tumor delivery, and does not compromise photothermal conversion efficiency[59, 61]. These results indicate that biomimetic coatings can endow photothermal nanoparticles with greater tumor accumulation and broader combinatorial therapeutic potential, thereby enhancing overall therapeutic efficacy.

1.1.8 Purposes and outlines

This research is dedicated to the development of three representative biomimetic nanoplatforms that integrate photothermal therapy with immunomodulation to address the challenges of refractory malignancies. First, a tumor cell membrane–coated carbon nanohorn (CNH) nanoplatform encapsulating paclitaxel (PTX) is engineered to combine photothermal therapy, chemotherapy, and immunotherapy. By harnessing the exceptional photothermal conversion efficiency of CNHs under near-infrared irradiation, this system enables precise light-triggered PTX release, while the homologous tumor cell membrane coating improves dispersibility, promotes immune evasion, and facilitates tumor-specific accumulation, thereby enhancing the ablation of aggressive colorectal tumors and stimulating durable antitumor immunity. Second, to overcome the intrinsic instability and poor aqueous solubility of gallium-based liquid metals (LMs), we develop Lactococcus-functionalized LM nanocomposites (Lacto–LM) that leverage probiotic-derived components for improved stability, enhanced tumor localization, and high photothermal performance. Importantly, the Lactococcus constituents act as intrinsic immune adjuvants, amplifying host immune responses to achieve complete tumor regression after limited treatments and establishing long-lasting systemic

immune memory that prevents recurrence and metastasis. Third, we introduce blood plasma–camouflaged LM nanocomplexes conjugated with anti-CD25 antibodies and co-loaded with the STING agonist DMXAA for near-infrared II (NIR-II) photothermal immunotherapy of triple-negative breast cancer (TNBC). The plasma coating provides immune evasion, prolonged circulation, and efficient tumor accumulation, while the early release of anti-CD25 modulates regulatory T cells (Tregs) to relieve immunosuppression within the tumor microenvironment. Upon subsequent NIR-II laser irradiation, the LM nanocomplexes convert light into heat, inducing direct tumor ablation and promoting the release of tumor-associated antigens, which synergize with DMXAA to activate both innate and adaptive immune responses. Notably, this multifunctional platform not only eradicates primary orthotopic TNBC but also effectively suppresses lung metastasis, the most common metastatic pattern of TNBC. Collectively, these three strategies underscore the potential of biomimetic and multifunctional nanoplatforms to achieve localized tumor eradication, systemic immune activation, and durable protection against metastasis, thereby offering innovative and translatable therapeutic avenues for the treatment of aggressive and refractory cancers.

1.1.9 Reference

[1] F. Bray, M. Laversanne, H. Sung, J. Ferlay, R. L. Siegel, I. Soerjomataram, A. Jemal, *CA Cancer J. Clin.* **2024**, *74*, 229.

[2] W. H. Organization, Global cancer burden growing, amidst mounting need for services, https://www.who.int/news/item/01-02-2024-global-cancer-burden-growing--amidst-mounting-need-for-services, accessed: 10-18, 2025.

[3] A. M. Filho, M. Laversanne, J. Ferlay, M. Colombet, M. Piñeros, A. Znaor, D. M. Parkin, I. Soerjomataram, F. Bray, *Int. J. Cancer.* **2025**, *156*, 1336.

[4] H. Sung, J. Ferlay, R. L. Siegel, M. Laversanne, I. Soerjomataram, A. Jemal, F. Bray, *CA Cancer J. Clin.* **2021**, *71*, 209.

[5] I. A. f. R. o. C. (IARC), Global cancer burden in 2022, with projections to 2050, https://www.iarc.who.int/news-events/new-report-on-global-cancer-burden-in-2022-by-world-region-and-human-development-level/. accessed: 10.15, 2025.

[6] B. A. Chabner, T. G. Roberts, Jr., *Nat. Rev. Cancer.* **2005**, *5*, 65.

[7] T. P. Hanna, W. D. King, S. Thibodeau, M. Jalink, G. A. Paulin, E. Harvey-Jones, D. E. O'Sullivan, C. M. Booth, R. Sullivan, A. Aggarwal, *BMJ.* **2020**, *371*.

[8] M. T. C. Amjad, A.; Kasi, A., in *StatPearls [Internet]*, StatPearls Publishing, Treasure Island (FL) **2025**.

[9] W. M. van den Boogaard, D. S. Komninos, W. P. Vermeij, *Cancers (Basel).* **2022**, *14*, 627.

[10] J. D. Middleton, D. G. Stover, T. Hai, *Int. J. Mol. Sci.* **2018**, *19*, 3333.

[11] C. D'Alterio, S. Scala, G. Sozzi, L. Roz, G. Bertolini, presented at Semin. Cancer Biol. **2020**.

[12] C. Sawyers, *Nature.* **2004**, *432*, 294.

[13] I. Mellman, G. Coukos, G. Dranoff, *Nature.* **2011**, *480*, 480.

[14] A. Beck, L. Goetsch, C. Dumontet, N. Corvaïa, *Nature reviews Drug discovery.* **2017**, *16*, 315.

[15] B. Liu, H. Zhou, L. Tan, K. T. H. Siu, X.-Y. Guan, *Signal transduction and targeted therapy.* **2024**, *9*, 175.

[16] M. Vanneman, G. Dranoff, *Nat. Rev. Cancer.* **2012**, *12*, 237.

[17] G. P. Dunn, L. J. Old, R. D. Schreiber, *Immunity.* **2004**, *21*, 137.

[18] A. M. Eggermont, A. Spatz, C. Robert, *The Lancet.* **2014**, *383*, 816.

[19] S. A. Rosenberg, *The Journal of Immunology.* **2014**, *192*, 5451.

[20] S. L. Topalian, C. G. Drake, D. M. Pardoll, *Cancer Cell.* **2015**, *27*, 450.

[21] F. S. Hodi, S. J. O'Day, D. F. McDermott, R. W. Weber, J. A. Sosman, J. B. Haanen, R. Gonzalez, C. Robert, D. Schadendorf, J. C. Hassel, *N. Engl. J. Med.* **2010**, *363*, 711.

[22] S. Chen, Z. Zhang, X. Zheng, H. Tao, S. Zhang, J. Ma, Z. Liu, J. Wang, Y. Qian, P. Cui, *Front. Oncol.* **2021**, *11*, 562315.

[23] R. R. Munhoz, M. A. Postow, *The Cancer Journal.* **2018**, *24*, 7.

[24] T. Zhang, J. Xie, S. Arai, L. Wang, X. Shi, N. Shi, F. Ma, S. Chen, L. Huang, L. Yang, *Oncotarget.* **2016**, *7*, 73068.

[25] S. A. Rosenberg, N. P. Restifo, J. C. Yang, R. A. Morgan, M. E. Dudley, *Nat. Rev. Cancer.* **2008**, *8*, 299.

[26] S. L. Maude, T. W. Laetsch, J. Buechner, S. Rives, M. Boyer, H. Bittencourt, P. Bader, M. R. Verneris, H. E. Stefanski, G. D. Myers, *N. Engl. J. Med.* **2018**, *378*, 439.

[27] S. S. Neelapu, F. L. Locke, N. L. Bartlett, L. J. Lekakis, D. B. Miklos, C. A. Jacobson, I. Braunschweig, O. O. Oluwole, T. Siddiqi, Y. Lin, *N. Engl. J. Med.* **2017**, *377*, 2531.

[28] P. Jiang, S. Jing, G. Sheng, F. Jia, *Front. Immunol.* **2024**, *15*, 1420205.

[29] J. Martinez-Quintanilla, I. Seah, M. Chua, K. Shah, *The Journal of Clinical Investigation.* **2019**, *129*, 1407.

[30] Y. Zhou, Y. Wei, X. Tian, X. Wei, *J. Hematol. Oncol.* **2025**, *18*, 18.

[31] K. Peng, X. Zhao, Y.-X. Fu, Y. Liang, *Cell. Mol. Immunol.* **2025**, 1.

[32] J. Chu, F. Gao, M. Yan, S. Zhao, Z. Yan, B. Shi, Y. Liu, *J. Transl. Med.* **2022**, *20*, 240.

[33] K. Dhatchinamoorthy, J. D. Colbert, K. L. Rock, *Front. Immunol.* **2021**, *12*, 636568.

[34] S. Zheng, W. Wang, L. Shen, Y. Yao, W. Xia, C. Ni, *Experimental Hematology & Oncology.* **2024**, *13*, 80.

[35] B. Wu, B. Zhang, B. Li, H. Wu, M. Jiang, *Signal transduction and targeted therapy.* **2024**, *9*, 274.

[36] S. He, L. Zheng, C. Qi, *Mol. Cancer.* **2025**, *24*, 5.

[37] Y. Yang, S. Li, K. K. To, S. Zhu, F. Wang, L. Fu, *J. Exp. Clin. Cancer Res.* **2025**, *44*, 145.

[38] K. Park, M. S. Veena, D. S. Shin, *Frontiers in cell and developmental biology.* **2022**, *10*, 830208.

[39] D. Jaque, L. Martinez Maestro, B. del Rosal, P. Haro-González, A. Benayas, J. Plaza, E. Martín Rodríguez, J. Solé, *Nanoscale.* **2014**, *6*.

[40] Y. Cai, T. Chai, W. Nguyen, J. Liu, E. Xiao, X. Ran, Y. Ran, D. Du, W. Chen, X. Chen, *Signal Transduction and Targeted Therapy.* **2025**, *10*, 115.

[41] X. Dai, X. Li, Y. Liu, F. Yan, *Materials & Design.* **2022**, *217*, 110656.

[42] J. Chen, H. Yu, T. Zheng, X. Zhang, C. Chen, P. Sun, *RSC Advances.* **2025**, *15*, 15450.

[43] X. Cui, Q. Ruan, X. Zhuo, X. Xia, J. Hu, R. Fu, Y. Li, J. Wang, H. Xu, *Chem. Rev.* **2023**, *123*, 6891.

[44] H. S. Han, K. Y. Choi, *Biomedicines.* **2021**, *9*.

[45] J. Sun, H. Zhao, W. Xu, G.-Q. Jiang, *Frontiers in Chemistry.* **2022**, *10*, 1024177.

[46] J. Nam, S. Son, L. J. Ochyl, R. Kuai, A. Schwendeman, J. J. Moon, *Nat. Commun.* **2018**, *9*, 1074.

[47] O. Kepp, G. Cerrato, A. Sauvat, G. Kroemer, Vol. 11, Taylor & Francis, 2022, 2131227.

[48] Y. Hu, E. Qi, C. Yun, X. Li, F. Liu, Z. Cheng, N. Guan, Q. Wang, H. Zhao, W. Xiao, *J. Transl. Med.* **2025**, *23*, 271.

[49] Q. Chen, L. Xu, C. Liang, C. Wang, R. Peng, Z. Liu, *Nat. Commun.* **2016**, *7*, 13193.

[50] C. Wang, L. Xu, C. Liang, J. Xiang, R. Peng, Z. Liu, *Adv. Mater.* **2014**, 8154.

[51] J. Shi, P. W. Kantoff, R. Wooster, O. C. Farokhzad, *Nat. Rev. Cancer.* **2017**, *17*, 20.

[52] H. S. Han, K. Y. Choi, *Biomedicines.* **2021**, *9*, 305.

[53] X. Huang, P. K. Jain, I. H. El-Sayed, M. A. El-Sayed, *Nanomedicine.* **2007**, *2*, 681.

[54] E. Blanco, H. Shen, M. Ferrari, *Nat. Biotechnol.* **2015**, *33*, 941.

[55] A. R. Rastinehad, H. Anastos, E. Wajswol, J. S. Winoker, J. P. Sfakianos, S. K. Doppalapudi, M. R. Carrick, C. J. Knauer, B. Taouli, S. C. Lewis, *Proc. Natl. Acad. Sci.* **2019**, *116*, 18590.

[56] D. E. Owens III, N. A. Peppas, *Int. J. Pharm.* **2006**, *307*, 93.

[57] T. Ishida, M. Ichihara, X. Wang, K. Yamamoto, J. Kimura, E. Majima, H. Kiwada, *J. Controlled Release.* **2006**, *112*, 15.

[58] S. Wilhelm, A. J. Tavares, Q. Dai, S. Ohta, J. Audet, H. F. Dvorak, W. C. Chan, *Nature reviews materials.* **2016**, *1*, 1.

[59] C.-M. J. Hu, L. Zhang, S. Aryal, C. Cheung, R. H. Fang, L. Zhang, *Proc. Natl. Acad. Sci.* **2011**, *108*, 10980.

[60] R. H. Fang, A. V. Kroll, W. Gao, L. Zhang, *Adv. Mater.* **2018**, *30*, 1706759.

[61] Z. Chen, P. Zhao, Z. Luo, M. Zheng, H. Tian, P. Gong, G. Gao, H. Pan, L. Liu, A. Ma, *ACS nano.* **2016**, *10*, 10049.

[62] N. Bertrand, J. Wu, X. Xu, N. Kamaly, O. C. Farokhzad, *Adv. Drug Del. Rev.* **2014**, *66*, 2.

[63] F. Gallego-Gómez, A. Blanco, C. López, *Adv. Mater.* **2015**, *27*, 2686.

[64] J. Sun, J. Wang, W. Hu, Y. Wang, T. Chou, Q. Zhang, B. Zhang, Z. Yu, Y. Yang, L. Ren, *ACS Applied Materials & Interfaces.* **2021**, *13*, 10778.

[65] S. B. Aboeleneen, M. A. Scully, J. C. Harris, E. H. Sterin, E. S. Day, *Nano Convergence.* **2022**, *9*, 37.

Chapter 2 Biomimetic functional nanocomplexes for photothermal cancer chemoimmunotheranostics

2.1. Introduction

Carbon nanohorns (CNHs) have attracted considerable attention as photothermal therapy (PTT) agents due to their excellent biocompatibility and efficient photothermal conversion[1-3]. Structurally, CNHs consist of single graphene layers that form conical, horn-shaped tips. This unique morphology, together with their distinct surface chemistry, facilitates high drug-loading capacity and controlled drug release behavior. The conical structure of CNHs allows effective encapsulation of diverse therapeutic molecules, while their surfaces can be functionalized with targeting moieties, such as monoclonal antibodies or ligands directed against tumor-specific biomarkers[4-6]. These physicochemical properties collectively make CNHs promising candidates for cancer therapy.

Despite these advantages, several challenges hinder the clinical translation of CNHs. A major limitation is the relatively short systemic circulation time, which reduces delivery efficiency to target sites and compromises therapeutic efficacy. Bare CNHs, lacking functionalization or protective coatings, are prone to premature drug leakage prior to reaching tumor tissues, potentially causing off-target toxicity. Furthermore, immune system-mediated accelerated clearance further shortens their in vivo retention, limiting antitumor effectiveness[7-8]. Although polyethylene glycol (PEG) derivatives have been extensively employed to enhance nanoparticle circulation and biocompatibility[9], PEGylation carries the risk of eliciting immune responses, including the generation of anti-PEG antibodies, which restricts its clinical

utility[10]. To overcome these limitations, it is essential to develop facile and multifunctional surface modifications of CNHs with bioactive molecules. Moreover, the immunogenicity of CNHs can be strategically regulated through the incorporation of immunostimulatory antigens or molecular adjuvants, enabling a combined therapeutic approach that integrates immunogenic CNHs with PTT and chemotherapy—a strategy that remains underexplored in the context of carbon-based nanomaterials.

Recently, biomimetic surface engineering using cellular membranes has emerged as a promising alternative to conventional PEG coatings. This strategy allows the transfer of intact membranes, along with peripheral proteins, onto the nanoparticle surface, enhancing targeting efficiency and improving in vivo delivery[11]. Membranes derived from a variety of cells—including cancer cells, bacteria, and macrophages—have been utilized to functionalize nanoparticles for applications such as anticancer vaccination, antibacterial immunomodulation, and targeted drug delivery[12-15]. Among these, cancer cell membranes (CMs) are frequently employed as single-membrane coatings due to their dual ability to facilitate immune evasion and homotypic tumor targeting. Proteins involved in self-recognition on CMs are thought to mediate homotypic adhesion, a mechanism that reflects natural tumor cell aggregation during primary tumor formation and metastatic dissemination[16-17].Consequently, CM-coated nanoparticles have been widely investigated for diagnostics, therapeutics, and anticancer vaccine development[18]. The primary advantage of CM coating lies in the preservation of native cellular proteins, enabling the nanoparticles to exploit intrinsic biological functions that conventional nanoparticles lack. Nevertheless, the extraction and purification of structurally intact CMs remain complex, and critical immunogenic components, such as cytoplasmic

proteins and nucleic acids, are often lost during nanoparticle fabrication. Therefore, further optimization of CM-based nanomedicines, including multifunctionalization with additional therapeutic agents and nanomaterials, is necessary to fully realize their potential in innovative cancer therapies.

We first employed whole Colon26 cells in combination with carbon nanohorns (CNHs) to enhance both the immunological activity of CNHs and the delivery efficiency of the chemotherapeutic agent paclitaxel (PTX), thereby achieving improved antitumor efficacy through synergistic photothermal–chemo–immunotherapy. We hypothesized that CM-coated CNHs (CNH–CM) inherently replicate the surface characteristics of their source cells, conferring multiple advantageous properties, including excellent water dispersibility, superior biocompatibility, prolonged systemic circulation, enhanced tumor targeting, and the induction of systemic anticancer immune responses.

2.1 Objective of this chapter.

The objective of this chapter is to develop and evaluate a tumor cell membrane–coated biomimetic carbon nanohorn (CNH) nanoplatform encapsulating paclitaxel (PTX) for multimodal cancer therapy. CNHs are utilized for their exceptional photothermal conversion efficiency under near-infrared irradiation, enabling precise light-triggered drug release within the tumor microenvironment. The tumor cell membrane coating improves aqueous dispersibility, facilitates immune evasion, and supports active homologous targeting to malignant cells. Moreover, the coating derived from immunogenic Colon26 cells—comprising cellular membranes, cytoplasmic proteins, and nucleic acids—serves as a reservoir of tumor-

associated antigens, thereby functioning as potent immune stimulators to activate robust antitumor immunity within the tumor microenvironment. By integrating these features, this work aims to achieve localized tumor ablation and enhanced paclitaxel efficacy while simultaneously eliciting durable antitumor immunity, thereby providing a promising and translatable strategy for the treatment of refractory malignancies

2.2 Materials and methods

2.2.1 Nanocomplex synthesis

The PTX–CNH–CM complexes were prepared by mixing 1 mg of CNH (average diameter, ca. 80–100 nm; purity, 95%; metal-free, NEC Corporation, Tokyo, Japan), 2×10^7 Colon 26 cells, and 1 mg of PTX in 10 mL of PBS, followed by pulse-type sonication (VCX-600; Sonics, Danbury, CT, USA) for 10 min in an ice bath. The CNH–CM nanoparticles were prepared similarly but without the addition of PTX. A PTX solution was separately prepared by dissolving 1 mg of PTX in 10 mL of PBS with 10% cremophore and sonicating for 5 min in an ice bath. Similarly, a CNH–CRE solution was prepared by dispersing 10 mg of CNH in 10 mL of PBS with 10% Cremophore® EL (Nacalai Tesque, Kyoto, Japan) and sonicating for 10 min in an ice bath. Additionally, highly concentrated PTX–CNH–CM or PTX solutions were prepared by increasing the amounts of CNH and CM in the same ratio. The ICG–PTX–CNH–CM was prepared by mixing 1 mg of ICG (Tokyo Chemical Industry, Tokyo, Japan) with 1 mL of the prepared PTX–CNH–CM solution and vortexing for 1 min under dark conditions. The drug loading efficiencies of the PTX–CNH–CM and ICG–PTX–CNH–CM nanocomplex were assessed by calculating unbound PTX or ICG molecules after filtration using a UV–vis–NIR

spectrometer. Briefly, the prepared aqueous suspension of PTX–CNH–CM or ICG–PTX–CNH–CM was filtered with a hydrophilic polyvinylidene fluoride filter membrane [pore size = 0.22 μm; Vented Millex®-GV Filter Unit (Sterile), Merck Millipore, Darmstadt, Germany]. The filtrates were measured using a UV–vis–NIR spectrometer to identify unbound PTX or ICG molecules and calculate drug loading efficiencies from calibration carves of PTX and ICG.

2.2.2 Structural and optical characterizations

The structural morphology and composition of the PTX–CNH–CM, CNH–CM, and CNH were meticulously examined employing a high-resolution transmission electron microscope (HR-TEM) (Model JEM-2010; JEOL Ltd., Tokyo, Japan) operating at an acceleration voltage of 200 kV. These TEM investigations were conducted at the Hanaichi UltraStructure Research Institute Co., Ltd. in Aichi, Japan. DLS technology (Zetasizer Nano ZS; Malvern Panalytical, UK) was utilized to ascertain the hydrodynamic diameter and zeta potential of the nanoparticles. Additionally, the optical properties, specifically absorbance and FL, were characterized by deploying a UV–vis–NIR spectrophotometer (Model V-730 BIO; Jasco Corporation, Tokyo, Japan) and an FL spectrometer (Model FP-6300; Jasco Corporation, Tokyo, Japan), respectively. The amounts of CM and PTX conjugated with CNH were estimated by TG analysis (TG-DTA8122; Rigaku, Tokyo, Japan). The PTX–CNH–CM and CNH–CM were prepared as the same way as the mentioned above but using 0.1 mg of PTX. TGA traces were recorded for the series using a ramp rate of 5 °C/min in air. The PTX–CNH–CM and CNH–CM were synthesized by the same way as the above protocol of nanocomplex synthesis except for using distilled water instead of PBS. The powder PTX–CNH–CM and CNH–CM was prepared by a freeze dryer (FDU-1200; EYELA, Tokyo, Japan) before TG measurements.

2.2.3 Photothermal conversion efficacy

The photothermal transduction of PTX–CNH–CM nanoparticle dispersions was investigated by irradiating the solutions alongside MilliQ water with an 808 nm NIR laser (Civil Laser, Hangzhou, Zhejiang, China) at varying outputs of 1.2 W (approximately 61.1 mW/mm², spot diameter approximately 5 mm), 0.6 W (30.6 mW/mm²), and 0.3 W (15.3 mW/mm²). The thermal response of the solutions was continuously monitored in situ utilizing a high-precision temperature sensor (Model AD-5601A; A&D Company, Tokyo, Japan). Furthermore, infrared thermographic imaging was conducted (Model i7; FLIR Systems, Nashua, NH, USA) to visually record the thermal patterns.

To evaluate the photothermal stability of the PTX–CNH–CM complexes, a 200 μL aliquot of the nanocomplex suspension was exposed to an 808 nm NIR laser at an intensity of 1.2 W (equivalent to approximately 61.1 mW/mm², with a spot diameter of around 5 mm) for 5 min. Subsequent to irradiation, the suspension was diluted with MilliQ water, and the resultant solution's optical absorbance spectrum was analyzed using a UV–vis–NIR spectrophotometer.

Photothermal conversion efficiency of nanocomplex was determined according to the previous methods[19-21]. Detailed calculations were given as follows:

$$\eta = hS(T_{Max} - T_{Surr}) - Q_{Dis} / I(1 - 10^{-A_{808}}) \quad (1)$$

Where η is the photothermal conversion efficiency of nanocomplex, h is the heat transfer coefficient, S is the surface area of the container, and the value of hS is obtained from the Eq.2. T_{max} is the maximum steady temperature of the solution of the nanocomplex and T_{Surr} is environmental temperature. I and A_{808} represent the laser power and the absorbance at the used

laser wavelength (808 nm), respectively. Q_{Dis} expresses heat dissipated from the light absorbed by the solvent and container.

$$hS = m_D C_D / \tau_s \quad (2)$$

Where m_D and C_D are the mass of the solvent and the heat capacity of the solvent, respectively. A sample system time constant τ_s can be calculated by Eq.3.

$$t = -\tau_s \ln(\theta) \quad (3)$$

A dimensionless parameter θ is introduced as followed:

$$\theta = T - T_{Surr} / T_{Max} - T_{Surr} \quad (4)$$

2.2.4 Controlled drug release:

To assess controlled drug release, the PTX–CNH–CM complexes were subjected to an 808 nm NIR laser at an intensity of 1.2 W (approximately 61.1 mW/mm², with a spot diameter of roughly 5 mm) for 20 min. Dispersion of the nanocomplexes was prepared in a 1 mL volume containing a concentration of CNH and PTX at 10 μg/mL each. The temporal release profile of PTX was monitored by collecting samples at specific intervals (0-, 3-, 5-, 7-, 10-, and 20-min post-irradiation). The samples were then filtered to procure the liberated PTX, which was quantitatively analyzed using a UV–vis–NIR spectrophotometer.

2.2.5 Cell culture and viability

Both the Colon 26 and MRC5 cell lines were obtained from the Japanese Collection of Research Bioresources Cell Bank (Tokyo, Japan). The Colon 26 cell line was cultured in Roswell Park Memorial Institute (RPMI) 1,640 medium (Gibco, Grand Island, NY, USA)

supplemented with 10% fetal bovine serum (FBS), 2 mM L-glutamine, 1 mM sodium pyruvate, gentamycin, and 100 IU/mL penicillin-streptomycin. The MRC5 cells were cultured in Dulbecco's Modified Eagle's Medium (Gibco, Grand Island, NY, USA) supplemented with 10% FBS, 2 mM L-glutamine, 1 mM sodium pyruvate, gentamycin, 100 IU/mL penicillin-streptomycin, and Hank's Balanced Salt Solution (Life Technologies, Carlsbad, CA, USA). Both cell lines were maintained at 37 °C in a humidified chamber containing 5% CO_2. To prevent the genetic instability associated with high passage numbers, the cell stocks were regularly revived from cryopreserved vials stored in liquid nitrogen.

Cell viability was assessed using the Cell Counting Kit-8 (CCK-8) assay (Dojindo Laboratories, Kumamoto, Japan), following the manufacturer's instructions. Briefly, 1×10^4 cells per well were seeded in 96-well plates and allowed to adhere overnight. The cells were then exposed to the nanoparticles and irradiated with laser, as indicated. After washing with fresh medium, the cells were incubated with the CCK-8 solution for 2 h at 37°C. The absorbance at 450/690 nm was measured using a microplate reader.

2.2.6 Intracellular penetration of the CNH complex:

Colon 26 cells (1×10^5 cells per well) were seeded in polylysine-coated glass-bottom dishes (Matsunami Glass, Osaka, Japan) and allowed to adhere overnight. The cells were then exposed to 10 μg/mL of ICG-PTX-CNH-CM (where the ICG, CNH, and PTX concentrations were 10, 10, and 1 μg/mL, respectively) for 24 h at 37°C in a humidified incubator containing 5% CO_2.

The intracellular penetration of the ICG–PTX–CNH–CM was observed using an FL

microscopy system (IX73) equipped with a mirror unit (IRDYE800-33LP-A-U01; Semrock, Lake Forest, IL, USA) and an objective (40× magnification, 0.95 numerical aperture; UPLSAPO20X, Olympus) at room temperature. For 3D fluorescence bioimaging, the Colon 26 cells were incubated with ICG–PTX–CNH–CM in a similar manner. After three washes with PBS, the cells were examined, and images were acquired using a fluorescence microscope (BZ-X800, Keyence, Tokyo, Japan) and 3D analysis software (Keyence).

2.2.7 Cell culture and nanocomplex treatment

Cells at a density of 1×10^5 cells/mL were seeded into bioimaging dishes and incubated overnight to allow for adherence. A suspension of ICG–PTX–CNH–CM nanoparticles in PBS (with a CNH concentration of 10 μg/mL) was prepared and introduced to the cells. Alternatively, an equivalent volume of PBS was added as a control. The cells were then incubated for 2 h at 37°C in a 5% CO_2 atmosphere. After three washes with PBS, the cells were maintained in RPMI medium.

A configured laser setup was employed to evaluate the destroyed cancer cells caused by laser-activated nanomedicine. An 808 nm NIR continuous-wave diode laser with an output of 254 mW (equating to an intensity of approximately 129 mW/mm^2) was integrated into an IX73 microscopy system (Olympus, Tokyo, Japan). A focused laser beam of 50 μm in diameter was directed onto the cells using a 40× objective lens with a numerical aperture of 0.95 (UPLSAPO40X, Olympus). The irradiation was conducted at room temperature for 5 s. Pre- and during irradiation images were captured with an electron-multiplying charge-coupled device camera (DP80, Olympus).

2.2.8 In vivo fluorescent bioimaging

The animal experiments were conducted following protocols approved by the Institutional Animal Care and Use Committee of the Japan Advanced Institute of Science and Technology (JAIST) (No. 06–001). To monitor the chronological changes in fluorescence intensity due to the PTX–CNH–CM tumor-targeting effect, Colon 26 tumor-bearing female BALB/cCrSlc mice (6 weeks old, n = 4, average weight = 18 g, average tumor size = 100 mm^3) were intravenously injected with 200 μL of PBS or PBS containing ICG–PTX–CNH–CM (200 μL, ICG at 11.11 mg/kg, PTX at 2.5 mg/kg, and CNH at 10 mg/kg, or 200 μL, ICG at 1 mg/mL, PTX at 0.25 mg/mL, and CNH at 1 mg/kg). The mice were sacrificed, and the major organs (heart, liver, spleen, and kidneys) as well as the tumors were imaged using an in vivo fluorescence imaging system (VISQUE InVivo Smart-LF, Vieworks, Anyang, Republic of Korea) with a 3-s exposure time and an ICG filter (excitation: 740–790 nm, emission: 810–860 nm). The fluorescence images were acquired and analyzed using CleVue software at 4, 8, 12, and 24 h post-injection (Vieworks).

2.2.9 In vivo anticancer therapy

Male BALB/cCrSlc mice (n = 65, 6 weeks old, average weight = 15–20 g) were obtained from Japan SLC (Hamamatsu, Japan). Colon 26 cell-derived tumors were induced by subcutaneous injecting a 1:1 mixture of Matrigel (Dow Corning, Corning, NY, USA) and culture medium containing 1×10^7 cells into the right dorsal side of the mice. After approximately 1 week, when the tumor volume reached ~100 mm^3, the mice were intravenously injected with 200 μL of PBS, 200 μL of PBS containing PTX-CNH-CM (PTX at 0.25 mg/mL or 2.5 mg/kg, CNH at 1 mg/mL or 10 mg/kg), 200 μL of PBS containing CNH-

CM (CNH at 1 mg/mL or 10 mg/kg), 200 μL of PBS containing CNH (1 mg/mL or 10 mg/kg), or 200 μL of PBS containing PTX (0.25 mg/mL or 2.5 mg/kg). The dorsal right-side tumors were irradiated for 5 min every other day, starting 24 h after sample injection, for a total of six laser irradiation sessions, using an 808 nm laser (600 mW, 30.6 mW/mm^2).

Thermographic measurements were conducted during laser irradiation using infrared thermography. Tumor formation and overall health (viability and body weight) were monitored every other day. Tumor volumes were calculated using the formula $V = L \times W^2/2$, where L and W represent tumor length and width, respectively. Mice were euthanized when the tumor volumes exceeded 1,500 mm^3, following the guidelines of the JAIST Institutional Animal Care and Use Committee.

IHC staining of tumor tissues: Colon 26 tumor-bearing mice (n = 5) were euthanized one day after the sample intravenous injection and laser irradiation. The tumor tissues from the treatment groups were then harvested for IHC staining. IHC analysis was performed by the Biopathology Institute Co., Ltd. (Oita, Japan) using standard protocols. Briefly, the primary tumors were surgically removed, fixed in 10% formalin, processed for paraffin embedding, and cut into 3–4 μm sections. After incubation with the primary antibody (Table 1), the sections were stained with H&E and examined by light microscopy (IX73). The areas showing positive staining in the tumor tissues were analyzed using a light microscopy system (BZ-X800) and hybrid cell count and microcell count software (Keyence). The color development of 10 independent areas (regions of interest) was analyzed for each treated tumor tissue.

Table 1. Antibodies used in the IHC staining.

Antibody	Type	Source	Catalog No.	Application
F4/80	Mouse Monoclonal	BMA Biomedicals	T-2028	IHC (1:50)
CD3	Rabbit Monoclonal	Abcam	ab16669	IHC (1:100)
CD19	Rabbit Polyclonal	Bioss	bs-0079R	IHC (1:100)
CXCR4	Goat Polyclonal	Abcam	ab1670	IHC (1:100)
NKp46	Rabbit Polyclonal	Affinity Biosciences	DF7599	IHC (1:100)
Caspase-3	Rabbit Polyclonal	Cell Signaling Technology	9661S	IHC (1:100)
TNF-α	Rabbit Polyclonal	Abcam	ab6671	IHC (1:100)

2.2.10 Statistical analysis

All experiments were performed in triplicate and repeated three or more times. Quantitative values are shown as the mean ± standard deviation of at least three independent experiments. Statistical differences were performed using the Student's one-sided/two-sided t-test. P-values <0.05 were considered significant, and P-values <0.01 were considered highly significant.

2.3 Results and discussion

2.3.1 Structural and optical characterization of CNH complexes

The PTX–CNH–CM nanocomplex was synthesized and subjected to comprehensive

visual and physicochemical characterization to confirm successful assembly. The nanocomplex exhibited a uniform dark coloration, indicative of effective PTX loading into carbon nanohorns and the successful incorporation of tumor cell membranes (Figure 2.1A). To evaluate aqueous dispersibility, suspensions of PTX–CNH–CM were prepared and monitored over time. The nanocomplex remained well-dispersed without observable aggregation, demonstrating excellent colloidal stability, a critical prerequisite for subsequent biological evaluations.

The hydrodynamic size and stability of the nanocomplex were quantified by dynamic light scattering (DLS) over a period of 30 days. The results (Figure 2.1B) showed negligible changes in particle diameter, confirming robust colloidal stability and suggesting that the cell membrane coating effectively inhibits aggregation while preserving structural integrity under storage conditions. Collectively, these observations demonstrate that PTX–CNH–CM possesses favorable physicochemical properties, providing a reliable platform for subsequent in vitro and in vivo studies.

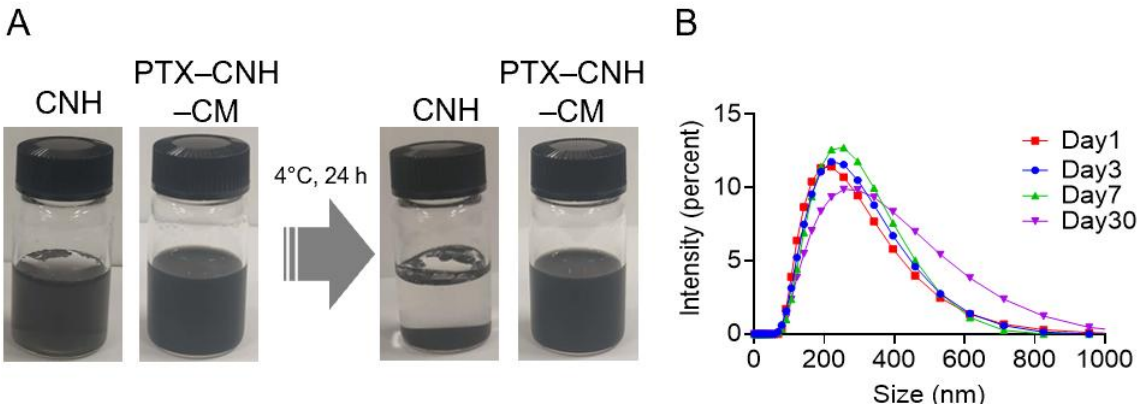

Figure 2.1 Colloidal stability and size distribution of PTX–CNH–CM nanocomposites. A) Images of CNH and PTX–CNH–CM in PBS buffer before and after incubation for 24 h at 4°C. B) DLS size distribution of PTX–CNH–CM. Average hydrodynamic diameters of the PTX–CNH–CM on days 1, 3, 7, and 10 after preparation.

In addition, DLS analysis revealed that CNH–CM exhibited high aqueous dispersibility,

with a hydrodynamic diameter of approximately 219 nm, closely matching that of PTX–CNH–CM (218 nm). These results indicate that coating CNHs with tumor cell membranes effectively enhances their colloidal stability in aqueous media. In contrast, pristine CNHs without functionalization displayed pronounced polydispersity and the formation of large aggregates, reflecting poor water dispersibility due to the intrinsically hydrophobic nature of the CNH surface (Figure 2.2A). This comparison highlights the critical role of membrane coating in facilitating homogeneous dispersion, which is essential for consistent drug delivery and reliable biological interactions.

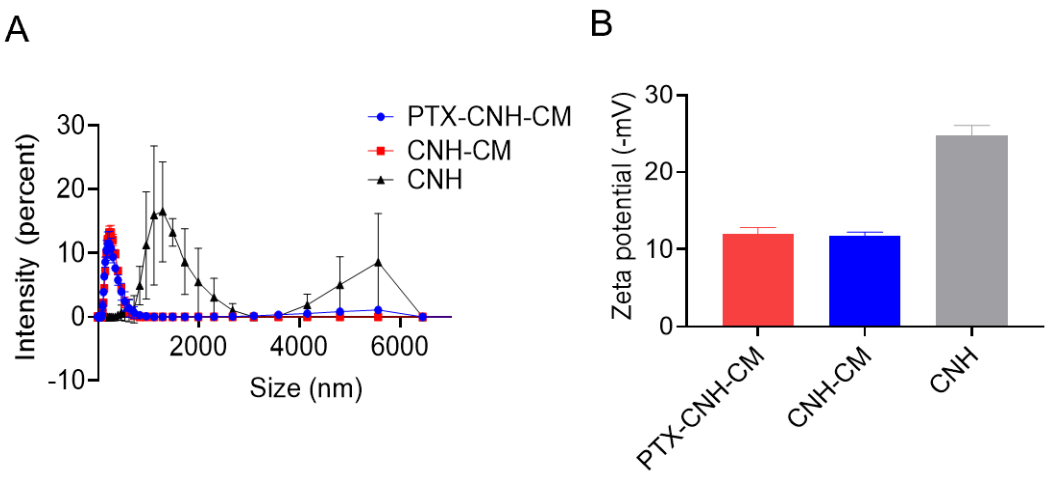

Figure 2.2 Colloidal characterization of CNH-based nanocomposites. A) Dynamic light scattering (DLS) and zeta potential B) measurements of PTX–CNH–CM, CNH–CM, and CNH.

The zeta potentials of CNH, CNH–CM, and PTX–CNH–CM in PBS were measured as –24.7, –11.7, and –11.9 mV, respectively (Figure 2.2B). The highly negative surface charge of pristine CNH is likely attributed to the carboxyl and hydroxyl groups introduced during the production process[22-23]. Upon coating with the tumor cell membrane, the zeta potential of the nanocomplex became less negative, suggesting that multivalent interactions between membrane components and the CNH surface modulate the electrostatic properties of the

resulting nanostructures. Collectively, these findings indicate that tumor cell membranes not only preserve particle size and prevent aggregation but also actively regulate the surface characteristics of CNH. Such physicochemical improvements are expected to enhance the performance of the nanocomplex in subsequent drug delivery and biological assays, thereby establishing a reliable platform for both in vitro and in vivo studies.

TEM analysis revealed that PTX–CNH–CM exhibited a uniform spherical morphology with an average diameter of approximately 200 nm (Figure 2.3). Owing to the membrane coating, the TEM images clearly displayed a well-defined core–shell structure, in which the CNH core was enveloped by a lighter and continuous membrane layer, confirming successful tumor cell membrane coating. The particle size observed by TEM was slightly smaller than that measured by DLS, which can be attributed to the absence of a hydration layer in the dry state during TEM sample preparation.

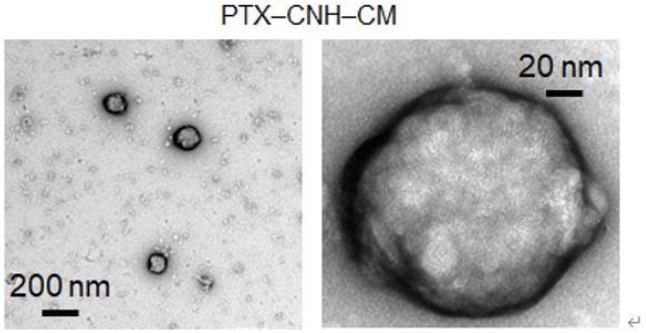

Figure 2.3 TEM observations of PTX–CNH–CM.

Meanwhile, CNH–CM also exhibited a monodisperse distribution on the TEM grid, with a coating structure derived from cellular components that closely resembled that of PTX–CNH–CM. By contrast, pristine CNHs showed no discernible coating layer; their characteristic

single-graphene tubules with exposed horn-shaped tips were clearly observed, and pronounced aggregation was evident, consistent with the poor aqueous dispersibility described previously (Figure 2.4).

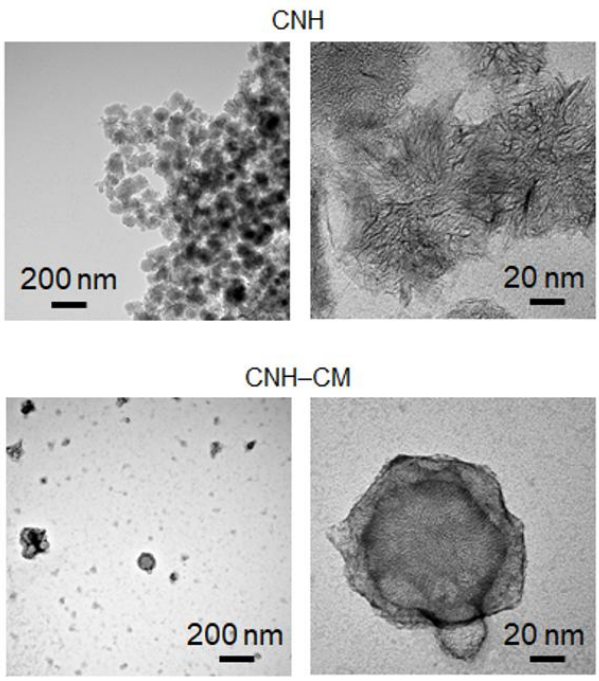

Figure 2.4 TEM observations of CNH and CNH–CM.

This microscopic observation, together with DLS and zeta potential measurements, confirmed that PTX–CNH–CM possesses a well-defined and stable nanostructure. The uniform size distribution and intact membrane coating are critical for ensuring reproducible drug delivery, minimizing premature aggregation, and facilitating consistent interactions with cellular targets. Overall, the combined physicochemical characterization establishes PTX–CNH–CM as a reliable platform for subsequent in vitro cytotoxicity assays and in vivo therapeutic evaluation.

To further quantify the amount of tumor cell membrane and drug loaded onto the CNH

surface, thermogravimetric analysis (TGA) was performed. This technique allows for precise determination of mass loss associated with the organic coating and loaded drug, providing a direct measure of the functionalization efficiency of the nanocomplex. As shown in Figure 2.5, TGA results indicated that approximately 0.74 mg of cell membrane and 0.09 mg of PTX were coated on the surface of 1 mg of CNH. These findings confirm the successful loading of both the biomimetic membrane and the therapeutic agent onto the nanocarrier, consistent with the structural and morphological observations from TEM and DLS analyses.

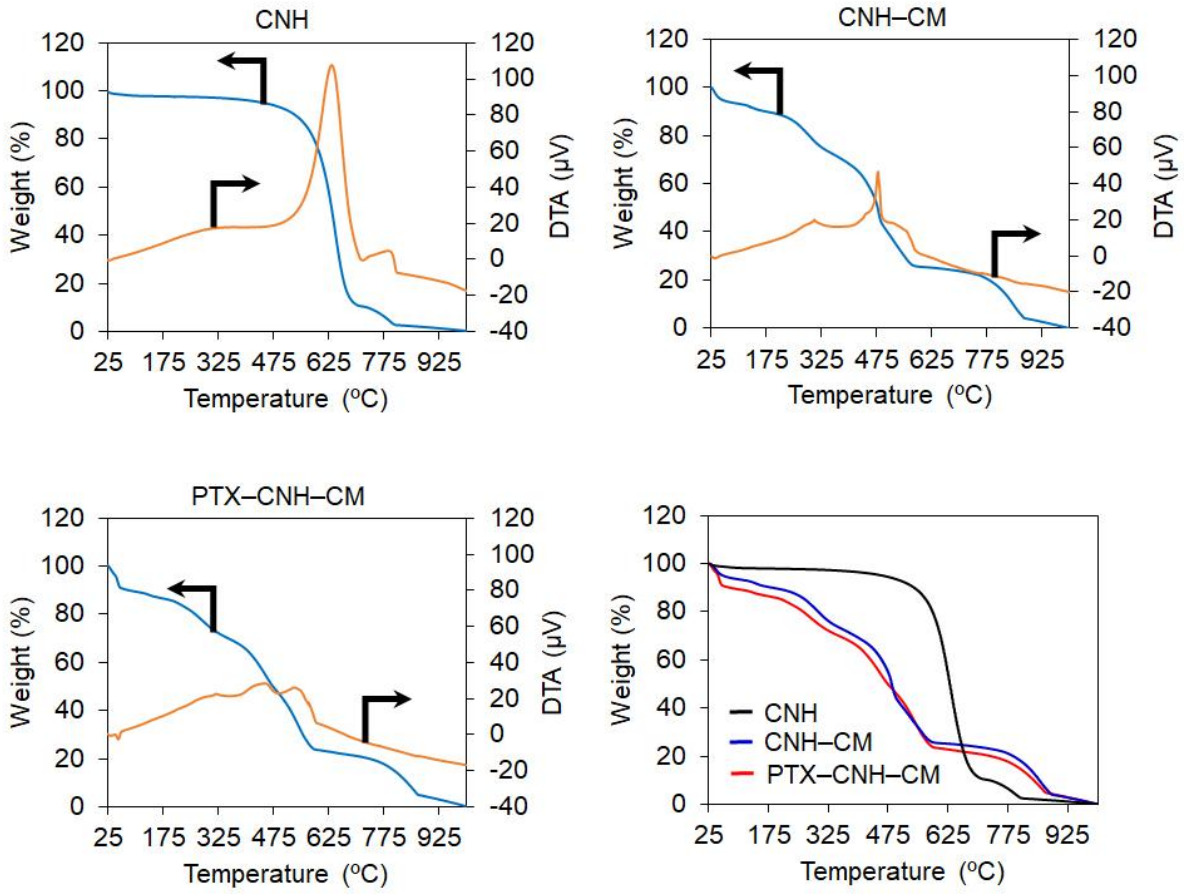

Figure 2.5 Thermogravimetric analysis (TGA) of CNH, CNH–CM, and PTX–CNH–CM.

To characterize the functional properties of the nanocomplexes, their optical behavior was examined by UV–Vis absorption spectroscopy. CNH–CM exhibited a pronounced absorbance

in the near-infrared (NIR) region (700–1,000 nm) (Figure 2.6). In addition, a distinct peak between 200 and 300 nm was observed, corresponding to the intrinsic absorption of PTX and CNH components. The absorption profile of PTX–CNH–CM closely resembled that of CNH–CM, indicating that tumor cell membrane coating did not alter the inherent optical characteristics of the nanoparticles. These findings confirm that PTX–CNH–CM retains the characteristic NIR absorption of CNH.

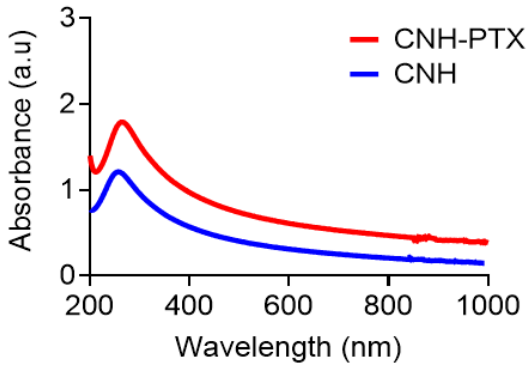

Figure 2.6 UV–vis–NIR absorbance spectra of PBS suspension of CNH and PTX–CNH–CM. (PTX concentration = 5 μg/mL and CNH concentration = 50 μg/mL).

CNHs outperform many inorganic nanomaterials, such as metallic nanoparticles and nanorods, owing to their high drug-loading capacity derived from the large surface area and strong CNH–drug hydrophobic interactions[24]. We hypothesized that coating drug-loaded CNHs with a cellular membrane would prevent premature drug leakage while simultaneously enhancing blood circulation time and tumor-targeting capability. The drug-loading efficiency of the PTX–CNH–CM nanocomplex was determined by quantifying the amount of unbound PTX remaining after filtration, using a UV–vis–NIR spectrometer. The results showed that approximately 86.4% of PTX was successfully incorporated into the nanocomplex.

Interestingly, irradiation with an 808 nm NIR laser at 1.2 W (ca. 61.1 mW/mm²) enabled

spatiotemporally controlled PTX release (Figure 2.7). In this study, a fiber-coupled 808 nm continuous-wave diode laser was selected due to its high tissue penetration, ease of visual targeting, and cost-effective commercial availability. These findings indicate that the CNH–CM platform can function as a light-responsive drug carrier with potential utility in precise cancer therapy.

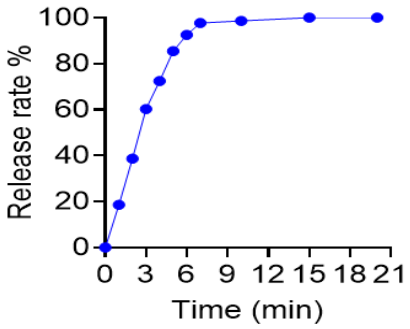

Figure 2.7 Drug release profile from laser-induced PTX–CNH–CM. Data are presented as means ± standard error of the mean (SEM) (n = 3; independent tests).

The photothermal performance of the PTX–CNH–CM complex was systematically assessed using an 808 nm laser and a thermocouple to monitor temperature changes. While NIR light does not penetrate as deeply into tissues as modalities such as X-rays or ultrasound, it offers distinct advantages for tumor therapy: the ability to deliver localized, highly focused energy and to achieve precise spatial control of heating when coupled with efficient photothermal nanomaterials. Such characteristics enable selective energy deposition in tumor tissue, reducing collateral damage to surrounding healthy structures.

For this study, an 808 nm continuous-wave diode laser was selected because of its high tissue transparency, low absorption by water and endogenous biomolecules, and visible beam that facilitates accurate targeting. When the PTX–CNH–CM suspension (CNH concentration

= 1 mg/mL) was irradiated at a power density of 0.3 W (15.3 mW/mm²), the temperature increased rapidly to approximately 58 °C (Figure 2.9A). This pronounced rise confirms the nanocomplex's ability to efficiently convert NIR light into thermal energy.

Moreover, the magnitude of temperature elevation could be readily modulated by adjusting either the laser power density (0.6 or 1.2 W, corresponding to 30.6 and 61.1 MW mm^{-2}, respectively) or the nanocomplex concentration (Figures 2.8B and 2.8C). This predictable, dose-dependent photothermal response underscores the versatility of the PTX-CNH-CM system, enabling fine-tuning of thermal output to accommodate diverse therapeutic strategies ranging from mild hyperthermia to ablative cancer therapy.

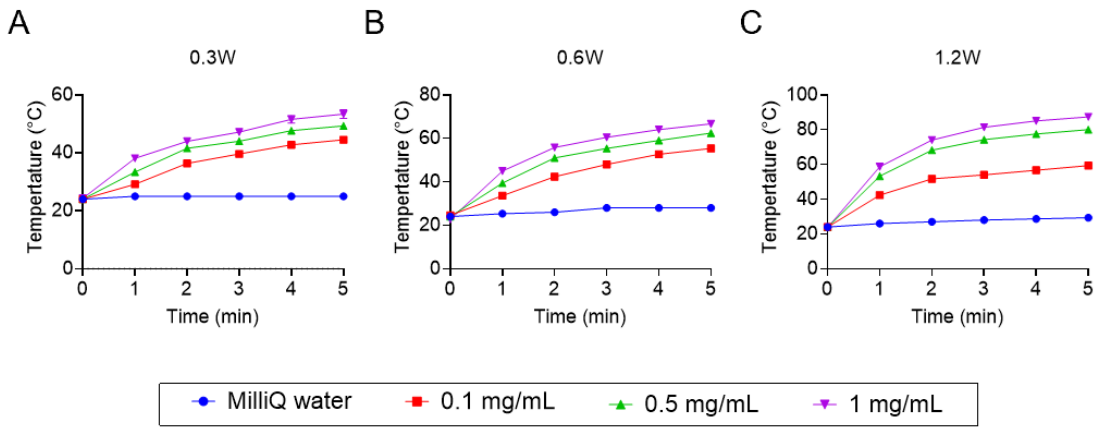

Figure 2.8 Photothermal conversion properties of the CNH complex. A–C) Laser-induced temperature increase in MilliQ water (control) and PTX–CNH–CM suspensions at different CNH concentrations by 808 nm laser irradiation at 0.3 W (15.3 mW/mm²), 0.6 W (30.6 mW/mm²), or 1.2 (60.12 mW/mm²) power. CNH (1 mg/mL) was dispersed in 0.2 mL of PBS. Data are presented as means ± SEM (n = 3; independent tests).

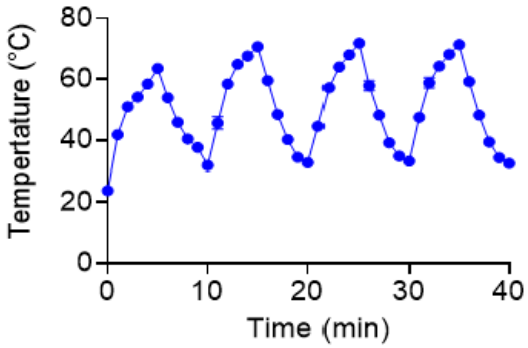

Figure 2.9 Photothermal stability test of the PTX–CNH–CM solution under photothermal heating and natural cooling cycles by 808 nm laser irradiation at 1.2 W (≈ 61.1 mW/mm2) power.

Given the critical importance of stability in ensuring consistent therapeutic efficacy and minimizing unintended thermal injury to surrounding tissues during PTT, we monitored the temperature changes of the nanocomplexes over four consecutive laser on/off cycles. The analysis revealed negligible fluctuations and only a marginal decline in peak temperature, thereby demonstrating satisfactory photothermal stability of the PTX-CNH-CM system (Figure 2.9). These results highlight the robustness of the nanocomplex under repeated thermal stress and affirm its reliability as a precision-targeted photothermal agent for cancer therapy.

We further validated the potent photothermal conversion capability of PTX–CNH–CM by acquiring thermographic images at varying concentrations before and after 5 min of laser irradiation under different power densities (Figure 2.10).

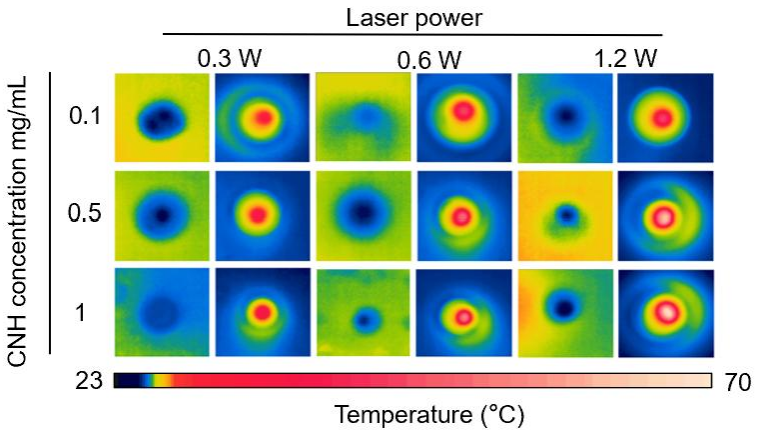

Figure 2.10 Thermographic images of PTX–CNH–CM solution after 5-min laser irradiation at various laser powers 0.3 W (~15.3 mW/mm2), 0.6 W (~30.6 mW/mm2), and 1.2 W (~ 61.1 mW/mm2) and different CNH concentrations (0.1, 0.5, and 1.0 mg/mL).

The photothermal conversion efficiency of PTX–CNH–CM was calculated to be 63%, exceeding that of a wide range of reported nanomaterials, including representative metal-based systems, carbon dots, and semiconducting polymer nanoparticles (Table 2)[19, 23-25]

This high efficiency highlights the superior capability and stability of PTX–CNH–CM in converting light into heat, further supporting its potential for effective photothermal tumor ablation.

Table 2. The photothermal conversion efficiency of materials in previous reports.

Material	Photothermal conversion	Reference
PTX–CNH–CM	63	This study
Gold nanorods	21	20
Gold nanoshells	13	20
Copper selenide	22	20
Carbon dots	31	21
Semiconducting	37	22

2.3.2 In vitro anticancer efficacy of the CNH complex

The in vitro anticancer efficacy of laser-activated PTX–CNH–CM nanocomplexes was assessed against human normal MRC-5 fibroblasts and Colon26 cancer cells (Figure 2.11). Before evaluating their combined photothermal and chemotherapeutic effects, the potential intrinsic cytotoxicity of CNH–CM was examined by incubating cells with various concentrations of CNH–CM for 24 h without laser irradiation. Notably, CNH–CM exhibited negligible cytotoxicity toward both MRC-5 and Colon26 cells across all tested concentrations, whereas the RIPA buffer used as a positive control induced severe cytotoxicity in both cell types (Figure 2.11A). In contrast, PTX–CNH–CM induced significant cytotoxicity toward both cell types, attributable to the presence of the chemotherapeutic agent PTX (Figure 2.11B). Importantly, PTX–CNH–CM displayed higher cytotoxicity against Colon26 cells than MRC-5 cells, which can be ascribed to the selective susceptibility of cancer cells to PTX, reflecting tumor-specific biochemical responses to the drug[26].

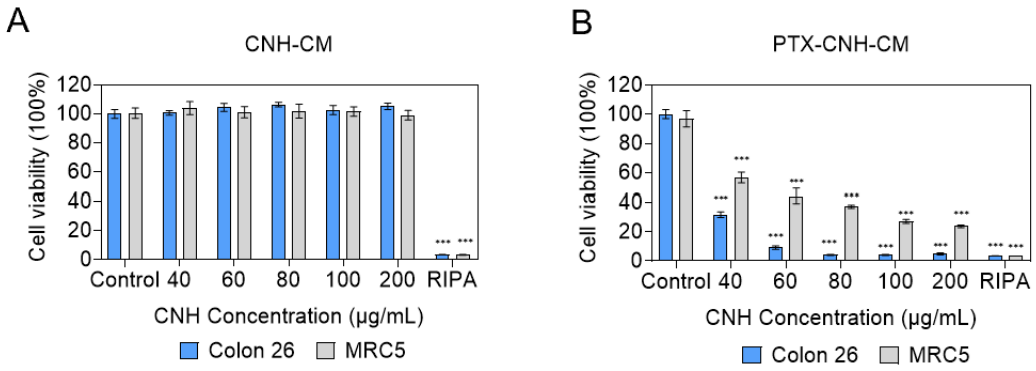

Figure 2.11 Viability of Colon 26 and MRC5 cells treated with the CNH nanocomplext. A) CNH–CM, B) PTX–CNH–CM and RIPA buffer (control) at various CNH concentrations. Cell viability was tested 24 h after treatment. Data presented as means ± SEM (n = 5; biologically independent tests), ***, $p < 0.001$ versus control without nanoparticles (Students t-test).

The cytotoxic effects of laser-activated CNH–CM and PTX–CNH–CM complexes were subsequently evaluated (Figures 2.12). Upon laser irradiation at a power density of 0.32 W cm^{-2} (≈61.1 mW mm^{-2}), CNH–CM exhibited substantial cytotoxicity against both MRC-5 and Colon26 cells (Figures 2.12A), which was attributed to the strong photothermal conversion capability of the CNH core. Furthermore, laser-irradiated PTX–CNH–CM induced even greater cytotoxicity in both cell lines (Figures 2.12B), attributable to the synergistic effect of chemotherapeutic PTX release combined with the potent photothermal heating generated by CNH.

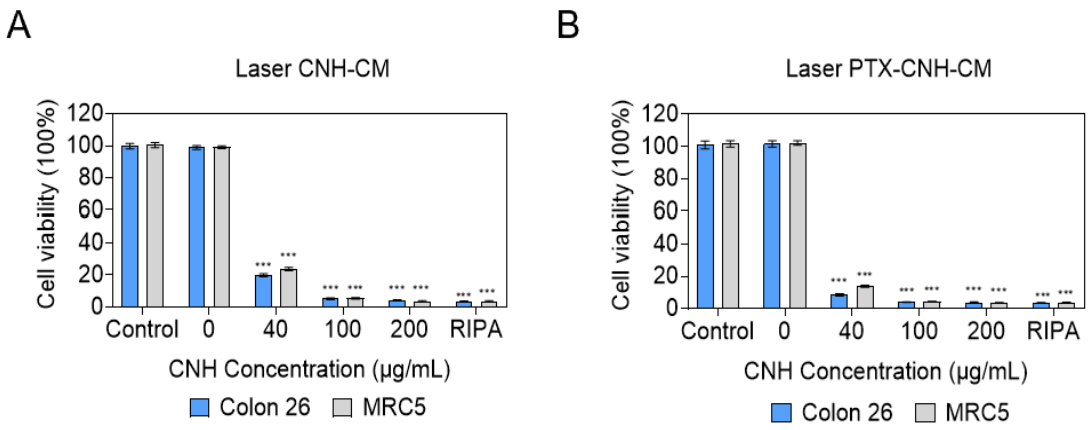

Figure 2.12 Laser-induced cytotoxicity evaluation in Colon 26 and MRC5 cells exposed to the A) CNH–CM, B) PTX–CNH–CM, and RIPA buffer (control) after 24 h of treatment with 5 min laser irradiation (0.3 W [~15.3 mW/mm^2]) at various CNH concentrations. Data presented as means ± SEM (n = 5; biologically independent tests), ***, $p < 0.001$, by Student's t-test.

To evaluate the cellular uptake and interaction of the CNH complexes with Colon26 cells, fluorescence spectroscopy and fluorescence microscopy were employed. For this purpose, a NIR-fluorescent formulation, ICG-PTX-CNH-CM, was prepared by incorporating the hydrophobic NIR dye indocyanine green (ICG) into PTX-CNH-CM via a simple sonication process, as detailed in the Experimental Section. In this design, both hydrophobic ICG and PTX were embedded within the lipid-mediated hydrophobic domains of the tumor cell

membrane coating. Interestingly, the synthesized ICG-CNH-CM exhibited negligible fluorescence emission from ICG upon NIR excitation, which is likely attributable to strong molecular interactions between CNH and ICG[27-28] that result in fluorescence quenching (Figure 2.13).

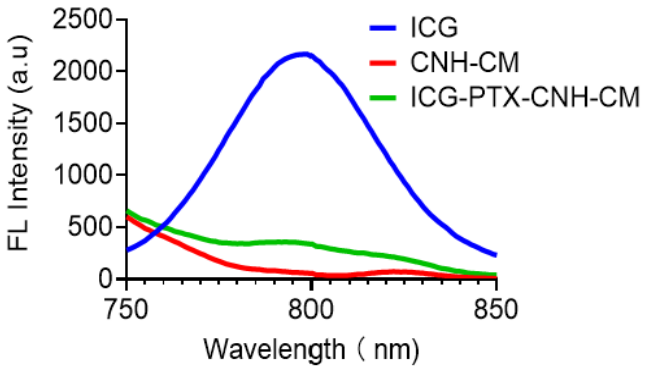

Figure 2.13 FL spectra of ICG, CNH–CM, ICG–PTX–CNH–CM at 750 nm excitation wavelength. ICG, (concentration = 12.5 μg/mL), CNH–CM (CNH concentration = 125 μg/mL), and ICG–PTX–CNH–CM (CNH concentration = 125 μg/mL, ICG concentration = 12.5 μg/mL, and ICG–PTX concentration = 31.3 μg/mL

The loading efficiency of ICG was subsequently determined using the same analytical approach employed for calculating PTX loading efficiency. (Figure 2.14A) Free ICG rapidly precipitated in PBS after 2 days of storage, indicating its poor aqueous stability. The fluorescence spectra of ICG solutions at various concentrations (0.8–10 μg/mL) exhibited a characteristic emission peak around 820 nm, with intensity positively correlated to concentration (Figure 2.14B) A linear relationship ($R^2 = 0.9939$) between fluorescence intensity and ICG concentration was established, confirming reliable quantitative analysis (Figure 2.14C).The fluorescence spectra of ICG–CNH–CM before and after filtration showed negligible difference, suggesting that ICG was successfully loaded and retained within the nanocomplex even after purification Results showed that approximately 99.6% of ICG was

successfully incorporated into the nanocomplex (Figure 2.14D). Following filtration with DMSO, about 87.7% of ICG was released from the CNH, which restored the fluorescence properties of ICG in the filtrate (Figure 2.14E). These observations confirm that ICG molecules were effectively bound to the CNH–CM structure.

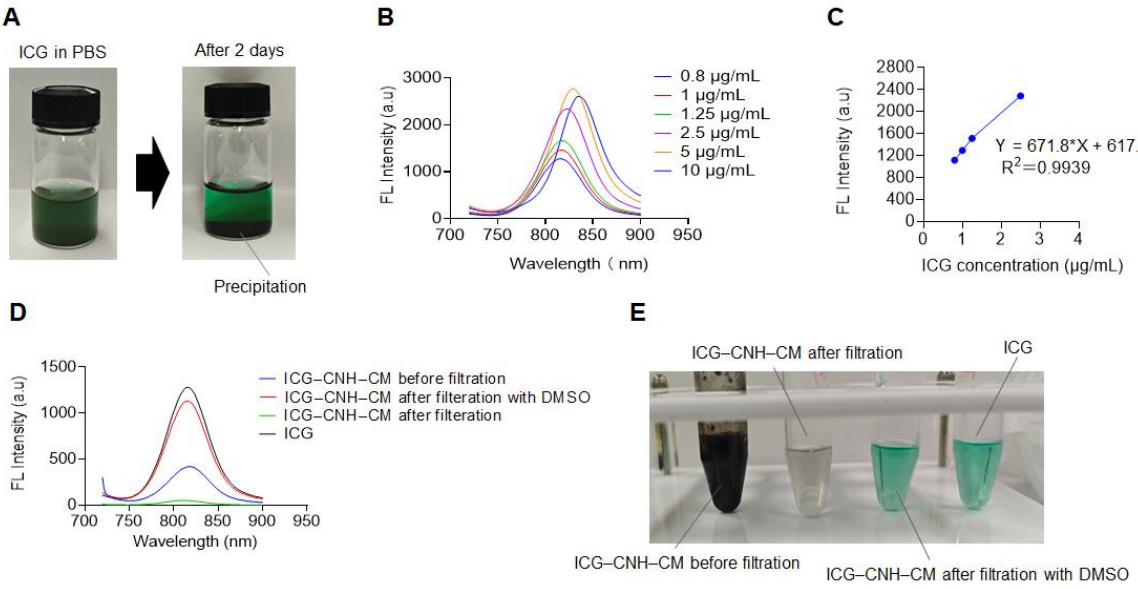

Figure 2.14 Loading efficiency of ICG into CNH–CM. A) Photo of aqueous solutions of ICG in PBS just after preparation (left) and after 2 days at 20°C (right). ICG forms visible aggregations and massive precipitations in PBS. B) Fluorescence (FL) intensity of ICG solution in DMSO at different concentration. C) Calibration curve of ICG solution in DMSO. D) FL intensity of each sample before and after treatments. Concentration of ICG was adjusted before treatment. E) Photo of each sample before and after treatments.

After 24 h of incubation of ICG-PTX-CNH-CM with Colon26 cells at 37 °C, a distinct pink fluorescence signal was observed, indicating efficient intracellular uptake of the nanocomplex (Figure 2.15A). In contrast, the control group exhibited no detectable fluorescence, further confirming that the observed signal originated specifically from the ICG-PTX-CNH-CM. Moreover, three-dimensional fluorescence microscopy revealed a uniform intracellular distribution of the nanocomplex within the cytoplasmic region, suggesting successful internalization and dispersion inside the cells (Figure 2.15B).

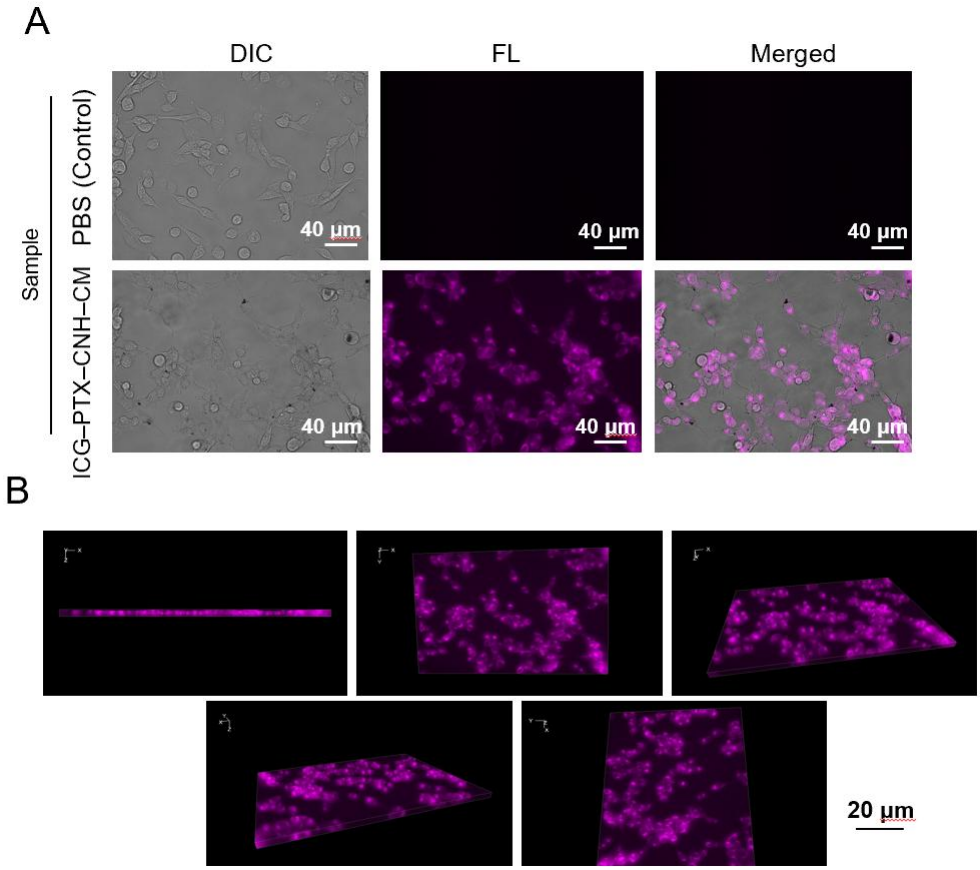

Figure 2.15 Intracellular distribution of the CNH complex. A) FL bioimaging of Colon26 cancer cells after incubation with PBS (control) and ICG–PTX–CNH–CM. The 2D pictures represent differential interference contrast (DIC), FL, and a merged image (DIC+ FL). Pink and black particles represent ICG–PTX–CNH–CM. B) 3D FL images of Colon 26 cells after incubation with ICG–PTX–CNH–CM.

The real-time anticancer effect of NIR laser–activated ICG-PTX-CNH-CM was evaluated using a single laser beam integrated with the fluorescence microscopy system. Upon 808 nm laser irradiation at 564 mW (approximately 287 mW/mm²), Colon26 cells were rapidly destroyed, accompanied by the formation of bubbles, which can be attributed to localized water vaporization resulting from the intense photothermal effect of CNH (Figure 2.16). In contrast, the control group without CNH-CM-PTX exhibited no detectable cellular or spheroid damage under the same irradiation conditions. These findings highlight the strong photothermal conversion capacity of the CNH-based nanocomplex and underscore its potential for precise

and potent photothermal ablation of cancer cells.

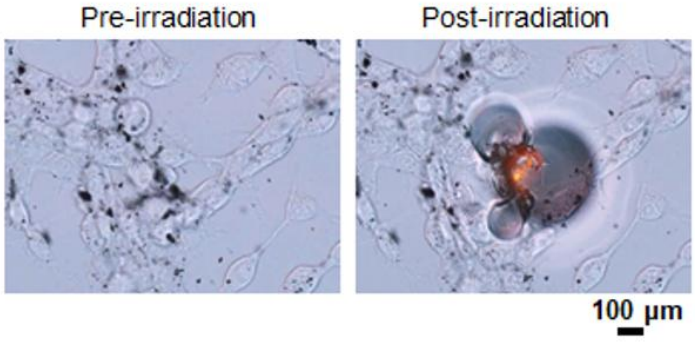

Figure 2.16 Real-time observation of Colon 26 cancer cell destruction by laser-induced PTX–CNH–CM before and after laser irradiation. (808 nm, 564 mW, ~287 mW/mm2). The red circle represents the laser irradiation position and area.

2.3.3 In vivo targeting and anticancer effect of CNH complexes

The systemic biodistribution of the functional tumor cell membrane–modified CNH complex was evaluated to assess its tumor-targeting ability and in vivo anticancer potential. Fluorescent ICG-PTX-CNH-CM was intravenously administered to Colon26 tumor–bearing mice via tail vein injection, and whole-body fluorescence was monitored over 28 h using an in vivo bioimaging system. A pronounced fluorescence signal was observed at the tumor site following injection Figure 2.17A, indicating efficient accumulation of the CNH nanocomplex, consistent with the enhanced permeability and retention (EPR) effect[29]. In contrast, no detectable fluorescence was observed in the PBS group throughout the entire imaging period. At the end of the experiment, major organs were collected to examine ex vivo fluorescence distribution. As shown in Figure 2.17B, apart from the tumor, strong fluorescence was also detected in the lungs and weaker signals in the kidneys. The pronounced tumor-associated fluorescence further validates the effective tumor accumulation of PTX-CNH-CM. The fluorescence observed in the kidneys and lungs may be attributed to the high aqueous

dispersibility and prolonged circulation of the nanocomplex, with renal clearance likely serving as a predominant elimination pathway.

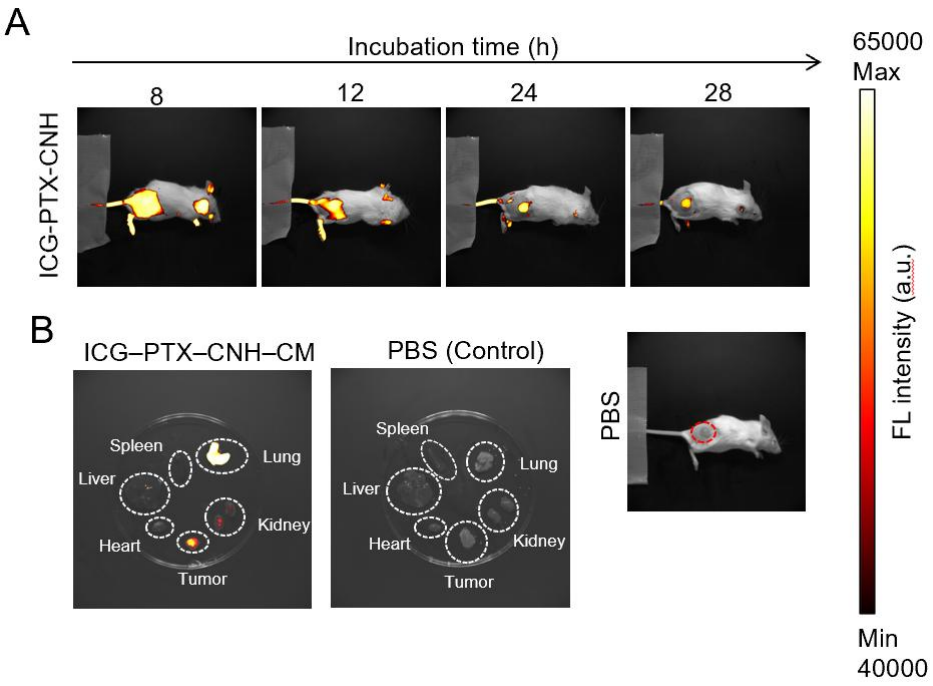

Figure 2.17 Systemic distribution of the CNH complex in the tumor model. A) FL imaging of Colon 26 tumor-bearing mice after i.v. injection of PBS and ICG–PTX–CNH–CM. B) Extracted vital organs and tumors after an i.v. injection of PBS or ICG–PTX–CNH–CM (ICG, 11.11 mg/kg; and CNH, 5.6 g/kg) (200 μL, ICG, 1 mg/mL; and CNH, 1 mg/mL). The red dashed circle denotes the solid tumor location.

Notably, the ICG–PTX–CNH–CM formulation demonstrated superior tumor-targeting capability compared with a conventional CNH preparation containing the dispersant Cremophor® EL and NIR fluorescent dye ICG (ICG–CNH–CRE) (Figure 2.18). This enhanced performance can be attributed to the advantages conferred by the tumor cell membrane coating, including improved aqueous dispersibility, excellent biocompatibility, extended systemic circulation, and increased tumor penetration. Collectively, these results confirm that ICG–PTX–CNH–CM achieves high tumor selectivity and prolonged retention at the tumor site following a single administration. Given that the effectiveness of any therapeutic strategy

depends on its ability to access a substantial proportion of the tumor mass, these findings suggest that engineering a tumor-selective CNH complex represents a promising strategy to target and anchor within a broader population of cancer cells located deep inside and throughout the tumor stroma.

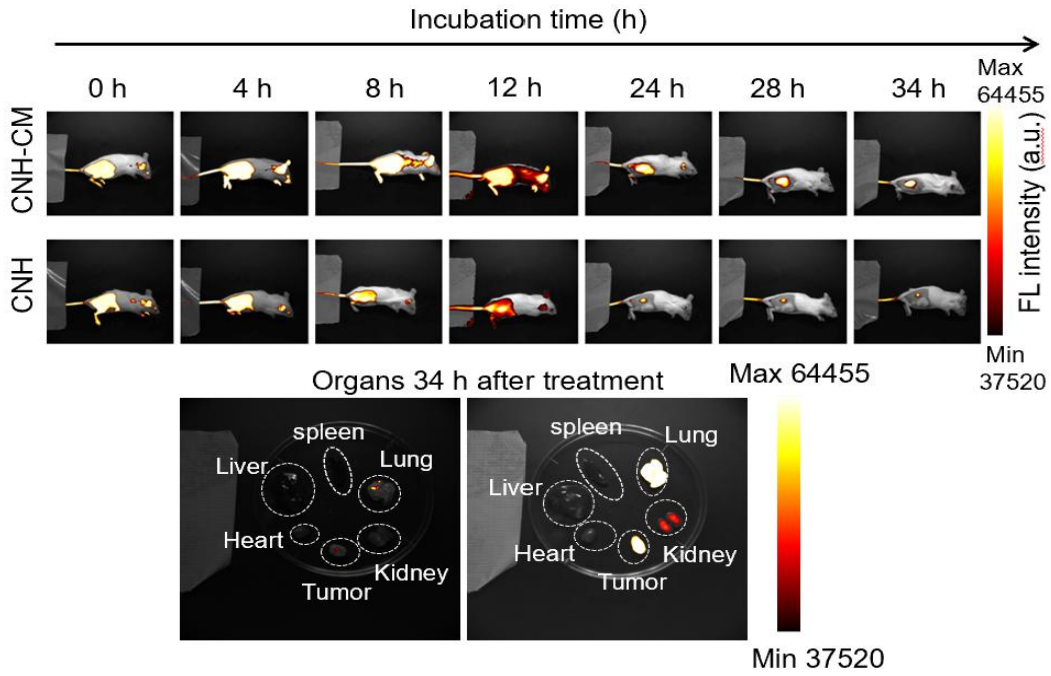

Figure 2.18 FL imaging of Colon 26 tumor-bearing mice and extracted organs after i.v. injection of ICG–CNH–CM and ICG–CNH–CRE. (ICG, 11.11 mg/kg; and CNH, 5.6 g/kg) (200 μL, ICG, 1 mg/mL; and CNH, 1 mg/mL).

The in vivo photothermal performance of the nanocomplexes was evaluated 24 h after a single intravenous administration. Colon26 tumors in mice were irradiated with an 808 nm laser at a power density of 600 mW (≈30.6 mW mm^{-2}), and body surface temperature was continuously monitored using a thermographic camera In the PTX–CNH–CM–treated group, tumor surface temperature increased rapidly, reaching approximately 58 °C within 5 min of irradiation (Figure 2.19). Although injection of the CNH–Cremophor (CNH–CRE) formulation also induced substantial temperature elevation, the effect was slightly lower than that observed

with PTX–CNH–CM under identical conditions. This enhanced photothermal effect is attributed to the superior tumor accumulation of PTX–CNH–CM, driven by the synergistic contributions of homologous targeting and the enhanced permeability and retention (EPR) effect. Specifically, beyond the EPR effect, tumor cell membrane coating facilitates binding of PTX–CNH–CM to tumor-associated proteins and promotes phagocytic uptake by myeloid cells such as macrophages and neutrophils.

In contrast, control groups (PBS and PTX) exhibited only minor temperature increases following laser irradiation, likely due to nonspecific heat generation from light absorption by skin, blood, and underlying tissue. These results not only validate the precise tumor-targeting capability and strong photothermal conversion of CNH–CM–based complexes but also highlight their therapeutic potential. The findings underscore the strategic advantage of integrating targeted delivery with synergistic PTT, demonstrating the ability of these nanoparticles to localize within and thermally disrupt tumor tissues with high efficiency.

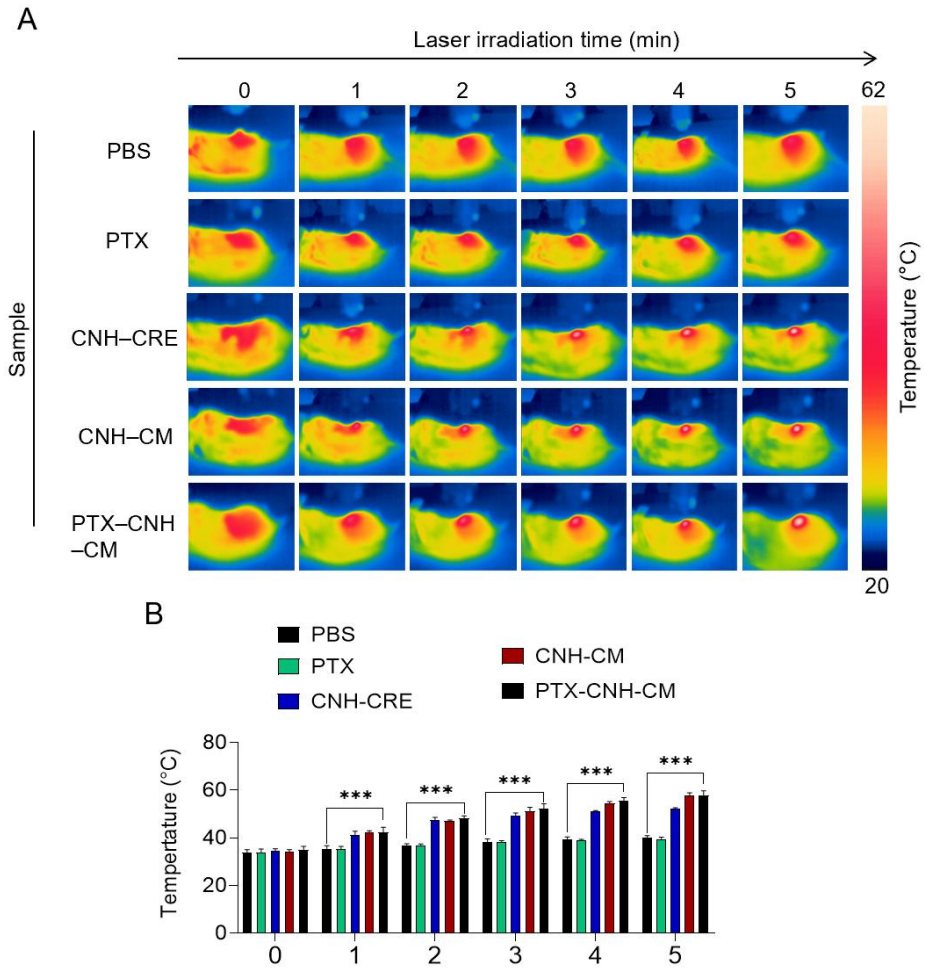

Figure 2.19 In vivo photothermal conversion behavior of laser-induced PTX–CNH–CM. A) Thermographic measurement of the tumor surface by treatment with PBS or PTX–CNH–CM-i.v. injected mice. Laser power, irradiation time, and wavelength are 0.6 W (~30.6 mW/mm2), 5 min, and 808 nm. B) Temperature changes of tumors in Colon26-bearing mice on day 2 after injection with PTX-CNH-CM or PBS followed by 808 nm laser irradiation for 5 min [laser power = 0.6 W (~30.6 mW/mm2)]. Data are expressed as means ± SEM; n = 5 independent experiments. Statistical significance was calculated in comparison with the PBS group. ***$p < 0.001$, by Student's t-test.

We next evaluated the in vivo anticancer efficacy of PTX–CNH–CM in the absence of laser irradiation. Among all groups, PTX–CNH–CM exhibited the most pronounced inhibitory effect on tumor growth (Figures 2.20). This superior performance is likely attributable to the synergistic combination of the chemotherapeutic activity of PTX and the immune activation elicited by membrane components. At the same PTX dose, free PTX displayed significantly

weaker tumor inhibition compared with PTX–CNH–CM. Similarly, CNH–CM achieved a comparable level of tumor suppression to free PTX, which can be ascribed to its tumor-targeting capability and immune-activating properties provided by the cell membrane coating. By contrast, CNH–Cremophor (CNH–CRE) showed negligible therapeutic effects, similar to PBS, owing to the absence of photothermal activity.

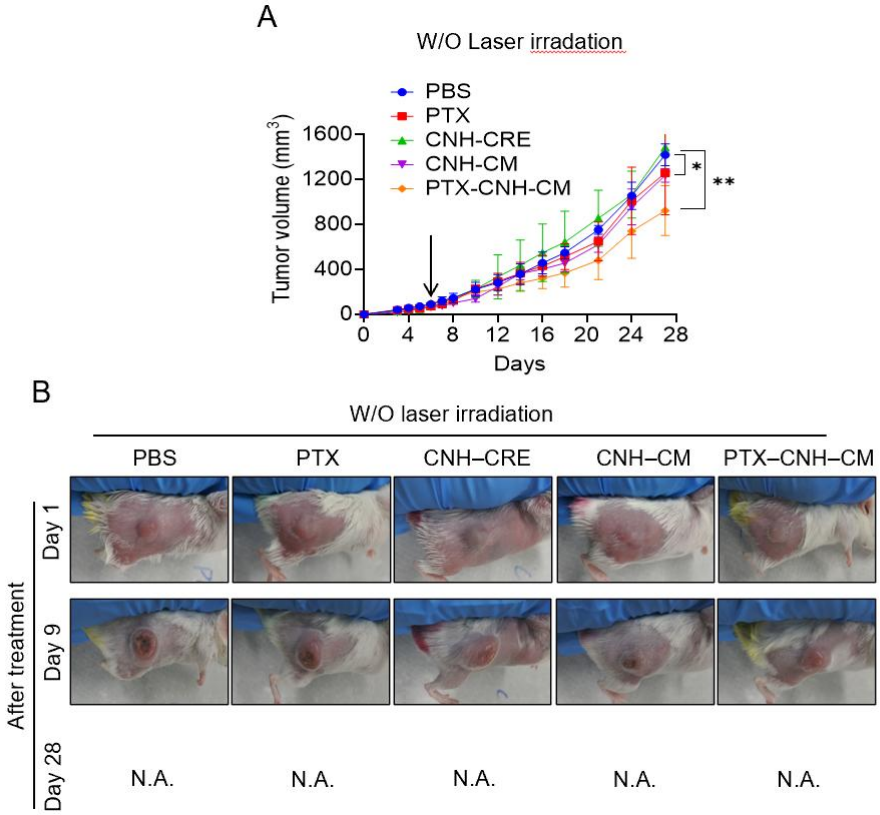

Figure 2.20 In vivo anticancer test of CNH complexes. A) Anticancer efficacy of various samples with and without laser irradiation. PBS or dispersion of PTX, CNH, CNH–CM, and PTX–CNH–CM was intravenously injected into the Colon 26-bearing mice. Data are expressed as means ± SEM ($n \geqslant 4$ biologically independent tests). *$p < 0.05$, ***$p < 0.001$, by Student's t-test. The black arrows display the time point of sample administration. B) Photos of the mice after each treatment.

The laser-mediated anticancer efficacy was further assessed in Colon26 tumor–bearing mice. Among all treatment groups, PTX–CNH–CM, CNH–CM, and CNH–CRE under laser irradiation induced complete tumor regression after two treatment sessions, attributable to the tumor-targeting effect and potent photothermal ablation generated by CNH (Figures 2.21).

Notably, PTX–CNH–CM achieved more rapid tumor regression compared with CNH–CM and CNH–CRE, likely due to efficient homotypic tumor targeting, controlled PTX release, and immune stimulation conferred by the cell membrane coating. In comparison, the PTX + laser group exhibited significant therapeutic effects relative to PBS + laser, primarily reflecting the chemotherapeutic activity of PTX. Collectively, these results demonstrate that PTX–CNH–CM achieves a robust synergistic therapeutic outcome by integrating photothermal, chemotherapeutic, and immunological effects under laser irradiation.

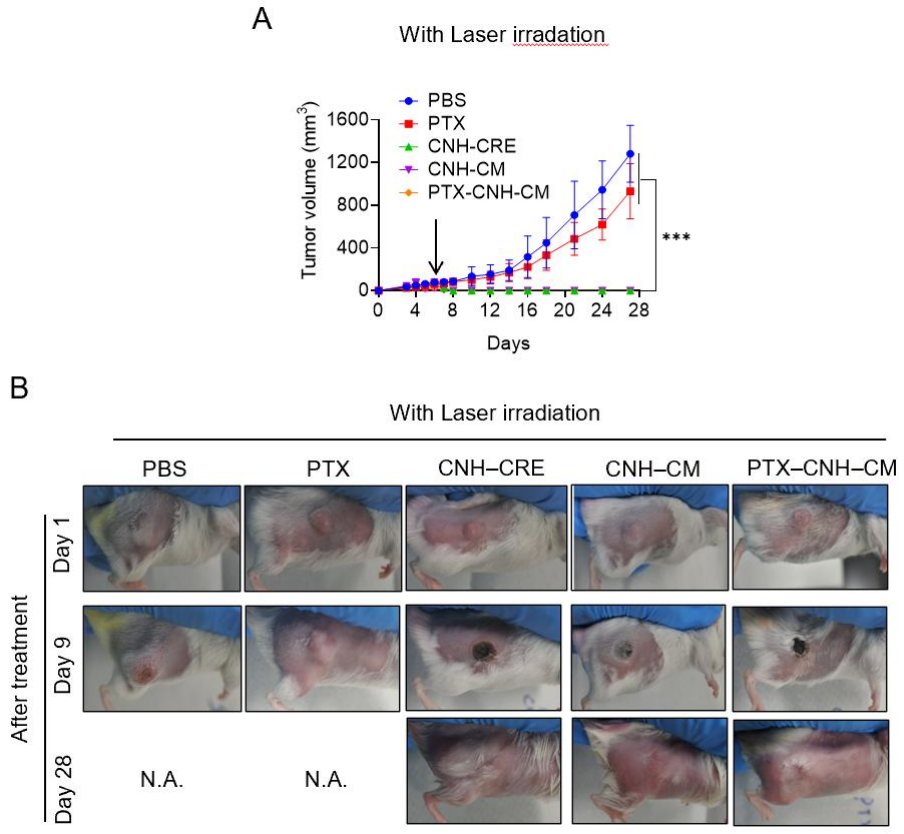

Figure 2.21 In vivo anticancer test of light-induced CNH complexes. A) Anticancer efficacy of various samples with and without laser irradiation. PBS or dispersion of PTX, CNH, CNH–CM, and PTX–CNH–CM was intravenously injected into the Colon 26-bearing mice. After 24 h, the tumors were treated with 808-nm laser irradiation (laser power = 0.6 W (≈ 30.6 mW/mm2); irradiation time = 5 min every day (total 2 times irradiation). Data are expressed as means ± SEM (n ≥ 4 biologically independent tests). *p < 0.05, ***p < 0.001, by Student's t-test. The black arrows display the time

point of sample administration. B) Photos of the mice after each treatment.

In addition, PTX–CNH–CM not only induced a strong antitumor effect but also significantly prolonged the survival of laser-treated mice (Figure 2.22). Among the non-irradiated groups, both CNH–CM and PTX alone exhibited moderate effects in extending survival, consistent with the antitumor efficacy results described above. By contrast, PBS and CNH–CRE alone showed no therapeutic benefit in terms of survival.

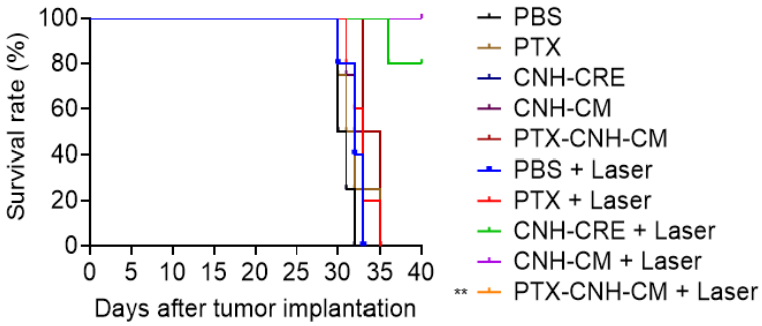

Figure 2.22 Kaplan–Meier survival curves of Colon 26 tumor–bearing mice following treatment with light-activated CNH complexes. (40 days post tumor implantation). Statistical significance was calculated in comparison with the PBS group. *** $P < 0.001$ by Log-rank (Mantel–Cox) test. The PTX–CNH–CM and CNH–CM + laser groups showed a 100% survival rate for at least 30 days. n $\geqslant$ 4 biologically independent mice

The body weights of all groups, with or without laser irradiation, remained relatively stable throughout the experimental period, indicating the good biocompatibility and safety of the CNH complexes (Figure 2.23).

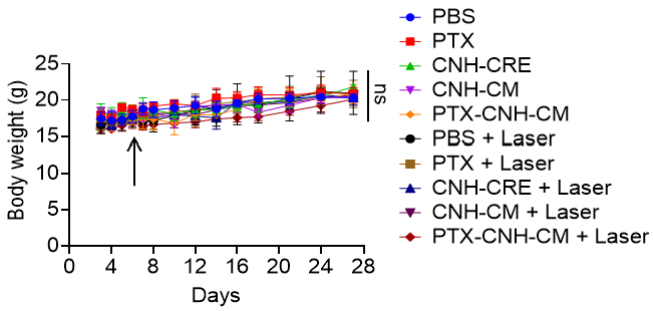

Figure 2.23 Average mouse body weight after treatment during the treatment period. The black arrow displays the time point of sample administration.

Lastly, blood cell counts and biochemical parameter analyses revealed no significant differences 30 days after intravenous injection of PTX–CNH–CM suspension (Table 3). These results suggest that PTX–CNH–CM possesses excellent biocompatibility and safety, supporting its potential as a multidimensional photothermal anticancer agent.

Table 3. Complete blood counts (CBCs) and biochemical parameters of the mice injected with PBS or PTX-CNH-CM dispersion after 7 days.

Measured value	Entry	Unit	PBS (n = 6)	PTX-CNH-CM (n = 7)	P value
CBC	WBC	$\times 10^2\ \mu L^{-1}$	70.8 ± 17.92	73.14 ± 10.46	>0.05
	RBC	$\times 10^4\ \mu L^{-1}$	869.8 ± 3.99	895.86 ± 31.16	>0.05
	HGB	$g\ dL^{-1}$	13.68 ± 0.19	13.94 ± 0.3	>0.05
	HCT	%	40.06 ± 0.83	40.84 ± 1.27	>0.05
	MCV	fL	46.06 ± 0.49	45.6 ± 0.48	>0.05
	MCH	pg	15.74 ± 0.17	15.57 ± 0.35	>0.05
	MCHC	$g\ dL^{-1}$	34.12 ± 0.27	34.16 ± 0.49	>0.05
	PLT	$\times 10^4\ \mu L^{-1}$	84.54 ± 5.17	87.44 ± 9.47	>0.05

Measured value	Entry	Unit	PBS (n = 6)	PTX-CNH-CM (n = 7)	P value
Biochemical parameters	TP	g dL^{-1}	4.48 ± 0.13	4.4 ± 0.11	>0.05
	ALB	g dL^{-1}	3.08 ± 0.08	3.16 ± 0.12	>0.05
	BUN	mg dL^{-1}	24.02 ± 4.22	22.21 ± 1.49	>0.05
	CRE	mg dL^{-1}	0.11 ± 0.01	0.11 ± 0.02	>0.05
	Na	mEq L^{-1}	145.6 ± 0.89	145.75 ± 1.04	>0.05
	K	mEq L^{-1}	20.44 ± 1.58	20.99 ± 0.57	>0.05
	Cl	mEq L^{-1}	104 ± 1.22	105.25 ± 2.12	>0.05
	AST	IU L^{-1}	41.6 ± 3.85	44.5 ± 4	>0.05
	ALT	IU L^{-1}	20.4 ± 3.78	22.5 ± 2.98	>0.05
	LDH	IU L^{-1}	184.6 ± 19.1	169.25 ± 19.57	>0.05
	AMY	IU L^{-1}	2,112.4 ± 246.09	2029.5 ± 297.17	>0.05
	CK	IU L^{-1}	71 ± 4.3	68.13 ± 25.59	>0.05

Data are represented as means ± SEM; n = 5 biologically independent mice. Statistical analyses comprise the two-way ANOVA test. Abbreviations: ALB, albumin; ALT, alanine transaminase; AMY, amylase; AST, aspartate aminotransferase; BUN, blood urea nitrogen; Cl, chlorine; CK, creatine kinase; CRE, creatinine; HCT, hematocrit; HGB, hemoglobin; K, potassium; LDH, lactate dehydrogenase; MCH, mean corpuscular hemoglobin; MCHC, mean corpuscular hemoglobin concentration; MCV, mean corpuscular volume; Na, sodium; PLT, platelet; RBC, red blood cell; TP, total protein; WBC, white blood cell.

2.3.4 The mechanism of tumor suppression by CNH complexes

To investigate the immunological mechanisms underlying light-triggered regression of solid tumors mediated by CNH complexes, HE staining and IHC analyses were performed on tumor sections from the PTX–CNH–CM group (Figure 2.24). HE staining revealed extensive

histoarchitectural damage within the tumor mass, characterized by pronounced intercellular fragmentation, indicative of robust antitumor activity. Similar patterns of tissue degradation were observed in the CNH–CRE + laser and CNH–CM + laser groups, demonstrating therapeutic efficacy comparable to that of the PTX–CNH–CM + laser group. By contrast, tumor sections from the PBS + laser and CNH–CRE groups exhibited no notable histological alterations during the treatment period. Consistent with these findings, TUNEL assays revealed substantial apoptotic cell populations, most prominently in the PTX–CNH–CM + laser group. Furthermore, caspase-3 staining confirmed the potent antitumor effects elicited by laser-activated PTX–CNH–CM.

IHC staining of the laser-irradiated PTX–CNH–CM group demonstrated substantial expression of immune markers (Figure 2.24), including cytotoxic NK and T lymphocytes, indicating robust immune activation likely driven by the combined stimulatory effects of photothermal heating and membrane-derived immunogenic molecules. Increased NK- and T-cell marker expression was also observed in the CNH–CM group, reflecting the intrinsic immunostimulatory capacity of the cell membrane coating. By contrast, the PTX + laser and PBS + laser groups exhibited negligible immune activation compared with the PTX–CNH–CM + laser, CNH–CM + laser, and CNH–CRE + laser groups.

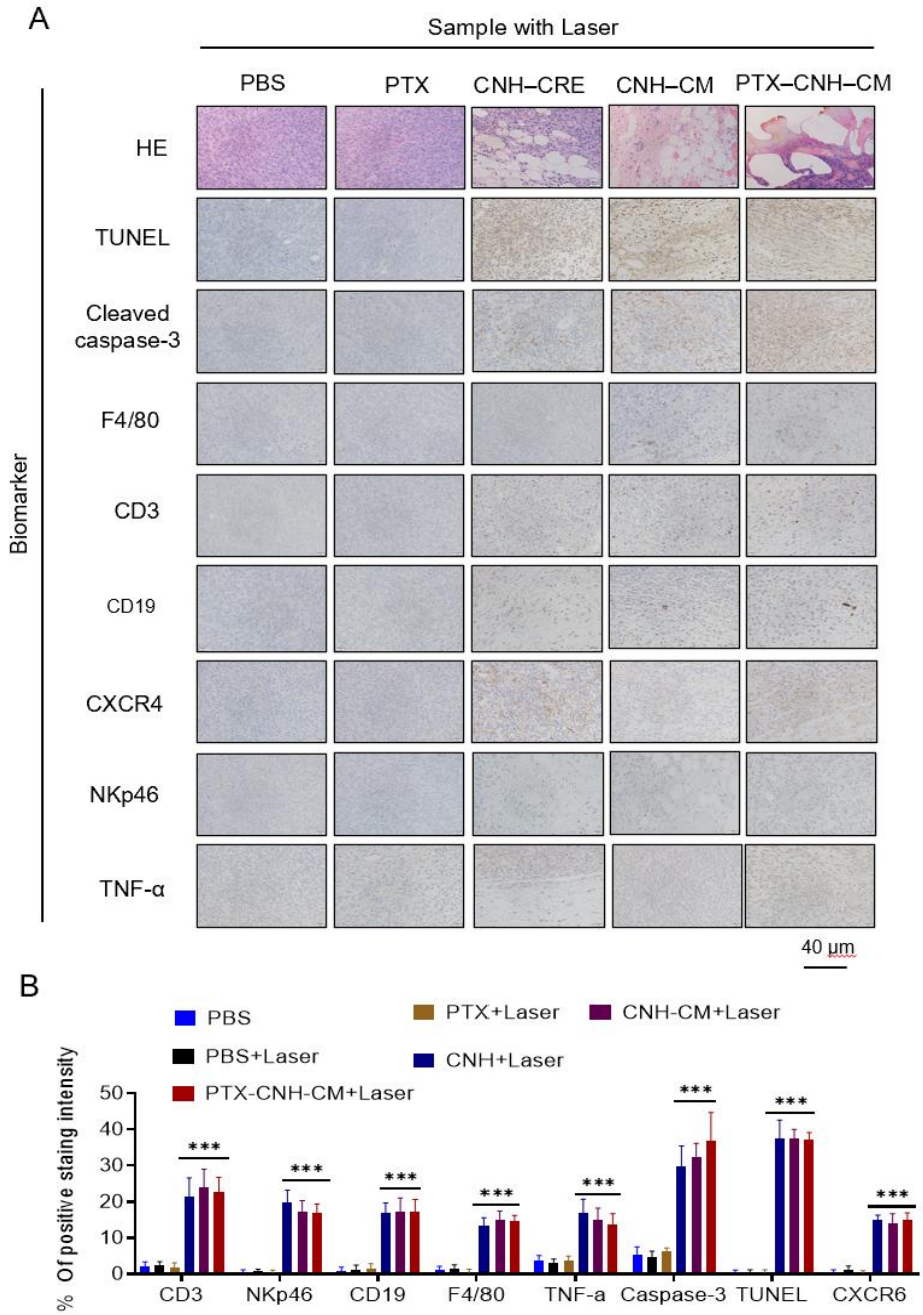

Figure 2.24 Mechanism of tumor suppression by CNH complexes. A) Hematoxylin and eosin (H&E), TUNEL, and IHC (Caspase-3, F4/80, CD3, CD19, CXCR4, NKp46, and TNF-α) stained tumor tissues collected from different groups of mice on day 1 after their respective treatments. B) Intensity of color development in various IHC slides as a comparison of control and treated samples. Data are represented as mean ± standard error of the mean (SEM); n = 10 independent areas (region of interest) in each tumor tissue collected from the groups of mice 1 day after treatments. Statistical significance was calculated in comparison with the control group, ***, $p < 0.001$ by one-way Student's t-test.

Immunological responses were also observed in the CNH–CM and PTX–CNH–CM groups even in the absence of laser irradiation (Figure 2.25). IHC staining for CD3 (T-cell marker), CD19 (B-cell marker), CXCR4 (neutrophil marker), NKp46 (NK cell marker), and TNF-α revealed significant immune activation induced by the tumor cell membrane coating. In contrast, the PBS, PTX, and CNH–CRE groups elicited negligible immune stimulation compared with PTX–CNH–CM and CNH–CM.

Collectively, the rapid tumor regression and accelerated wound healing observed with PTX–CNH–CM treatment under laser irradiation were driven by the synergistic effects of potent photothermal ablation mediated by CNH, effective immune activation derived from the cell membrane coating, and the chemotherapeutic inhibition of PTX. These integrated photothermal, chemo-drug, and immunological effects highlight the strong potential of CNH-based nanocomplexes for the treatment of advanced and aggressive cancers.

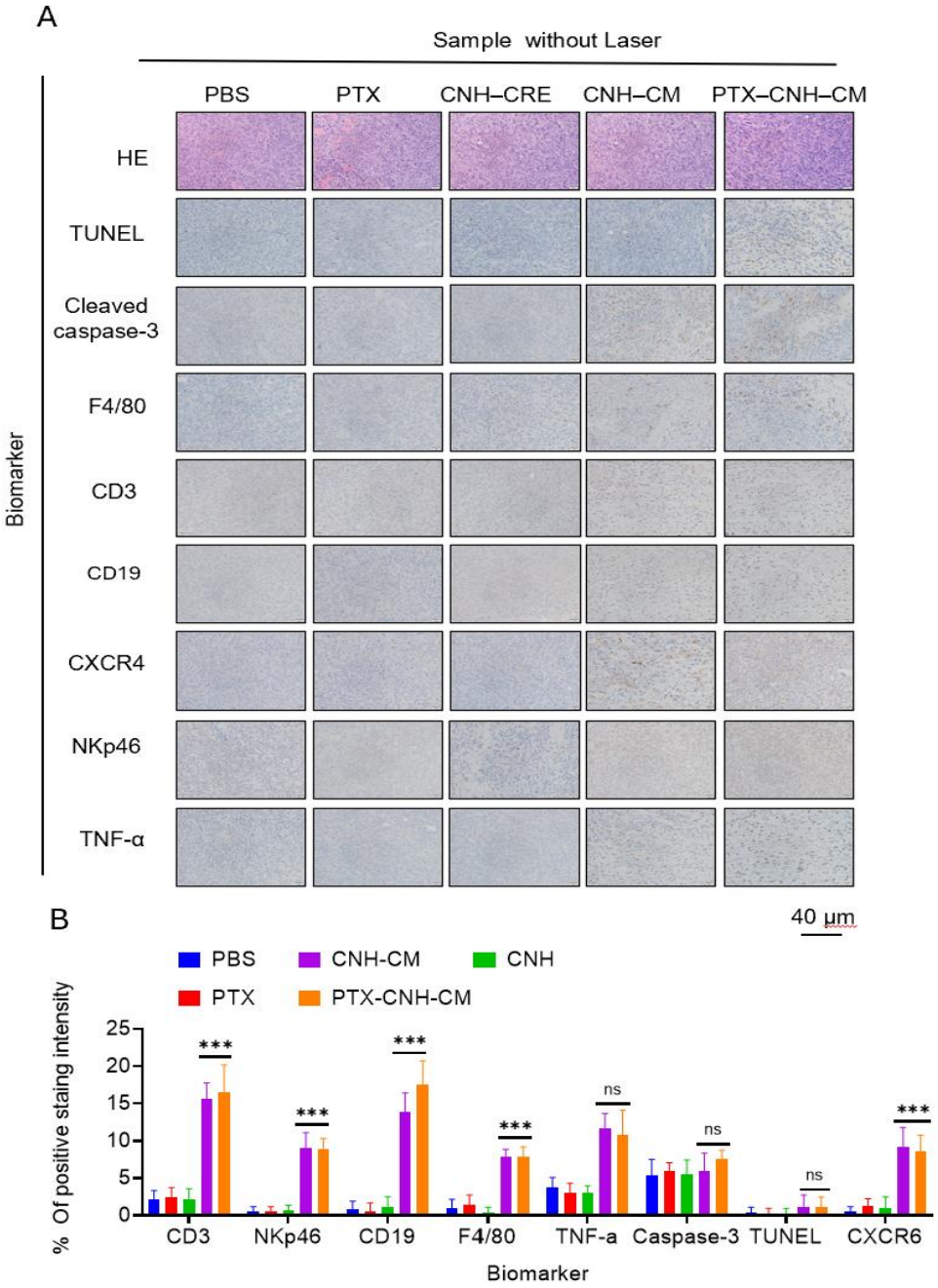

Figure 2.25 Mechanism of tumor suppression by laser-driven CNH complexes. A) Hematoxylin and eosin (H&E), TUNEL, and IHC (Caspase-3, F4/80, CD3, CD19, CXCR4, NKp46, and TNF-α) stained tumor tissues collected from different groups of mice on day 1 after their respective treatments. B) Intensity of color development in various IHC slides as a comparison of control and treated samples. Data are represented as mean ± standard error of the mean (SEM); n = 10 independent areas (region of interest) in each tumor tissue collected from the groups of mice 1 day after treatments. Statistical significance was calculated in comparison with the control group. ** $p < 0.01$, ***, $p < 0.001$, and ****$p < 0.0001$, by one-way Student's t-test.

2.4 Conclusion

In this chapter, we present the rational design and evaluation of carbon nanohorns (CNHs) as multifunctional complext for a synergistic cancer phototheranostic platform. While photothermal therapy (PTT) alone can induce efficient ablation of solid tumors under near-infrared (NIR) irradiation, its therapeutic window is inherently constrained, often failing to eradicate tumor cells beyond the irradiation field or to address metastatic lesions. To overcome these limitations, we engineered cancer cell membrane–camouflaged CNH nanocomplexes capable of targeted PTT while simultaneously eliciting antitumor immune responses. Further functionalization was achieved by loading paclitaxel (PTX) into the CNH–CM constructs, yielding a three-in-one therapeutic system that seamlessly integrates PTT, immunotherapy, and chemotherapy (Figure 2.26).

Comprehensive in vivo assessments demonstrated that PTX-encapsulated CNH–CM nanocomplexes exhibited pronounced tumor accumulation, prolonged intratumoral retention, and potent photothermal conversion under laser excitation. moreover, PTX release enhanced cytotoxic chemotherapeutic efficacy, and the biomimetic CM coating intrinsically activated diverse immune pathways within the tumor microenvironment. Collectively, these synergistic effects underscore the capacity of the CNH–CM–PTX platform to transcend the limitations of monomodal PTT, offering a versatile and precision-driven therapeutic modality for both primary and metastatic malignancies.

Overall, these multifunctional strategies for biomimetic CNH functionalization provide a versatile platform for therapeutic applications, potentially advancing CNH materials toward

clinical translation. Moreover, the unique properties of these biomimetically functionalized CNHs offer a promising avenue for expanding their utility beyond cancer therapy, including applications in immunotherapy, targeted drug delivery, and broader biomedical research.

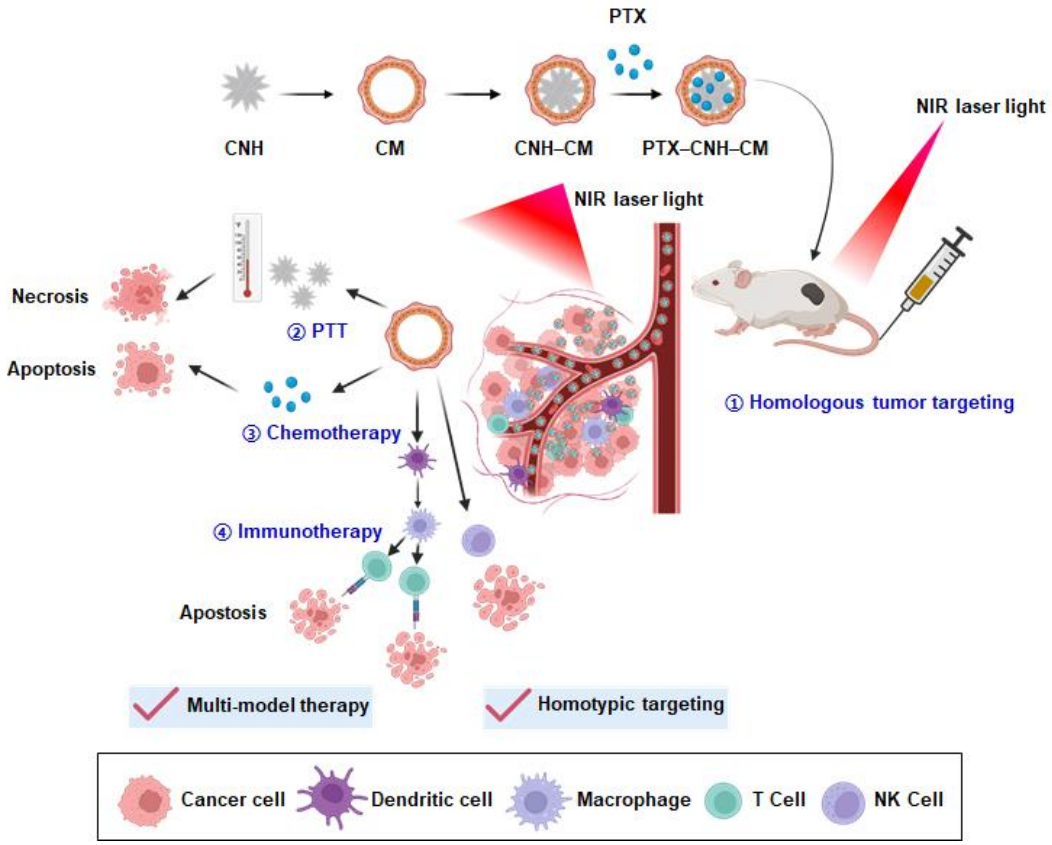

Figure 2.26 Schematic illustration of the biomimetic functional CNH complex for synergistic cancer therapy. Carbon nanohorns (CNH) were coated with homologous cancer cell membranes (CM) to obtain biomimetic CNH–CM nanoparticles, followed by paclitaxel (PTX) loading to form PTX–CNH–CM. After intravenous administration, PTX–CNH–CM exhibited homologous tumor targeting (①) and accumulated efficiently within the tumor site. Upon NIR laser irradiation, the nanocomplex induced synergistic photothermal therapy (PTT) (②), chemotherapy (③), and immunotherapy (④). The combination therapy promoted tumor cell necrosis/apoptosis and enhanced dendritic cell maturation and T cell activation, achieving multi-modal tumor eradication.

2.5 Reference

[1] B. He, Y. Shi, Y. Liang, A. Yang, Z. Fan, L. Yuan, X. Zou, X. Chang, H. Zhang, X. Wang, *Nat. Commun.* **2018**, *9*, 2393.

[2] S. A. Chechetka, E. Yuba, K. Kono, M. Yudasaka, A. Bianco, E. Miyako, *Angew. Chem. Int. Ed.* **2016**, *55*, 6476.

[3] E. Miyako, J. Russier, M. Mauro, C. Cebrian, H. Yawo, C. Ménard-Moyon, J. A. Hutchison, M. Yudasaka, S. Iijima, L. De Cola, A. Bianco, *Angew. Chem. Int. Ed.* **2014**, *53*, 13121.

[4] J. W. Fisher, S. Sarkar, C. F. Buchanan, C. S. Szot, J. Whitney, H. C. Hatcher, S. V. Torti, C. G. Rylander, M. N. Rylander, *Cancer Res.* **2010**, *70*, 9855.

[5] Y. Yu, X. Yang, S. Reghu, S. C. Kaul, R. Wadhwa, E. Miyako, *Nat Commun.* **2020**, *11*, 4117.

[6] B. T. Luk, R. H. Fang, C. M. Hu, J. A. Copp, S. Thamphiwatana, D. Dehaini, W. Gao, K. Zhang, S. Li, L. Zhang, *Theranostics.* **2016**, *6*, 1004.

[7] A. N. Ilinskaya, M. A. Dobrovolskaia, *Toxicol. Appl. Pharmacol.* **2016**, *299*, 70.

[8] S. M. Moghimi, A. C. Hunter, J. C. Murray, *Pharmacol. Rev.* **2001**, *53*, 283.

[9] L. Jing, S. Shao, Y. Wang, Y. Yang, X. Yue, Z. Dai, *Theranostics.* **2016**, *6*, 40.

[10] P. Laverman, M. G. Carstens, O. C. Boerman, E. T. Dams, W. J. Oyen, N. van Rooijen, F. H. Corstens, G. Storm, *J. Pharmacol. Exp. Ther.* **2001**, *298*, 607.

[11] Y. Mima, Y. Hashimoto, T. Shimizu, H. Kiwada, T. Ishida, *Mol. Pharm.* **2015**, *12*, 2429.

[12] W. Gao, R. H. Fang, S. Thamphiwatana, B. T. Luk, J. Li, P. Angsantikul, Q. Zhang, C. M. Hu, L. Zhang, *Nano Lett.* **2015**, *15*, 1403.

[13] J. Jin, B. Krishnamachary, J. D. Barnett, S. Chatterjee, D. Chang, Y. Mironchik, F. Wildes, E. M. Jaffee, S. Nimmagadda, Z. M. Bhujwalla, *ACS Appl Mater Interfaces.* **2019**, *11*, 7850.

[14] J. C. Harris, M. A. Scully, E. S. Day, *Cancers (Basel).* **2019**, *11*.

[15] A. V. Kroll, R. H. Fang, Y. Jiang, J. Zhou, X. Wei, C. L. Yu, J. Gao, B. T. Luk, D. Dehaini, W. Gao, L. Zhang, *Adv. Mater.* **2017**, *29*, 1703969.

[16] M. Mareel, K. Vleminckx, S. Vermeulen, Y. Gao, L. Vakaet, Jr., M. Bracke, F. van Roy, *Prog. Histochem. Cytochem.* **1992**, *26*, 95.

[17] J. Y. Zhu, D. W. Zheng, M. K. Zhang, W. Y. Yu, W. X. Qiu, J. J. Hu, J. Feng, X. Z. Zhang, *Nano Lett.* **2016**, *16*, 5895.

[18] Z. Chen, P. Zhao, Z. Luo, M. Zheng, H. Tian, P. Gong, G. Gao, H. Pan, L. Liu, A. Ma, *ACS nano.* **2016**, *10*, 10049.

[19] C. M. Hessel, V. P. Pattani, M. Rasch, M. G. Panthani, B. Koo, J. W. Tunnell, B. A. Korgel, *Nano Lett.* **2011**, *11*, 2560.

[20] D. K. Roper, W. Ahn, M. Hoepfner, *J. Phys. Chem. C Nanomater. Interfaces.* **2007**, *111*, 3636.

[21] Q. Tian, F. Jiang, R. Zou, Q. Liu, Z. Chen, M. Zhu, S. Yang, J. Wang, J. Wang, J. Hu, *ACS Nano.* **2011**, *5*, 9761.

[22] Y. Shi, Z. Shi, S. Li, Y. Zhang, B. He, D. Peng, J. Tian, M. Zhao, X. Wang, Q. Zhang, *Int J Nanomedicine.* **2017**, *12*, 4177.

[23] X. Ning, C. Mao, J. Zhang, L. Zhao, *J. Mol. Struct.* **2022**, *1269*, 133829.

[24] K. Ajima, M. Yudasaka, T. Murakami, A. Maigné, K. Shiba, S. Iijima, *Mol. Pharm.* **2005**, *2*, 475.

[25] Y. Li, G. Bai, S. Zeng, J. Hao, *ACS Appl Mater Interfaces.* **2019**, *11*, 4737.

[26] Y. Ma, S. Yu, S. Ni, B. Zhang, A. C. F. Kung, J. Gao, A. Lu, G. Zhang, *Frontiers in cell and developmental biology.* **2021**, *9*, 626910.

[27] G. Pagona, G. E. Zervaki, A. S. D. Sandanayaka, O. Ito, G. Charalambidis, T. Hasobe, A. G. Coutsolelos, N. Tagmatarchis, *J. Phys. Chem. C.* **2012**, *116*, 9439.

[28] A. S. Sandanayaka, O. Ito, M. Zhang, K. Ajima, S. Iijima, M. Yudasaka, T. Murakami, K. Tsuchida, *Adv. Mater.* **2009**, *21*, 4366.

[29] J. Jin, Q. Zhao, *Journal of nanobiotechnology.* **2020**, *18*, 75.

Chapter 3 Bacterial-adjuvant liquid metal nanocomplexes for synergistic photothermal immunotherapy

3.1 Introduction

Gallium-based liquid metals (LMs) have attracted considerable attention as multifunctional materials for biomedical applications due to their exceptional biocompatibility profile and unique physicochemical characteristics, positioning them as promising candidates for PTT applications in cancer therapy[1-8]. However, despite their potential, LM-based systems face significant formulation challenges. When processed into nanosized particles through sonication techniques, these materials exhibit poor aqueous dispersibility and water immiscibility, resulting in spontaneous reaggregation into microsized particles due to their inherent fluidity. This aggregation behavior leads to compromised cellular uptake, inadequate tissue distribution, reduced biocompatibility, and diminished therapeutic efficacy[9-10]. Therefore, effective surface modification strategies for LMs remain a critical requirement for achieving stable aqueous dispersion and optimal therapeutic performance.

The tumor microenvironment harbors diverse bacterial populations that represent potential therapeutic targets for cancer treatment. Our recent investigations have identified specific bacterial strains isolated from tumor tissues that exhibit potent tumor-suppressive properties[11-12]. Among these, intratumoral nonpathogenic Lactococcus sp. (Lacto) demonstrates remarkable antitumor efficacy through cytotoxic immunological activation within the tumor microenvironment[11]. Lacto, a genus of lactic acid bacteria belonging to the Streptococcaceae family, is widely utilized in the dairy industry and naturally occurs within the

gastrointestinal tract as a component of the normal microbiota[13-14]. As a gram-positive bacterium, Lacto effectively stimulates immune responses in cancer therapy through its abundance of pathogen-associated molecular patterns (PAMPs), including peptidoglycan and teichoic acids[14-15]. The inherent safety profile and practical advantages of lactic acid bacterial strains make them attractive vectors for drug delivery in clinical cancer immunotherapy applications without requiring additional attenuation procedures[16]. However, the clinical translation of live bacterial therapeutics based on Lacto faces significant challenges, particularly in maintaining precise control over bacterial systemic efficacy and ensuring patient safety.

3.2 Objective of this chapter.

The objective of this chapter is to develop a novel Lactobacillus-derived surface modification strategy to enhance the aqueous dispersibility, stability, and tumor-targeting capability of liquid metal (LM) nanoparticles. By integrating *Lactococcus* (Lacto) ingredients onto the LM surface through a facile sonication process, the resulting Lacto–LM nanocomposites are designed to simultaneously improve colloidal behavior and exploit the intrinsic immunoadjuvant properties of bacterial components to potentiate systemic immune activation. This immunomodulatory mechanism is expected to augment the immunogenicity of autologous tumor antigens generated during LM-mediated photothermal ablation, thereby amplifying antitumor immune responses. Overall, this work aims to demonstrate that the Lacto–LM nanoplatform can achieve synergistic tumor eradication, effectively inhibit recurrence, and suppress metastatic progression, offering a versatile and potent framework for

next-generation LM-based immune-activating photothermal nanomaterial based therapy

3.3 Materials and methods

3.3.1 Bacterial strains and growth

The bacterial strain of *Lactococcus sp.* (Lacto) used in this study was originally isolated from murine colon carcinoma (Colon26)-derived tumors, as detailed in our previous study [34]. Lacto was anaerobically cultured on Luria broth (LB) agar plate and in LB medium at 26–30 °C. Subculturing was performed in Pearl Core E-MC64 medium (Eiken Chemical, Tokyo, Japan) at 32 °C in an incubator (i-CUBE FCI-280HG; AS ONE). Bacterial cell number and viability were assessed using a bacterial counter (CASY Cell Counter & Analyzer; OMNI Life Science, Basel, Switzerland) in conjunction with an active colony assay. Bacterial pellets were harvested by centrifugation at 3,000 rpm for 5 min at 25 °C and subsequently weighed using a precision balance (GR-202; A&D Co., Ltd., Tokyo, Japan). All reagents for bacterial culture were procured from Nacalai Tesque (Kyoto, Japan), Tokyo Chemical Industry (Tokyo, Japan), and FUJIFILM Wako Pure Chemicals.

3.3.2 Nanocomposite synthesis

Lacto–LM nanocomposites were synthesized by dispersing 30 mg of LM (Ga:In = 75.5:24.5 wt%; Alfa Aesar, Ward Hill, MA, USA) and 1.53×10^9 CFU Lacto cells in 10 mL of PBS, followed by pulse-type sonication (VCX-600; Sonics, Danbury, CT, USA) for 10 min in an ice bath. Similarly, DSPE–PEG–LM nanoparticles were prepared by dispersing 30 mg of LM in 10 mL of PBS containing 5 mg of DSPE–PEG_{2000}–NH_2 (Yuka Sangyo Co., Ltd, Tokyo, Japan), followed by sonication under identical conditions. To obtain highly concentrated

Lacto–LM or DSPE–PEG–LM suspensions, the amounts of LM and Lacto were increased proportionally while maintaining the same ratio. ICG–Lacto–LM, 0.2 mg of ICG (Tokyo Chemical Industry, Tokyo, Japan) was added to 1 mL of the synthesized Lacto–LM solution, followed by vortexing for 1 min in the dark. ICG–DSPE–PEG–LM was prepared using the same method as that used for the addition of DSPE–PEG–LM. Additionally, a highly concentrated ICG–Lacto–LM suspension was obtained by proportionally increasing the amounts of Lacto–LM and ICG.

3.3.3 Structural and optical characterization

The morphology and composition of Lacto–LM, DSPE–PEG–LM, and pristine LM were meticulously analyzed using high-resolution TEM (Model JEM-2010; JEOL Ltd., Tokyo, Japan) at an acceleration voltage of 200 kV. TEM analyses were conducted at Hanaichi Ultra Structure Research Institute Co., Ltd., Aichi, Japan. The hydrodynamic diameter of the nanoparticles was determined using DLS (Zetasizer Nano ZS; Malvern Panalytical, UK). Additionally, the optical properties including absorbance and FL were characterized using UV–vis–NIR (Model V-730 BIO; Jasco Corporation, Tokyo, Japan) and fluorescence (Model FP-6300; Jasco Corporation) spectrometers, respectively

3.3.4 Photothermal conversion efficiency

The photothermal transduction of Lacto–LM nanocomposite dispersion was assessed by irradiating the solution (Milli-Q water served as a control) with an 808 nm NIR laser (Civil Laser, Hangzhou, Zhejiang, China) at varying power outputs of 1.2 W (approximately 61.1 mW/mm^2, spot diameter ~5 mm), 0.6 W (ca. 30.6 mW/mm^2), and 0.3 W (ca. 15.3 mW/mm^2). The thermal responses of the solutions were continuously monitored *in situ* using a high-

precision temperature sensor (Model AD-5601A; A&D Co.), and infrared thermographic imaging (Model i7; FLIR Systems, Nashua, NH, USA) was employed to visually capture the thermal distribution patterns. The photothermal conversion efficiency (η) of Lacto–LM was determined following previously established methods [13–15]. using the equation:

$$\eta = hS(T_{Max} - T_{Surr}) - Q_{Dis} / I(1 - 10^{-A808}) \quad (1)$$

Where η is the photothermal conversion efficiency of nanoparticles, h is the heat transfer coefficient, S is the surface area of the container, and the value of hS is obtained from the Eq. 2. T_{max} is the maximum steady temperature of the nanoparticle solution, and T_{Surr} is the environmental temperature. I and A_{808} represent the laser power and absorbance, respectively, at a laser wavelength of 808 nm. Q_{Dis} represents the heat dissipated from the light absorbed by the solvent and container.

$$hS = m_D C_D / \tau_s \quad (2)$$

where, m_D and C_D are the mass and heat capacities of the solvent, respectively. A sample system time constant τ_s can be calculated by Eq.3.

$$t = -\tau_s \ln(\theta) \quad (3)$$

A dimensionless parameter θ is introduced as followed:

$$\theta = T - T_{Surr} / T_{Max} - T_{Surr} \quad (4)$$

To evaluate the photothermal stability of Lacto–LM nanocomposites, a 200 µL aliquot of the nanocomposite suspension was irradiated with an 808 nm NIR laser at an intensity of 1.2 W (approximately 61.1 mW/mm², spot diameter ~5 mm) for 5 min. After irradiation, the

suspension was diluted with Milli-Q water, and the optical absorbance spectrum of the resultant solution was analyzed using a UV–vis–NIR spectrophotometer to assess changes in the photothermal performance.

3.3.5 Cell culture and viability

Colon26 and TIG103 cell lines were obtained from the Japanese Collection of Research Bioresources Cell Bank (Tokyo, Japan). Colon26 cells were cultured in Roswell Park Memorial Institute (RPMI) 1640 medium (Gibco, Grand Island, NY, USA) supplemented with 10% fetal bovine serum (FBS), 2 mM L-glutamine, 1 mM sodium pyruvate, gentamycin, and 100 IU/mL penicillin-streptomycin, whereas TIG103 cells were maintained in Eagle's minimal essential medium (Nacalai Tesque, Tokyo, Japan) containing the same supplements. Both cell lines were cultured at 37 °C in a humidified incubator with 5% CO_2. To avoid genetic instability associated with high passage numbers, cell stocks were regularly revived from cryopreserved vials stored in liquid nitrogen.

Cell viability was evaluated using a Cell Counting Kit-8 (CCK-8) assay (Dojindo Laboratories, Kumamoto, Japan) following the manufacturer’s protocol. Briefly, 1×10^4 cells/well were seeded in 96-well plates and allowed to adhere overnight before exposure to nanoparticles and laser irradiation, as specified. Following treatment, the cells were washed with fresh medium and incubated with CCK-8 solution for 3 h at 37 °C. The absorbance was measured at 450/690 nm using a microplate reader to quantify cell viability.

3.3.6 Intracellular penetration of nanocomposites

Colon 26 cells (3×10^5 cells/well) were seeded onto polylysine-coated glass-bottom dishes

(Matsunami Glass, Osaka, Japan) and incubated overnight to allow adhesion. Subsequently, the medium was replaced with fresh medium containing free ICG, ICG–LM, or ICG–Lacto–LM at a final concentration of 12.5 μg/ mL for ICG and 3 mg/ mL for LM. Cells were incubated for 0.5, 2, 6, or 12 h. PBS-treated cells were used as the control group. After incubation, the cells were washed 4 times with PBS to remove unbound nanocomposites. Live-cell imaging was then performed using a fluorescence microscope (BZ-X800, Keyence, Tokyo, Japan). Fluorescence images were acquired using CH3 channel at excitation wavelength of 633 nm and an emission range of 650-750 nm. Differential interference contrast (DIC) images were collected under identical conditions. The fluorescence and DIC channels were merged using a light microscopy system (BZ-X800) and fluorescence intensity was quantified using Keyence software. Regions of interest were selected around individual cells, and the mean fluorescence intensity was measured.

3.3.7 Direct observation of laser-induced cancer cell destruction

Colon 26 cells were seeded in glass-bottom dishes at a density of 3×10^5 cells/mL and cultured overnight to allow cell adhesion. The medium was then replaced with fresh medium containing either PBS or Lacto–LM (final LM concentration**:** 375 μg/mL**)** and incubated for 5 h**.** After incubation, the medium was removed, and the cells were washed three times with PBS to eliminate unbound nanocomposites. Subsequently, 5 μL of propidium iodide (PI, 1 mg/mL, Dojindo Laboratories) was gently added to the center of the glass-bottom dish to label dead cells, followed immediately by laser irradiation. Laser irradiation was performed using an 808 nm NIR continuous-wave diode laser with power densities of 72, 144, or 287 mW/mm² for 3 s, focusing on a defined irradiation spot. DIC and PI fluorescence images were captured before

and immediately after irradiation using a IX73 microscope (Olympus, Tokyo, Japan) equipped with a 40× objective (numerical aperture: 0.95, UPLSAPO40X, Olympus). PI fluorescence was acquired with an excitation wavelength of 535–560 nm and an emission range of 570–620 nm. For quantitative analysis, the relative PI fluorescence intensity in the laser-irradiated region was measured using ImageJ software (Fiji) and normalized to the PBS group. All experiments were performed in triplicate (N = 3).

3.3.8 *In vivo* NIR bioimaging

All animal experiments were conducted in accordance with protocols approved by the Institutional Animal Care and Use Committee of the Japan Advanced Institute of Science and Technology (JAIST) (Approval No. 06–003). To evaluate the temporal dynamics of NIR FL intensity associated with the tumor-targeting efficacy of ICG–Lacto–LM, female BALB/c mice (6 weeks old, average weight: 18 g, Japan SLC, Hamamatsu, Japan) bearing Colon 26 tumors (average tumor volume: 100 mm^3) were intravenously injected with 200 μL of PBS or 200 μL of PBS containing ICG–Lacto–LM (ICG: 2 mg/mL or 22.2 mg/kg, LM: 6 mg/mL or 6.67 mg/kg, Lacto at 3.06×10^8 CFU/mL or 3.4 × 109 CFU/kg) or ICG–DEPE–PEG–LM (ICG: 2 mg/mL or 22.2 mg/kg, LM:6 mg/mL or 6.67 mg/kg). At designated time points (4, 9, 13, 16, and 24 h post-injection), the mice were euthanized and the major organs (heart, lung, liver, spleen, and kidneys) and tumor tissues were harvested for imaging. FL signals were captured using an in vivo bioimaging system (VISQUE InVivo Smart-LF, Vieworks, Anyang, Republic of Korea) with a 3-s exposure time and an ICG filter (excitation: 740–790 nm, emission: 810–860 nm). Image acquisition and analysis were performed using the CleVue software (Vieworks).

3.3.9 *In vivo* anticancer therapy

In vivo anticancer therapy experiments were performed using female BALB/c mice (n = 5, 5 weeks old, average weight: 15–20 g) obtained from Japan SLC (Hamamatsu, Japan). Tumors were initiated by subcutaneously injecting a 1:1 mixture of Matrigel® (Dow Corning, Corning, NY, USA) and culture medium containing 1×10^7 Colon26 cells in the right dorsal side of each mouse. After approximately one week, when the tumor volume reached approximately 100 mm^3, the mice were intravenously administered 200 μL of PBS alone, 200 μL of PBS containing DSPE–PEG–LM (LM at 6 mg/mL or 6.67 mg/kg), or 200 μL of PBS containing Lacto (Lacto at 3.06×10^8 CFU/mL or 3.4×10^9 CFU/kg), or 200 μL of PBS containing Lacto–LM (LM at 6 mg/mL or 6.67 mg/kg, Lacto at 3.06×10^8 CFU/mL or 3.4×10^9 CFU/kg). Laser irradiation of the dorsal right-side tumors was performed for 5 min every other day, beginning 24 h after sample injection, for a total of two sessions using an 808 nm laser (600 mW, ~30.6 mW/mm^2). Infrared thermography (i7; FLIR, Nashua, NH, USA) was used for thermographic measurements during laser irradiation. Tumor growth and overall health indicators (viability and body weight) were monitored on alternate days. Tumor volumes were calculated using the formula $V = L \times W^2/2$, where L and W denote the tumor length and width, respectively. Mice were euthanized when the tumor volume exceeded 1,800 mm^3, following the guidelines of the JAIST Institutional Animal Care and Use Committee.

3.3.10 qPCR assay

Female Colon 26 tumor-bearing mice (aged approximately 7 weeks, n = 3, average weight: 18 g, average tumor size: 150 mm^3; BALB/cCrSlc; Japan SLC) were euthanized 24 h after i.v. injection of the samples, as described in the *in vivo anticancer therapy* section. Tumors were

harvested from the mice in different experimental groups, homogenized using a handheld homogenizer (Thermo Fisher Scientific, Waltham, MA, USA), and subsequently processed for qPCR analysis. qPCR was performed on a QuantStudio™ 1 Real-time PCR System (Thermo Fisher Scientific) to assess the relative gene expression of IFN-γ, TNF-α, Ly6g, ADGRE1, NCR1, CD19, and CD3, using gene-specific primer-probe combinations (Thermo Fisher Scientific) (listed in Table 4) and TaqMan™ chemistry. Endogenous control was determined using the TaqMan™ Array Mouse Endogenous Control Plate 96-well (Thermo Fisher Scientific). GAPDH served as the internal reference. Reactions were run in triplicate and thermal cycling conditions were as follows: 50 °C for 2 min (AmpErase UNG activation), 95 °C for 2 min (AmpliTaq Gold DNA polymerase activation), followed by 40 cycles of 95 °C for 1 s (denaturation), and 60 °C for 20 s (annealing and extension). PCR efficiency was determined by running 10-fold serial dilutions of the test genes and endogenous control standards, with percentage efficiency ranging between 90% and 100%. The results were analyzed and presented as fold change (log_{10} relative quantification) relative to the control group.

Table 4.TaqManTM Primers for qPCR.

Target	Assay ID	Gene Symbol	Source
F4/80	Mm00802529_m1	Adgre1	Thermo Fisher Scientific
CD3	Mm00442746_m1	Cd3d	Thermo Fisher Scientific
CD19	Mm00515420_m1	Cd19	Thermo Fisher Scientific
CXCR4	Mm01996749_s1	Cxcr4	Thermo Fisher Scientific

NKp46	Mm01337324_g1	Ncr1	Thermo Fisher Scientific
IFN-γ	Mm01168134_m1	Ifng	Thermo Fisher Scientific
TNF-α	Mm00443258_m1	Tnf	Thermo Fisher Scientific
GAPDH	Mm99999915_g1	Gapdh	Thermo Fisher Scientific

3.3.11 IHC staining

Female Colon26 tumor-bearing mice (aged approximately 7 weeks, n = 5, average weight: 18 g, average tumor size: 150 mm^3; BALB/cCrSlc; Japan SLC) were euthanized one day after intravenous (i.v.) injection of the samples and laser irradiation. Tumor tissues from the treatment groups were collected for IHC staining. Additionally, the major organs, including the heart, liver, kidneys, spleen, and lungs, were harvested, fixed in 4% paraformaldehyde, and sent to a specialized facility for H&E staining to evaluate the safety profile of the nanohybrid. IHC analysis was performed by the Biopathology Institute Co. Ltd. (Oita, Japan) according to standard protocols. Briefly, primary tumors were surgically excised, fixed in 10% formalin, processed for paraffin embedding, and sectioned into 3–4 μm slices. After incubation with the primary antibodies (Table 5), the sections were stained with H&E and examined under a light microscope (IX73). Positively stained areas within the tumor tissues were analyzed using a light microscope (BZ-X800, Keyence,) and the hybrid cell and microcell count software (Keyence). The color development in 10 independent regions of interest was quantified for each treated tumor tissue.

Table 5. Antibodies used in the IHC staining.

Antibody	Type	Source	Catalog No.	Application
F4/80	Mouse Monoclonal	BMA Biomedicals	T-2028	IHC (1:50)
CD3	Rabbit Monoclonal	Abcam	ab16669	IHC (1:100)
CD19	Rabbit Polyclonal	Bioss	bs-0079R	IHC (1:100)
CXCR4	Goat Polyclonal	Abcam	ab1670	IHC (1:100)
NKp46	Rabbit Polyclonal	Affinity Biosciences	DF7599	IHC (1:100)
Caspase-3	Rabbit Polyclonal	Cell Signaling Technology	9661S	IHC (1:100)
TNF-α	Rabbit Polyclonal	Abcam	ab6671	IHC (1:100)
CD8	Rabit Monoclonal	Cell Signaling Technology	S7100	IHC (1:200)
CD4	Rabit Monoclonal	Cell Signaling Technology	98941	IHC (1:100)
Perforin	Rabit Monoclonal	Cell Signaling Technology	31647S	IHC (1:200)

Antibody	Type	Source	Catalog No.	Application
Granzyme B	Rabit Monoclonal	Cell Signaling Technology	44153	IHC (1:200)
Calreticulin	Rabit Polyclonal	Protein Tech	27298-1-AP	IHC (1:200)
HMGB1	Rabit Polyclonal	Protein Tech	10829-1-AP	IHC (1:200)
CD11c	Rabit Polyclonal	Protein Tech	17342-1-AP	IHC (1:200)
Anti-digoxigenin-peroxidase	Sheep Polyclonal	Merck Millipore	S7100	Tunel

3.3.12 ELISA for cytokine quantification

RAW 264.7 macrophages were seeded in 24-well plates at a density of 1.5×10^5 cells per well and incubated for 24 h. Subsequently, the cells were treated with PBS, LM, or Lacto–LM. For the concentration-dependent study, Lacto–LM was applied at final concentrations of 6, 12, 24, 48, and 75 μg/mL for 4 h (TNF-α) or 24 h (IL-6). For the time-dependent study, the cells were incubated with Lacto–LM (75 μg/ mL) for 4, 8, 12, and 24 h. After treatment, the culture supernatants were collected and analyzed using commercial enzyme-linked immunosorbent assay (ELISA) kits for TNF-α (KE10002, Proteintech Group, Inc., Chicago, IL, USA) and IL-6 (KE10007, Proteintech Group, Inc., Chicago, IL, USA) according to the manufacturer's instructions. Absorbance was measured at 450 nm using a microplate reader.

3.3.13 Immunofluorescence analysis of CD80 and CD86 expression in RAW 264.7 macrophages

RAW 264.7 macrophages were seeded into 24-well plates at a density of 1.5×10^5 cells per well and incubated for 24 h. The cells were then treated with PBS, LM (150 μg/mL), or Lacto–LM (75 μg/mL or 150 μg/mL) for 4 h. After treatment, the cells were washed three times with PBS and subsequently blocked with 5% fetal bovine serum (FBS) in PBS for 20 min at room temperature. The cells were incubated with anti-CD80-FITC (5 μg/mL, BioLegend) and anti-CD86-APC (5 μg/mL, BioLegend) antibodies (Table 6) for 15 min at room temperature in the dark. Following three additional PBS washes, fluorescence images were acquired using a Keyence fluorescence microscope, and the mean fluorescence intensities of CD80 and CD86 were quantified using Keyence software (hybrid cell count).

Table 6. Antibodies used in the immunofluorescence analysis.

Antibody	Type	Source	Catalog No.	Application
FITC–CD80	Armenian amster Monochlonal	BioLegend	104705	FL live cell imaging
APC–CD86	Armenian Hamster Monochlonal	BioLegend	105011	FL live cell imaging

3.3.14 Tumor rechallenge

Mice that achieved complete regression following laser-induced Lacto–LM treatment (day 75) were used for the tumor rechallenge experiment. This experiment included three biologically independent mouse models. A 100 μL mixture of culture medium and Matrigel (1:1 v/v) containing 1×10^7 Colon26 cells was subcutaneously injected in the right flank of

each mouse. Tumor recurrence was carefully monitored for 16 d following the injection. Control experiments were conducted with BALB/c mice (female, approximately 5 weeks of age, n = 3, average weight: 18 g; BALB/cCrSlc; Japan SLC), which were intravenously administered 200 μL of PBS. Seventy-five days after PBS injection, the mice were similarly injected with 100 μL of the culture medium/Matrigel mixture (1:1 v/v) containing 1×10^7 Colon26 cells in the right flank. Tumor volumes were measured over 16 d following the same methodology outlined in the *in vivo anticancer therapy* section for the Colon26 syngeneic mouse model.

3.3.15 Flow cytometry

Mice that achieved complete regression following laser-induced Lacto–LM treatment (day 75) were used for flow cytometry. Cells were collected from the spleen of the treated mice. Red blood cells were removed using ACK lysing buffer (Thermo Fisher Scientific), and the debris was removed using a cell strainer (mesh size = 40 μm, SureStrain; MTC Bio, Sayreville, NJ, USA). A total of 1×10^6 cells were stained with anti-CD27 and anti-CD127 antibodies (Table 7) according to the manufacturer's protocols. The stained cells were then analyzed (4×10^4 cells/per sample) using flow cytometry (MACSQuant® Analyzer 16, Miltenyi Biotec, Bergisch Gladbach, Germany) and the MACSQuantify™ software (V2.13.3; Miltenyi Biotec).

Table 7.Antibodies used in the flow cytometry analysis.

Antibody	Type	Source	Catalog No.	Application
FITC–CD3	Human cell line Monochlonal	Miltenyi Biotech	130-119-798	Flow cytometry

PerCP-Vio 700–CD45R (B220)	Human cell line Monochlonal	Miltenyi Biotech	130-110-850	Flow cytometry
CD127-APC-A	Human cell line Monochlonal	Miltenyi Biotech	130-122-938	Flow cytometry
CD27-PE-Vio615-A	Human cell line Monochlonal	Miltenyi Biotech	130-123-043	Flow cytometry
APC-Vio770–CD45	Human cell line Monochlonal	Miltenyi Biotech	130-110-800	Flow cytometry

3.3.16 Blood tests

The complete blood count (CBC) of mice was obtained using a blood cell counting machine (Microsemi LC 712; Horiba Medical, Japan). The biochemical parameters were investigated by Japan SLC and Oriental Yeast Co. (Tokyo, Japan). Female BALB/c mice (6 weeks old, n = 6, average weight: 18 g; Japan SLC) were i.v. injected in the tail vein with 200 μL of Lacto–LM (LM = 6 mg/mL or 3 mg/kg, Lacto = 3.06×10^8 CFU/mL or 3.06×10^9 CFU/kg) or 200 μL of PBS as a control. Blood samples were collected from the inferior vena cava 7 d post-injection for analysis.

3.3.17 Statistical analyses

All experiments were conducted in triplicate and repeated at least three times. Quantitative data are presented as the mean ± standard deviation (SD) or standard errors of the mean (SEM) from a minimum of three independent experiments. Statistical differences were assessed using Student's two-sided *t*-test and one-way ANOVA by Tukey's post hoc test, as appropriate, and

the log-rank (Mantel-Cox) test. All analyses were performed using GraphPad Prism (version 9.4.0; GraphPad Software, Boston, MA, USA). Statistical significance was set at a $p < 0.05$.

3.4 Results and discussion

3.4.1 Characterization of nanocomposites

Conventional membrane-coating strategies typically rely on complex multi-step purification and coating procedures, primarily due to the requirement for membrane isolation. These labor-intensive processes not only increase the risk of contamination but also compromise manufacturing reproducibility and scalability. To overcome these limitations, in this study, we established a one-step sonication approach for the fabrication of Lacto–LM nanocomposites. This streamlined strategy provides distinct advantages over traditional membrane-coating methods. Unlike conventional techniques that merely deposit biomembrane components onto the nanoparticle surface, the direct sonication process achieves superior integration of bioactive constituents derived from Lactobacillus, including peptidoglycans, lipoteichoic acids, and surface proteins, throughout the liquid metal matrix. Such integration endows the nanocomposites with enhanced structural stability via stronger molecular interactions between the bacterial components and the liquid metal core. Consequently, this architecture not only improves the retention of bioactivity during storage and systemic circulation but also ensures more robust functional performance. Collectively, this one-step sonication approach highlights the potential of Lacto–LM nanocomposites as a scalable and practical platform technology, warranting further investigation of their therapeutic efficacy in photothermal immunotherapy.

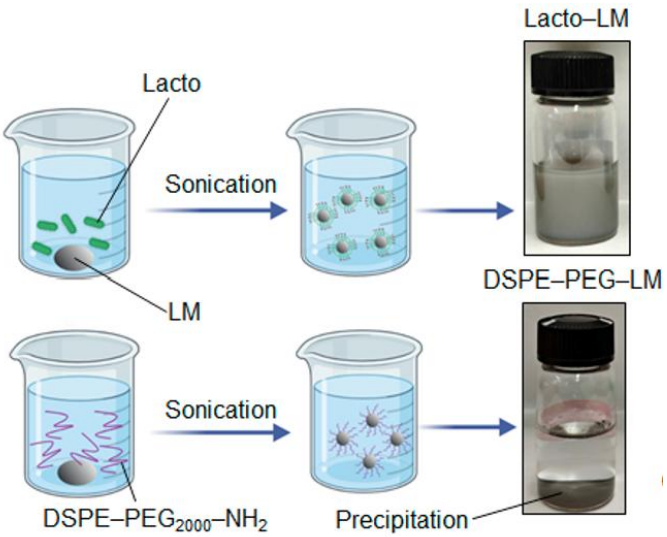

Figure 3.1 Schematic of the synthesis process and images of DSPE–PEG–LM in PBS and Lacto–LM dispersed in PBS.

The synthesized Lacto–LM nanocomposites exhibited a characteristic gray coloration and maintained excellent aqueous dispersibility, thereby confirming the effectiveness of the surface modification (Figure 3.1). To further verify the superiority of the Lacto-based coating strategy, a comparative study was conducted with conventional surfactant-assisted stabilization systems. Among them, 1,2-distearoyl-sn-glycero-3-phosphoethanolamine-N-[amino(polyethylene glycol)-2000] (DSPE-PEG2000-NH2)[17-18] has been widely employed as a biocompatible surfactant for improving the water dispersibility of various nanomaterials, including liquid metals (LMs). However, the DSPE-PEG2000-NH2-modified LM (DSPE–PEG–LM) system exhibited poor colloidal stability, with visible aggregation and sedimentation at the bottom of the container after 24 h of storage. Such instability highlights the inherent limitations of conventional surfactant-based approaches for LM stabilization,

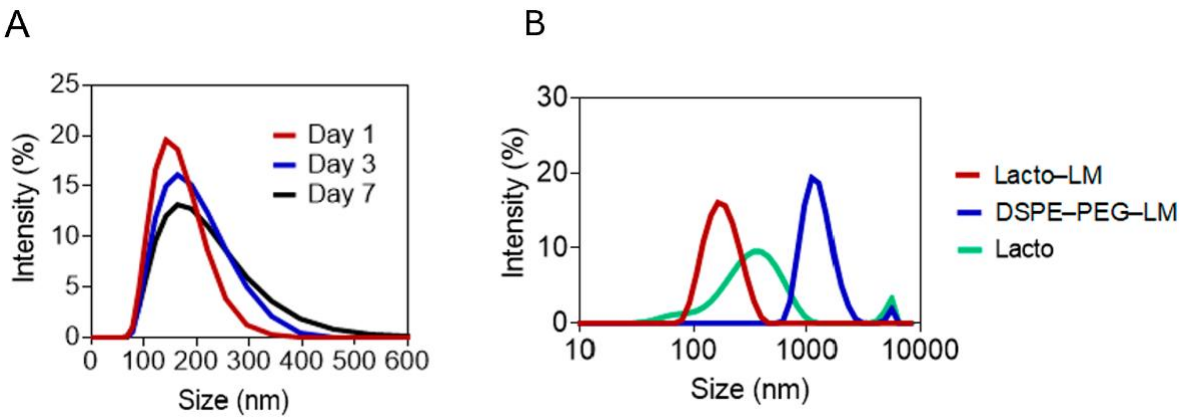

Figure 3.2 Dynamic light scattering (DLS) size distribution of Lacto–LM. A) Measurement of the average size of the nanocomposites on days 1, 3, and 7. B) DLS analysis of Lacto–LM, DSPE–PEG–LM, and Lacto.

Dynamic light scattering (DLS) analysis further substantiated the superior colloidal stability afforded by the Lacto-based surface modification. The Lacto–LM nanocomposites consistently exhibited a narrow hydrodynamic diameter distribution centered at approximately 160 nm and remained highly stable over an extended storage period of at least seven days (Figure 3.2A). The obtained DLS profiles revealed a low polydispersity index (PDI < 0.25) across multiple independent preparations, indicating favorable uniformity despite minor variations in surface morphology. In contrast, the DSPE–PEG–LM system displayed substantial polydispersity, with particle diameters exceeding 1,000 nm and pronounced aggregation after storage (Figure 3.3B). These results clearly demonstrate the superior stabilizing performance of the Lacto-based strategy. The enhanced colloidal stability of Lacto–LM is likely attributable to the unique interfacial interactions provided by bacterial components, which offer more robust and persistent stabilization than conventional polymeric surfactants, thereby effectively overcoming the intrinsic water immiscibility of pristine LM materials.

Transmission electron microscopy (TEM) analysis provided direct morphological

evidence of the successful formation of the Lacto–LM nanocomposites. The TEM micrographs clearly revealed a distinct bacterial component layer surrounding the LM cores, confirming the construction of a core–shell nanostructure (Figure 3.3). Quantitative evaluation of more than 200 particles demonstrated an average diameter of 136 ± 23 nm, with acceptable batch-to-batch reproducibility for this biohybrid nanocomposites. The uniform coating morphology consistently observed in Lacto–LM samples highlight the effectiveness and reliability of the sonication-based synthesis approach.

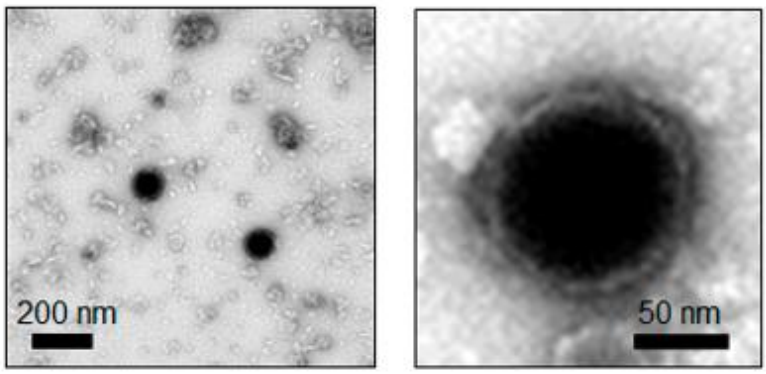

Figure 3.3 Transmission electron microscopy (TEM) images of Lacto–LM at low- (left) and high (right)-magnification.

However, DSPE–PEG–LM samples exhibited pronounced aggregation even under TEM grid conditions, whereas pristine LM displayed irregular morphology without discernible coating layers (Figure 3.4). Collectively, these findings corroborate the necessity and efficacy of the Lacto-based modification strategy in achieving stable biofunctional LM nanostructures.

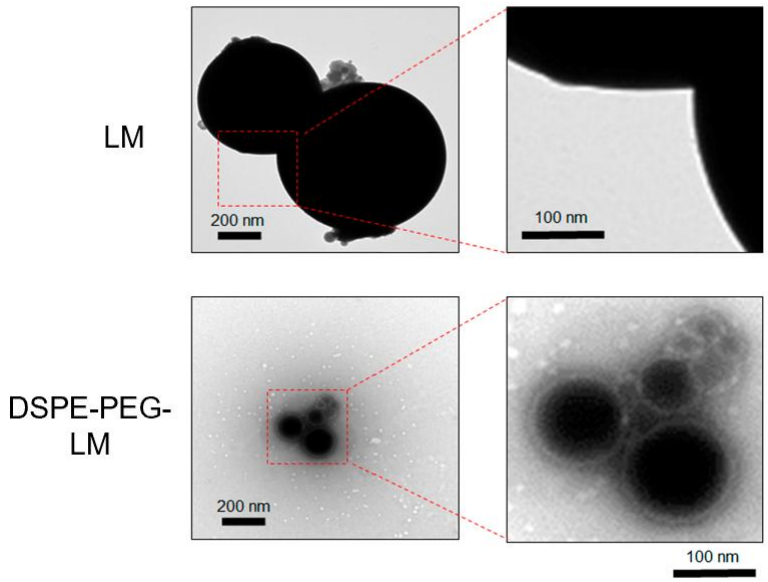

Figure 3.4 TEM images of pristine LM and DSPE–PEG–LM at low (left) and high (right) magnifications.

Ultraviolet–visible–near-infrared (UV–vis–NIR) spectroscopic analysis provided complementary evidence supporting the successful synthesis of Lacto–LM nanocomposites while preserving their characteristic optical properties. The absorption spectra of Lacto–LM dispersions in aqueous solution exhibited distinct absorbance in the therapeutically relevant NIR window (700–1,000 nm), consistent with the intrinsic optical response of the LM core (Figure 3.5). Notably, the appearance of characteristic Lacto-derived absorption peaks at approximately 220 and 250 nm confirmed the successful incorporation of bacterial components into the nanocomposite framework. Taken together, these spectroscopic results, in combination with the morphological and colloidal stability data, provide comprehensive validation of the successful fabrication of Lacto–LM nanocomposites.

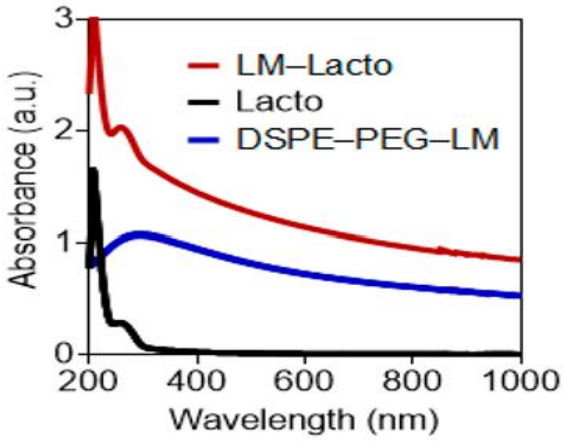

Figure 3.5 UV–vis–NIR absorbance spectra of PBS suspension of DSPE–PEG–LM, Lacto, and Lacto–LM. (LM concentration = 150 μg/mL and Lacto concentration = 7.65 × 108 CFU/mL).

The photothermal conversion capability of the Lacto–LM nanocomposites was then systematically investigated using precision thermocouple measurements under controlled 808 nm laser irradiation. To establish the dose–response relationship between photothermal heating efficiency and material concentration, temperature profiles were recorded for varying Lacto–LM concentrations under different laser power intensities: 0.3 W (approximately 15.3 mW mm^{-2}), 0.6 W (approximately 30.6 mW mm^{-2}), and 1.2 W (approximately 60.1 mW mm^{-2}) (Figure 3.6A–C). The results clearly demonstrated a power-dependent photothermal response. At the lowest laser power (0.3 W), only negligible temperature elevation was observed in Lacto–LM suspensions (LM concentration = 1 mg mL^{-1}) after 5 min of continuous irradiation, suggesting a threshold effect for efficient photothermal activation. Next, at 0.6 W, the same suspension reached temperatures of approximately 50 °C, approaching the threshold for hyperthermia-mediated cancer cell ablation. Most remarkably, when the laser power was further increased to 1.2 W, the suspension temperature rapidly exceeded 60 °C, demonstrating the exceptional photoexothermic performance of the Lacto–LM system. Together, this

substantial heating capacity and the observed concentration- and power-dependent response highlight the scalability and therapeutic adaptability of this nanosystem for diverse clinical applications.

Meanwhile, the photothermal conversion properties were validated by thermographic imaging of Lacto–LM solutions at different concentrations before and after 5 min of irradiation with a fiber-coupled 808 nm continuous-wave NIR laser (Figure 3.6D). These complementary thermal images corroborated the concentration-dependent heating behavior and provided spatial visualization of the temperature distribution, thereby reinforcing the potential of Lacto–LM nanocomposites for precise photothermal therapeutic applications.

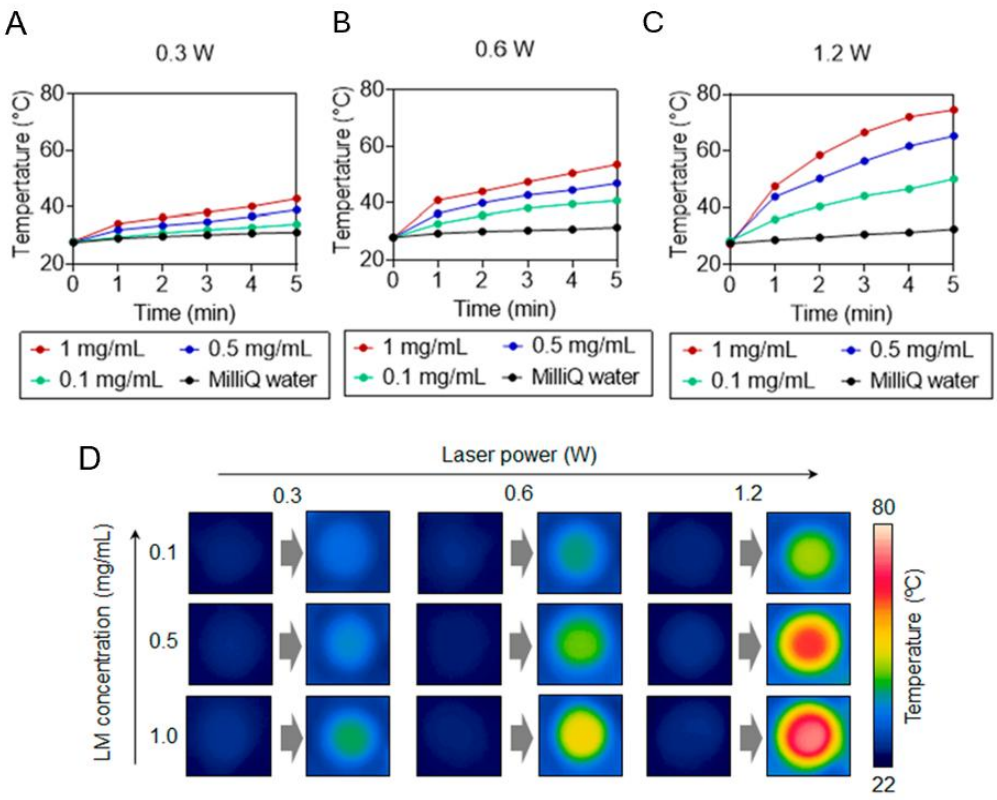

Figure 3.6 Photothermal activity of Lacto–LM nanocomposites. A-C) Photothermal heating curves, and D) corresponding thermographic images after 5 min of laser irradiation in Milli-Q water (control) and Lacto–LM at different LM concentrations by 808 nm laser irradiation at 0.3 W (ca. 15.3 mW/mm2), 0.6 W (ca. 30.6 mW/mm2), or 1.2 W (ca. 60.1 mW/mm2) power.

Considering the critical importance of material stability in preserving therapeutic efficacy while minimizing off-target thermal injury during photothermal therapy (PTT), we subsequently carried out detailed stability evaluations of the Lacto–LM nanocomposites. UV–vis–NIR spectroscopic analysis showed no detectable spectral alterations before or after 5 min of laser irradiation, thereby confirming robust optical stability under therapeutic conditions (Figure 3.7A). Such stability is essential for ensuring reproducible photothermal conversion efficiency throughout treatment.

In addition, thermal cycling experiments involving four consecutive laser on/off sequences further validated the resilience of the Lacto–LM system. Temperature monitoring revealed highly consistent heating and cooling curves with negligible fluctuations and only slight attenuation between cycles (Figure 3.7B). Taken together, these observations affirm the excellent photothermal durability of Lacto–LM nanocomposites under repeated irradiation, reinforcing their potential suitability for long-term therapeutic applications.

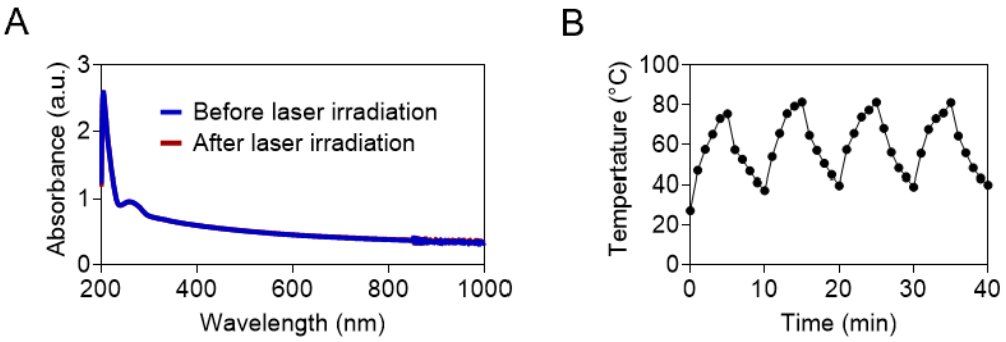

Figure 3.7 Photothermal stability of Lacto–LM nanocomposites. A)UV–vis–NIR absorbance spectra of Lacto–LM before and after laser irradiation for 5 min at 1.2 W (ca. 61.1 mW/mm^2). B) Stability testing of Lacto–LM under repetitive photothermal heating and natural cooling cycles by 808 nm laser irradiation at 1.2 W (ca. 61.1 mW/mm^2). LM concentration: 1 mg/mL in 0.5 mL PBS.

Quantitative evaluation demonstrated that the photothermal conversion efficiency of

Lacto–LM under 808 nm irradiation reached approximately 53%, which surpasses many previously reported photo exothermic nanomaterials, including metal-based agents, carbon nanostructures, and semiconducting polymer nanoparticles (Tables 8 and 9)[4-5, 19-23]. Such a high conversion efficiency, when considered together with the confirmed optical and thermal stability, positions Lacto–LM as a reliable and potent candidate for precision-targeted photothermal immunotherapy (PIT). Altogether, the systematic characterization results clearly establish that the Lacto-based surface modification strategy not only overcomes the intrinsic instability and poor aqueous compatibility of pristine LM systems but also introduces additional functional benefits derived from bacterial component incorporation. These combined advantages underscore the translational potential of the Lacto–LM nanocomposites for advanced therapeutic applications.

Table 8.The photothermal conversion efficiency of materials in previous reports.

Material	Photothermal conversion	Reference
Lacto–LM	53	This study
Gold nanorods	21	5
Gold nanoshells	13	5
Copper selenide	22	19
Carbon dots	31	4
Semiconducting polymer nanoparticles	37	20

Table 9.The photothermal conversion efficiency of LM nanoparticles in previous reports.

Material	Photothermal conversion efficiency (%)	Reference
Lacto–LM	53	This study
DSPE-PEG2000-amine–DC(8,9)PC–LM	52	23
Melanin–LM	37	7
SH-PEG-HS–CTAB–LM	33	22
Silica–LM	22	23

3.4.2 *In vitro* efficacy

The in vitro anticancer efficacy of laser-activated Lacto–LM nanocomposites was systematically investigated using normal human skin fibroblasts (TIG103) and murine colorectal cancer (Colon26) cells to establish both therapeutic potential and selectivity. To evaluate the intrinsic cytotoxicity and ensure the safety of the nanocomposite system, cells were first incubated with various concentrations of Lacto–LM for 24 h without NIR laser exposure (Figure 3.8). The results showed that Lacto–LM exhibited negligible cytotoxicity toward both TIG103 and Colon26 cells at all tested concentrations, thereby confirming the biocompatibility of the nanocomposite and demonstrating that its therapeutic efficacy is strictly dependent on photoactivation rather than intrinsic material toxicity.

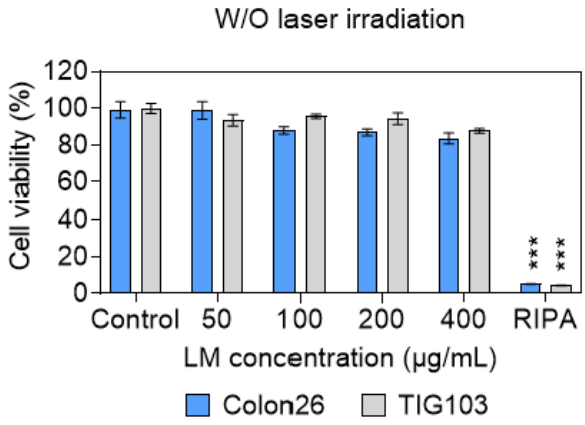

Figure 3.8 Viability of Colon26 and TIG103 cells after coculturing for 24 h with Lacto–LM at various LM concentrations or radioimmunoprecipitation assay (RIPA) buffer. Data are presented as mean ± SEM (n = 5; biologically independent tests). ***, $p < 0.001$, versus control without nanoparticles by Student's t-test.

In the following experiments, the photothermal cytotoxicity of laser-activated Lacto–LM nanocomposites was systematically investigated (Figure 3.9). Under irradiation with an 808 nm NIR laser at 0.6 W (≈30.6 mW/mm²), Lacto–LM induced significant cytotoxic effects in both TIG103 fibroblasts and Colon26 carcinoma cells, consistent with the robust photothermal conversion efficiency of the LM component. Of particular note, Colon26 cells displayed markedly higher sensitivity compared with normal TIG103 fibroblasts, thereby confirming favorable therapeutic selectivity. Such a discrepancy can be explained by intrinsic physiological distinctions between malignant and normal cells. Cancer cells typically exhibit elevated metabolic activity, diminished heat shock protein expression, and rapid proliferation, which collectively heighten their susceptibility to hyperthermia-induced protein denaturation and DNA damage. Conversely, normal fibroblasts preserve higher basal levels of heat shock proteins, enabling protein refolding, stabilization of macromolecular structures, and suppression of apoptosis under thermal stress[24-25]. Taken together, this inherent selectivity is

of critical significance, as it enhances therapeutic efficacy while minimizing collateral damage to healthy tissues, thereby strengthening the translational potential of the Lacto–LM system.

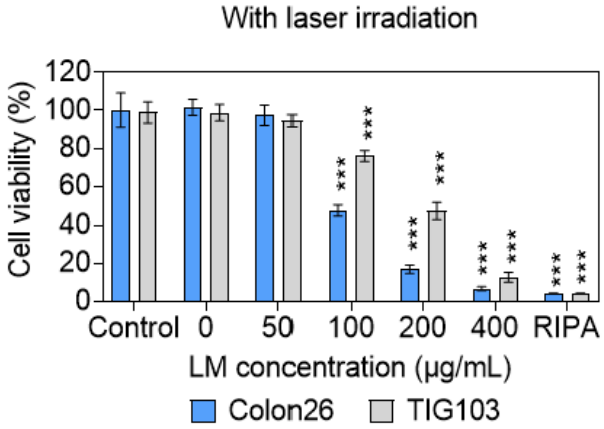

Figure 3.9 Cytotoxicity assay with Colon26 and TIG103 cells after Lacto–LM treatment at various LM concentrations for 24 h and laser irradiation. Data are presented as mean ± SEM (n = 5; biologically independent tests). ***, $p < 0.001$, versus control without nanoparticles by Student's t-test.

The real-time anticancer performance of NIR laser-activated Lacto–LM nanocomposites was then examined using an integrated optical microscopy system equipped with a single-beam laser setup. When exposed to 808 nm irradiation at 564 mW (~287 mW mm^{-2}), Colon26 cells underwent rapid disruption characterized by bubble generation, which was likely attributed to water vaporization induced by the intense photoexothermic reaction of LM (Figure 3.10). As a result, this immediate structural collapse clearly demonstrated the robust and acute photothermal effect of Lacto–LM. In contrast, control groups without nanocomposites displayed no detectable cell damage under identical laser conditions, thereby confirming that the cytotoxicity originated from the Lacto–LM system rather than laser irradiation alone. Taken together, these observations emphasize the superior photothermal conversion efficiency of Lacto–LM and provide compelling evidence for its potential as a precision therapeutic agent

for targeted cancer ablation.

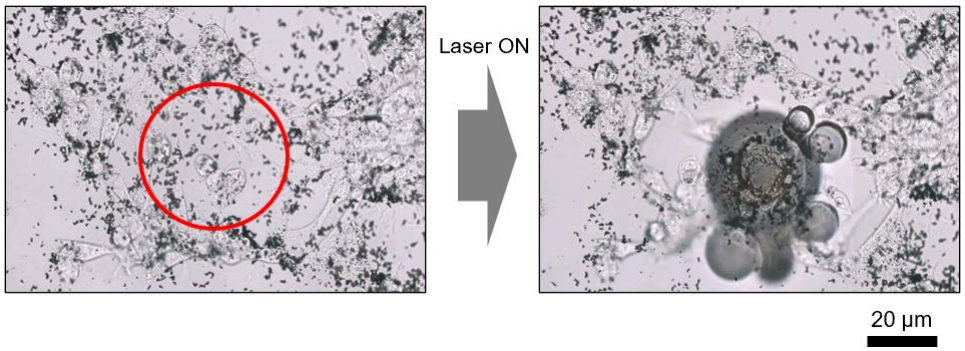

Figure 3.10 Direct microscopic observation of Colon26 cell damage caused by 808-nm NIR laser-induced Lacto–LM (564 mW, ~287 mW/mm2). Red circle shows laser irradiation position and area.

PI (Propidium Iodide) is a nucleic acid-binding dye that intercalates into DNA and RNA but cannot traverse intact cell membranes. Consequently, it selectively stains cells with compromised membrane integrity, such as dead or late-apoptotic cells. To further evaluate cell viability and elucidate the underlying death mechanisms, PI staining was performed under different laser power densities (72, 144, and 287 mW/mm²), in combination with real-time live-cell imaging (Figure 3.11). Following irradiation at 144 and 287 mW/mm², extensive PI-positive staining (red fluorescence) was observed, indicative of widespread cell death. This potent result was further supported by quantitative fluorescence intensity analysis, which revealed a significantly higher PI signal in the Lacto–LM group compared with the PBS control group before and after laser irradiation (Figure 3.12). This integrated biochemical and morphological assessment clearly confirmed that Lacto–LM nanocomposite–mediated photothermal therapy predominantly induces cancer cell death.

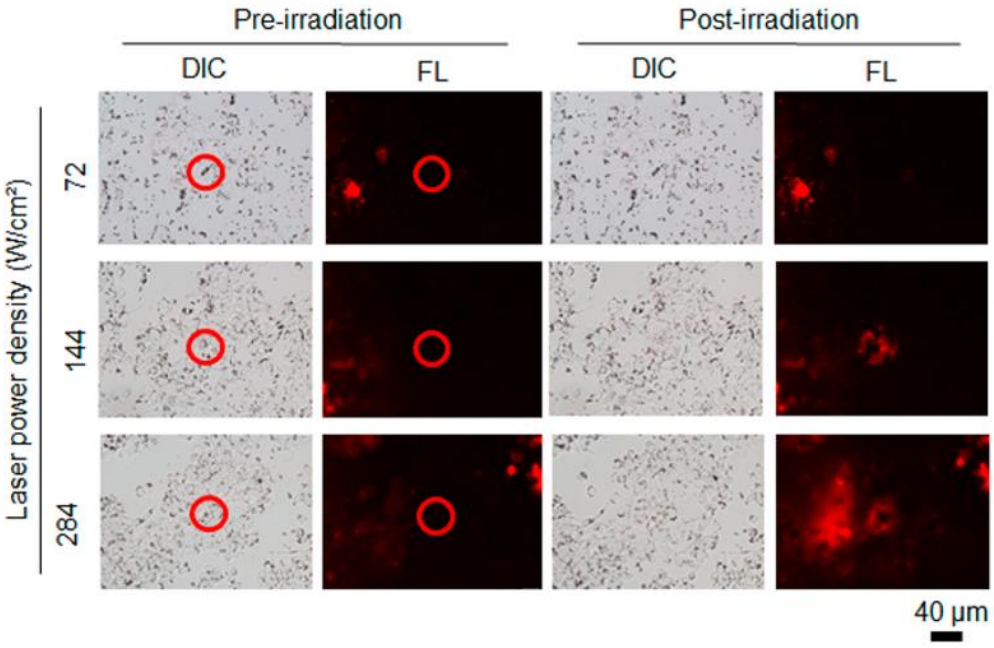

Figure 3.11 Effect of laser power density on cell death.Representative DIC and PI fluorescence images of Colon 26 cells irradiated with an 808 nm laser at 72, 144, or 284 W/cm² for 3 s after treatment with Lacto–LM (375 μg/mL) for 5 h. PI fluorescence denotes dead cells within the laser-irradiated region. Red circles indicate the laser irradiation spot.

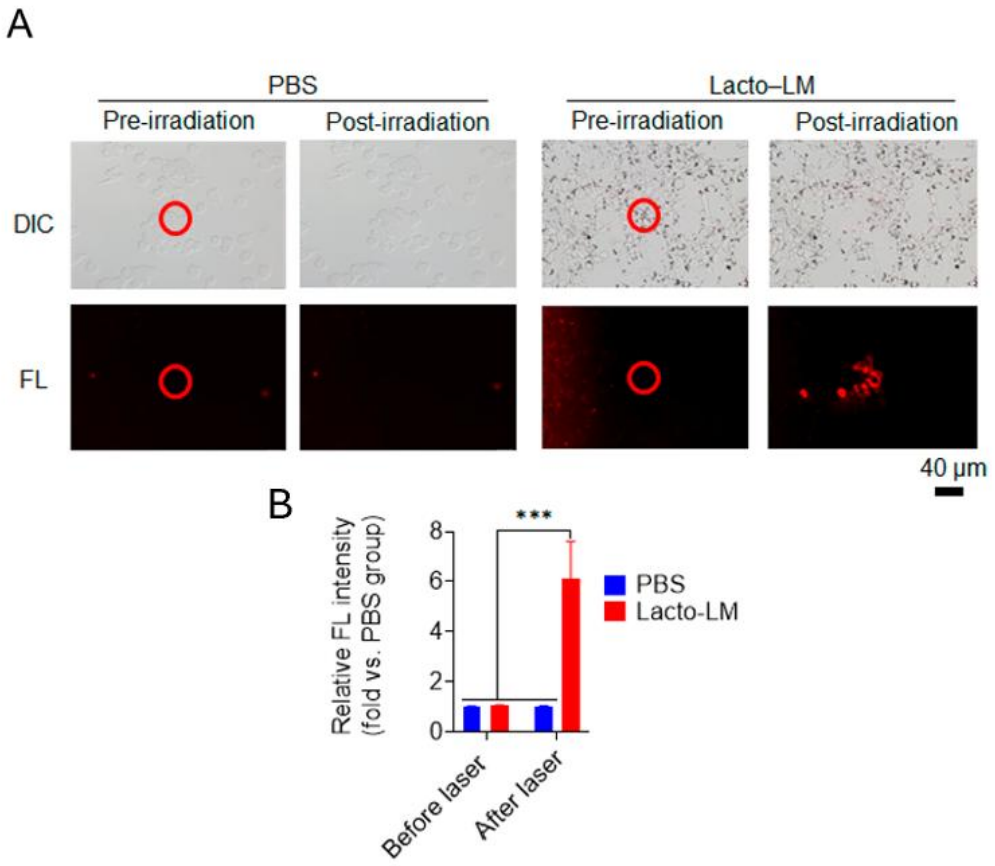

Figure 3.12 Laser-induced cell death in Colon 26 cells. A) Representative differential interference contrast (DIC) and propidium iodide (PI) fluorescence images of Colon 26 cells treated with PBS or Lacto–LM (75 μg/mL) before and after 808 nm laser irradiation (144 W/cm², 3 s). Red circles indicate the laser irradiation spot B) Quantitative analysis of relative fluorescence intensity. Data are presented as mean ± SD. ***p < 0.001 (Lacto–LM vs. other groups, N = 3).

Given that cellular internalization of nanomedicines is essential for achieving therapeutic efficacy[26-27], the uptake kinetics and intracellular distribution of Lacto–LM nanocomposites in Colon26 cells were systematically investigated using fluorescence (FL) spectroscopy and microscopy. For visualization, Lacto–LM nanocomposites encapsulating the NIR fluorescent dye indocyanine green (ICG) were prepared via a simple sonication process (ICG–Lacto–LM). In this nanoformulation, ICG molecules were sequestered within the bacterial components through ionic and hydrophobic interactions (Figure 3.13A). FL spectroscopic measurements demonstrated that ICG–Lacto–LM exhibited strong NIR fluorescence emission upon excitation, confirming successful incorporation and stable retention of the fluorescent probe (Figure 3.13B).

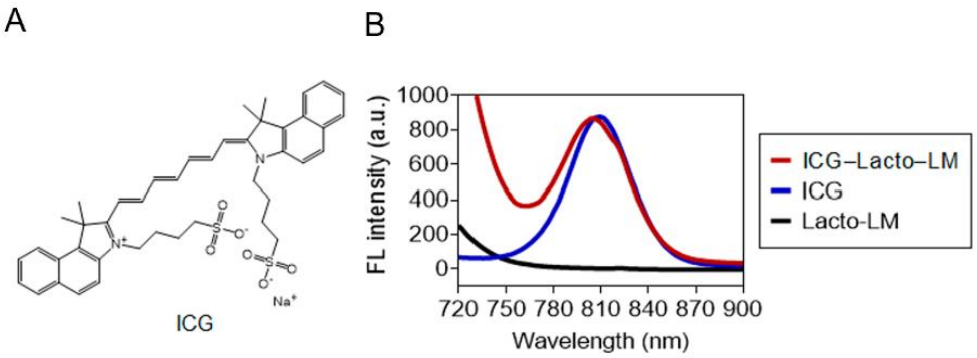

Figure 3.13 Fluorescence (FL) spectra of ICG–Lacto–LM. A) Chemical structure of ICG molecule. B) Fluorescence (FL) spectra of ICG–Lacto–LM (LM concentration = 300 μg/mL and ICG concentration = 12.5 μg/mL) at 750 nm excitation wavelength.

Following 24 h incubation with ICG–Lacto–LM, Colon26 cells exhibited extensive intracellular fluorescence, manifested as characteristic black or pink puncta within the cellular

structures, thereby confirming successful nanocomposite internalization (Figure 3.14A). In contrast, cells treated with PBS displayed no detectable fluorescence, validating the specificity of the observed signal. Three-dimensional FL microscopy further demonstrated a uniform cytosolic distribution of ICG–Lacto–LM (Figure 3.14B), indicating efficient cellular uptake and favorable intracellular localization, which collectively support its potential for subsequent therapeutic applications.

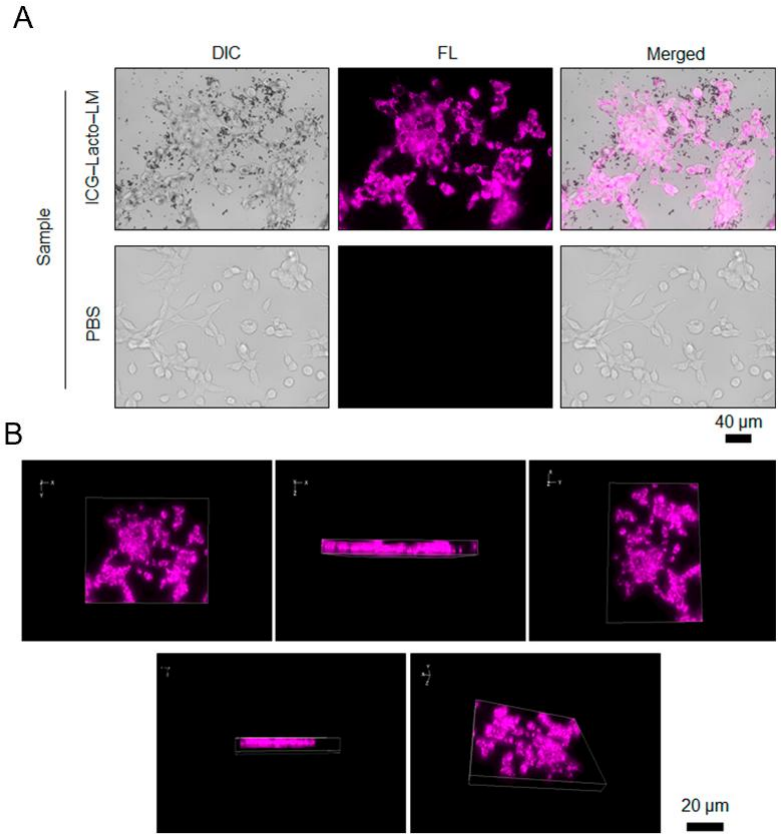

Figure 3.14 Intracellular distribution of indocyanine green (ICG) –Lacto–LM nanocomposites. A) Near-infrared (NIR) FL bioimaging of Colon26 cells after coculturing with ICG–Lacto–LM or PBS for 24 h. Pink and black particles represent Lacto–LM. B) Three-dimensional (3D) images of Colon26 cells after coculturing with ICG–Lacto–LM.

Moreover, to investigate the behavior of the Lacto–LM formulations due to fabrication of bacterial component, the cellular uptake of free ICG, ICG–LM, and ICG–Lacto–LM was systematically assessed at different incubation times (Figure 3.15). At the early time point of

0.5 h, slightly higher fluorescence was observed in the free ICG and ICG–LM groups, likely attributable to the rapid diffusion of ICG molecules across the cell membrane and into the cytosol. In contrast, ICG–Lacto–LM exhibited a more controlled release of ICG, owing to the presence of the bacterial coating. Quantitative analysis further demonstrated that ICG–Lacto–LM achieved significantly greater uptake efficiency compared with both free ICG and ICG–LM after 0.5 h. At later time points of 6 and 12 h, the intracellular fluorescence intensity of ICG–Lacto–LM remained markedly higher than that of the other two formulations ($p < 0.001$). Collectively, these results indicate that Lacto–LM nanocomposites possess superior biocompatibility and cellular penetration properties, which are essential prerequisites for efficient intracellular therapeutic delivery.

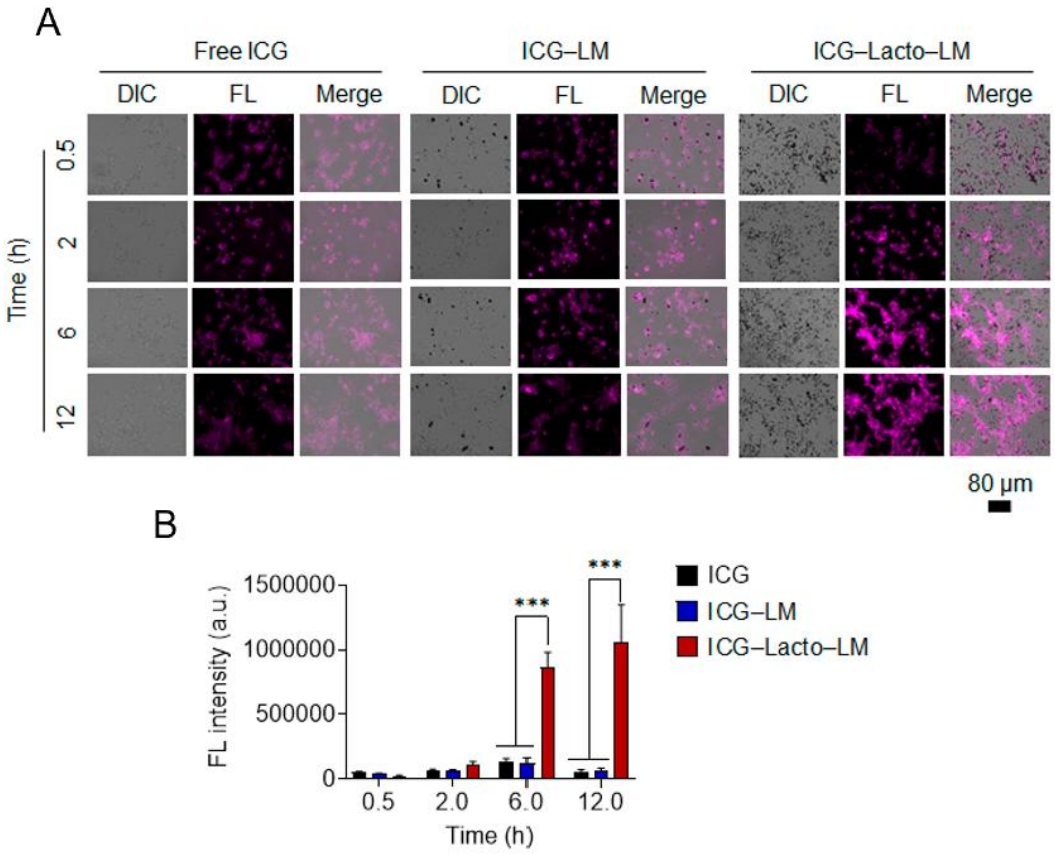

Figure 3.15 Enhanced cellular uptake of ICG–Lacto–LM nanocomposites by Colon26 cells. A)

Representative fluorescence microscopy images showing ICG uptake at 6 and 12 hours for free ICG, ICG–LM, and ICG–Lacto–LM nanocomposites. B) Quantitative analysis of intracellular ICG fluorescence intensity at 0.5, 2, 6, and 12 hours. Data represent mean ± SD (n = 3). ***$p < 0.001$ compared to free ICG and ICG–LM groups.

To investigate the in vitro immune-activating capacity of Lacto–LM nanocomplexes, we first evaluated their ability to polarize macrophages toward an M1-like, antigen-presenting phenotype. Activation of antigen-presenting cells up-regulates the costimulatory ligands CD80 (B7-1) and CD86 (B7-2), which engage CD28 to deliver the second signal required for effective T-cell priming; accordingly, CD80/CD86 are widely used readouts of APC activation in tumor-associated myeloid cells[28-30]. RAW 264.7 macrophages were exposed to Lacto–LM for 24 h, after which surface CD80 and CD86 were imaged and quantified by fluorescence microscopy. In contrast to PBS and Lacto controls, Lacto–LM markedly increased fluorescence intensity of $CD80^+$ (green) and $CD86^+$ (red) cells (Figure 3.16), indicating acquisition of a co-stimulatory, M1-skewed phenotype compatible with efficient T

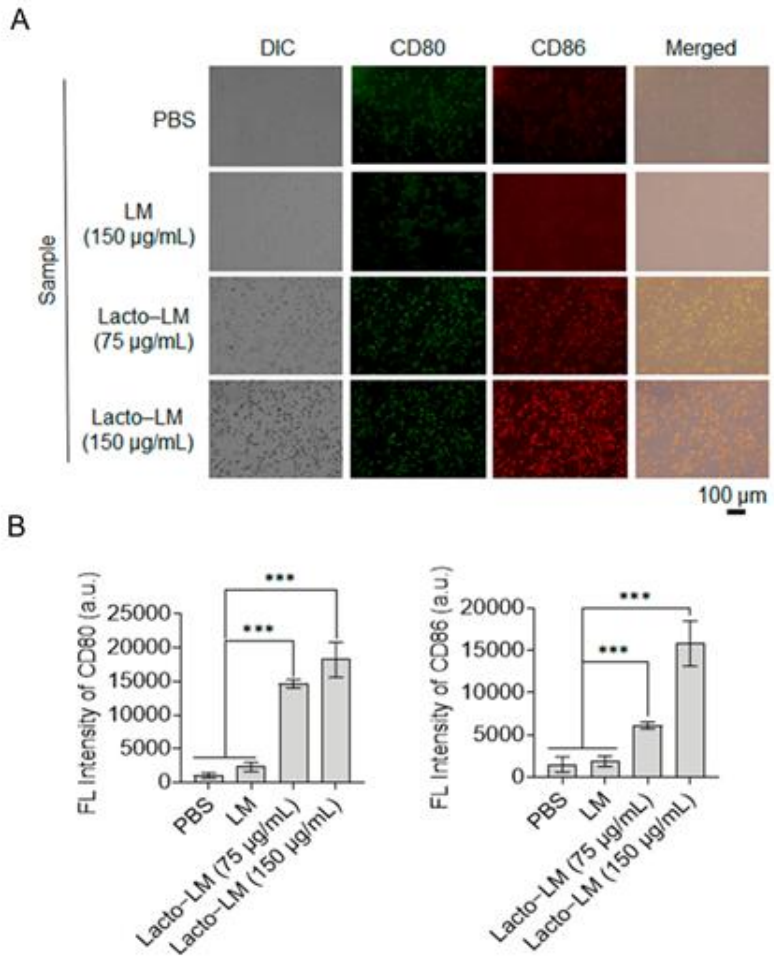

Figure 3.16 Expression of CD80 and CD86 in RAW 264.7 macrophages treated with PBS, LM (150 μg/mL), or Lacto–LM (75 or 150 μg/mL) for 24 h and stained with anti-CD80–FITC and anti-CD86–APC antibodies. Differential interference contrast (DIC) and merged fluorescence images are shown. B) Quantification of mean fluorescence intensities of CD80 and CD86. Data are presented as mean ± SD (N = 5). ***$p < 0.001$.

We next profiled pro-inflammatory cytokine secretion by RAW 264.7 macrophages. Cell-free supernatants collected at predefined time points (4, 8, 12, and 24 h) after treatment were analyzed by ELISA. Lacto–LM, but not PBS or Lacto alone, elicited significant increases in TNF-α and IL-6 (Figure 3.17). These cytokines are canonical outputs of M1-type activation and support T-cell priming and antitumor effector functions within the tumor microenvironment, reinforcing that Lacto–LM effectively licenses macrophages for immune-mediated antitumor responses.

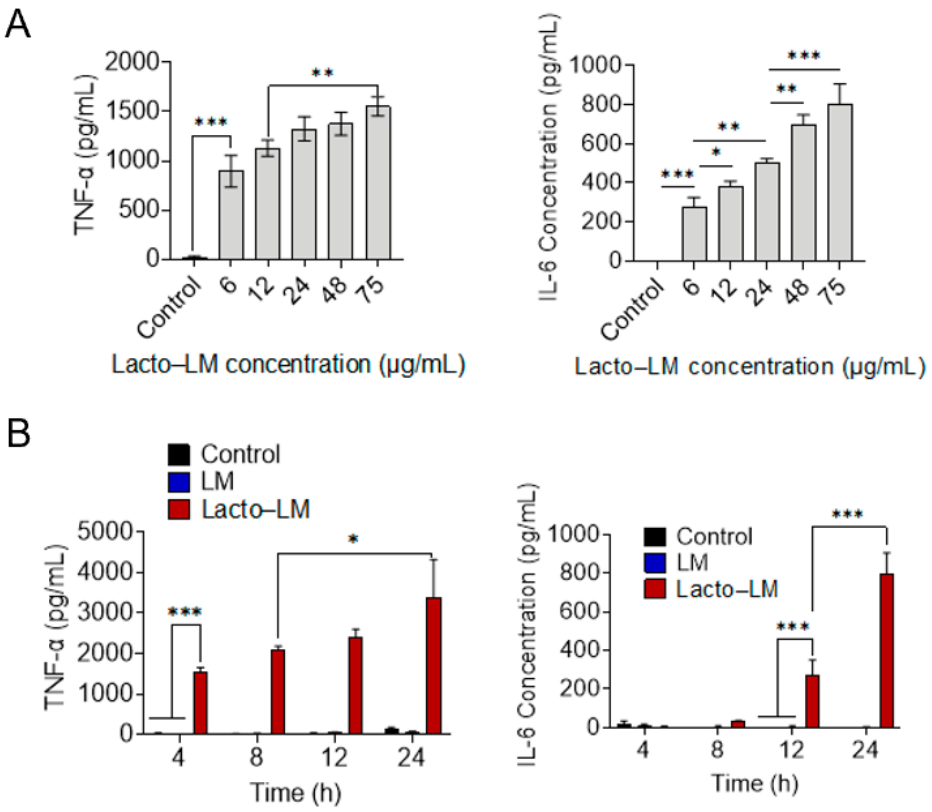

Figure 3.17 Immunostimulatory effects of Lacto–LM nanocomposites on RAW 264.7 macrophages assessed by cytokine secretion profiling. A) Concentration-dependent cytokine response: RAW 264.7 macrophages were treated with increasing concentrations of Lacto–LM nanocomposites (6, 12, 24, 48, and 75 μg/mL) and analyzed for TNF-α secretion at 4 hours and IL-6 secretion at 24 hours post-treatment. B) Time-course analysis of cytokine secretion: Temporal profiles of TNF-α and IL-6 release from RAW 264.7 macrophages following treatment with Lacto–LM nanocomposites (75 μg/mL) over 4, 8, 12, and 24 hours. Cytokine concentrations were quantified using enzyme-linked immunosorbent assay (ELISA). Data represents standard deviation from three independent experiments (n = 3). Statistical significance was determined by Student's two-sided t-test or one-way ANOVA. *$p < 0.05$, **$p < 0.01$, ***$p < 0.001$ compared to untreated control group. The results demonstrate dose- and time-dependent immune activation by Lacto-LM nanocomposites, confirming their immunostimulatory properties mediated by bacterial components.

3.4.3 *In vivo* efficacy

The clinical translation of nanoparticle-based therapeutics faces significant challenges, as most intravenously administered nanoparticles are rapidly cleared by the reticuloendothelial system, with only a minimal fraction reaching target tumor tissues, thereby severely compromising therapeutic efficacy. To address this limitation, we employed a biomimetic

strategy to modify LM with bacterial components, hypothesizing that Lacto–LM nanocomposites would achieve enhanced immune activation and homologous targeting capabilities. Consequently, we conducted comprehensive biodistribution analysis to evaluate the tumor-targeting potential of our nanocomposite system.

Using NIR fluorescent ICG–Lacto–LM in a Colon26-bearing syngeneic mouse model, we monitored biodistribution kinetics using an *in vivo* bioimaging system. The tumor-targeting behavior of ICG–Lacto–LM was evaluated over time following intravenous (i.v.) injection through the tail vein, with accumulation attributed to the enhanced permeability and retention (EPR) effect. Comparative analysis revealed that ICG–Lacto–LM exhibited significantly superior tumor accumulation compared to ICG–DSPE–PEG–LM, with the conventional surfactant-modified system showing markedly weakened fluorescence signals 24 h after i.v. administration (Figures 3.18). This enhanced targeting efficiency can be attributed to the multifaceted advantages of the Lacto nanocoating, including superior water dispersibility, prolonged circulation time, and enhanced tumor penetration capabilities. The control group (PBS injection) exhibited no detectable fluorescence throughout the body, confirming the specificity of the observed signals.

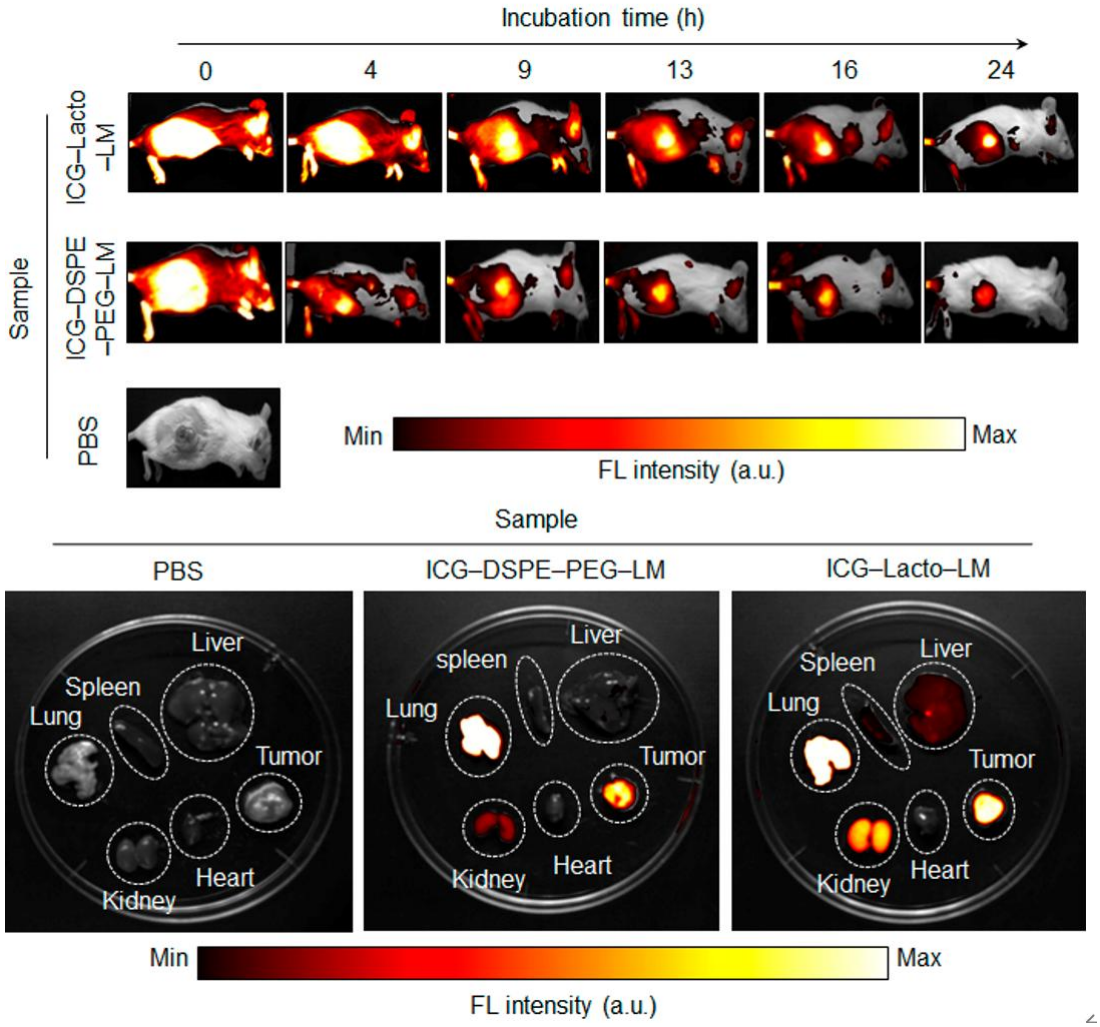

Figure 3.18 In vivo tumor targeting effect of ICG–Lacto–LM nanocomposites. Near-infrared (NIR) fluorescence bioimaging of whole body, extracted tumors, and vital organs from Colon26 tumor-bearing mice was performed following intravenous injection of ICG–Lacto–LM, PBS or ICG–DSPE–PEG–LM through the tail vein. ICG and LM concentrations were 22.22 mg/kg and 3 mg/kg, respectively.

Although weak fluorescence signals were detected in the lungs, the tumor site displayed markedly stronger fluorescence intensity following ICG–Lacto–LM administration. The fluorescence signals observed in the lungs, kidneys, and liver likely resulted from reticuloendothelial, renal, and hepatic clearance mechanisms, which represent the primary elimination pathways for these LM nanoparticles. These findings collectively demonstrate that

Lacto–LM possesses exceptional tumor selectivity and prolonged tumor site retention following single administration, suggesting that the design of tumor-localizing LM nanoparticles represents an excellent strategy for targeting and penetrating diverse cell subpopulations within the complex tumor microenvironment.

We subsequently evaluated the *in vivo* photothermal performance of the nanosystem after LM nanocomposites reached tumor tissues. Targeted Colon26 tumors in mice were irradiated with an 808-nm laser at 600 mW (approximately 30.6 mW/mm²) 24 h after single i.v. administration of each formulation. During irradiation, body surface temperature was continuously monitored using thermographic imaging (Figure 3.19A). The tumor surface temperature in mice injected with Lacto–LM increased dramatically within 5 min of NIR laser irradiation, reaching a peak of approximately 58 °C (Figure 3.19B). In contrast, the DSPE–PEG–LM solution produced only modest temperature elevation, from 32 °C to approximately 39 °C. The substantially more pronounced temperature elevation observed with laser-irradiated Lacto–LM compared to DSPE–PEG–LM indicates that Lacto–LMs preferentially accumulated in solid tumors and effectively heated deeper tumor tissues. This enhancement can be attributed to both the EPR effect and the specific intratumor binding of Lacto components to immune and cancer cells. Similarly, control groups (PBS and lactose alone) displayed only slight tumor surface temperature increases following laser irradiation, likely due to partial conversion of light energy to heat by skin, blood, and surrounding tissues. This comprehensive evaluation confirmed both the precise tumor targeting and exceptional photothermal properties of LM nanocomposites, underscoring their potential as a promising therapeutic strategy for cancer treatment.

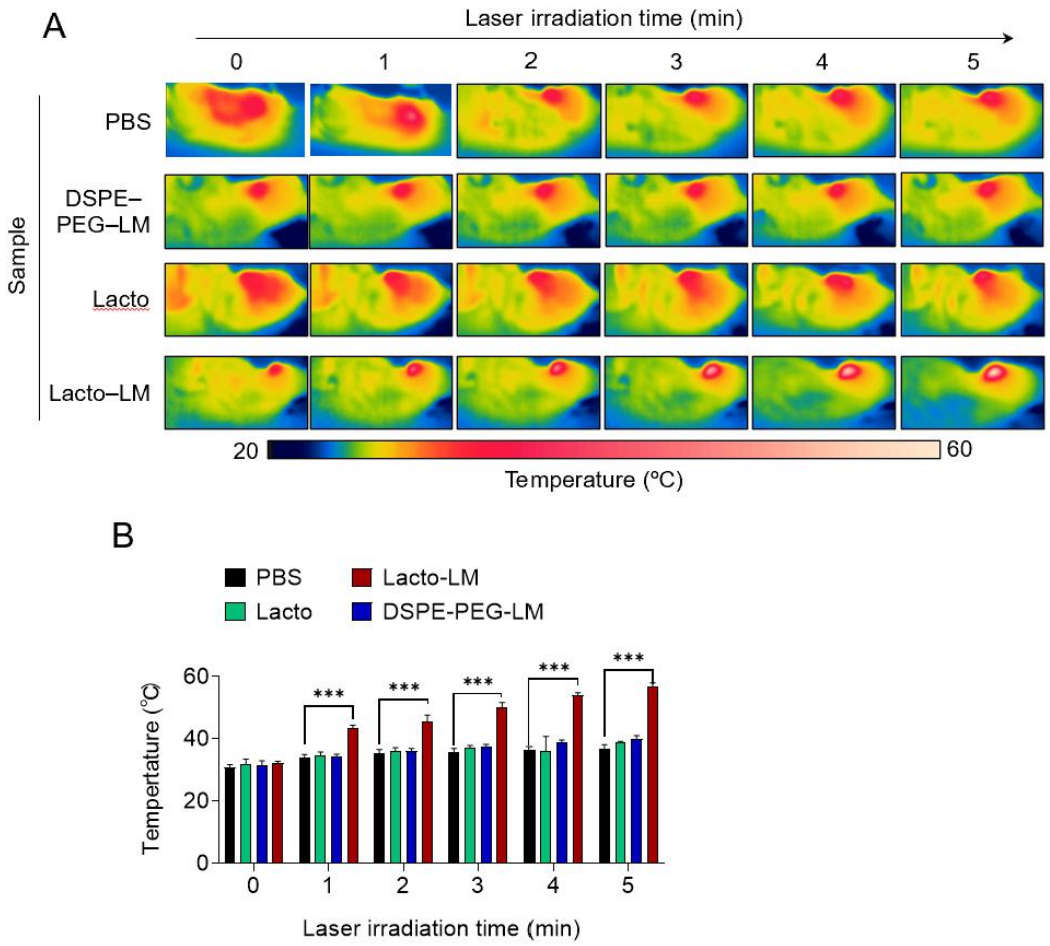

Figure 3.19 In vivo photothermal conversion of laser-induced Lacto–LM nanocomposites. A) Thermographic measurement of the tumor on the mouse body surface following 808-nm laser irradiation. Laser power was 0.6 W (ca. 30.6 mW/mm^2) and irradiation time was 5 min. B) Surface temperature of solid tumor in Colon26-bearing mice on day 1 after injection with LM–Lacto followed by 808 nm laser irradiation for 5 min (laser power = 0.6 W [≈30.6 mW/mm^2]). Data are expressed as mean ± standard error of the mean (SEM); n = 5 independent experiments. Statistical significance was calculated in comparison with the PBS group. ***p < 0.001, by Student's t-test.

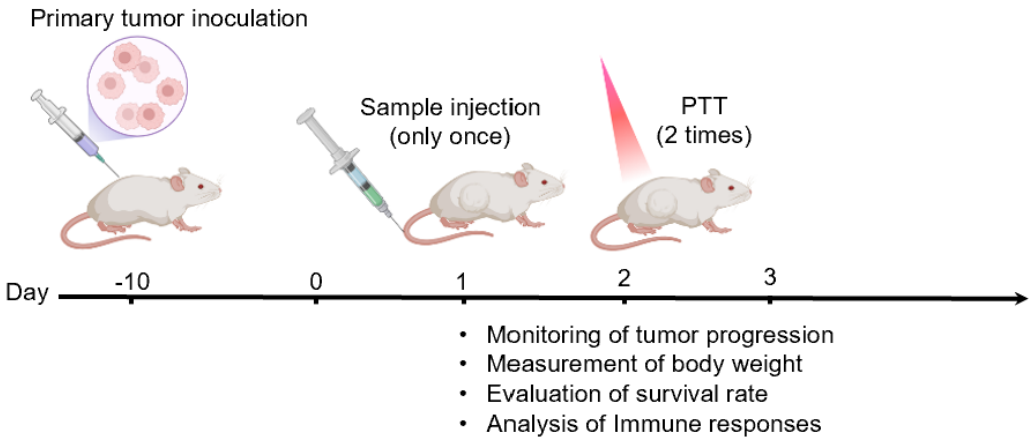

Figure 3.20 Time course of establishment and treatment of BALB/c mice bearing Colon26 tumors. After tumor establishment, mice were irradiated following intravenous (i.v.) injection with a single dose of Lacto–LM.

The in vivo antitumor efficacy of Lacto–LM was systematically evaluated in Colon26 tumor-bearing mice according to the experimental scheme shown in Figure 3.20. In the absence of laser irradiation, Compared with the PBS group, Lacto alone exhibited measurable antitumor activity, primarily attributable to its immune-activating capacity (Figure 3.21). Similarly, Lacto–LM induced pronounced tumor suppression in Colon26-bearing mice, which can be ascribed to the synergistic effects of enhanced tumor targeting and immune stimulation. In contrast, the DSPE–PEG–LM formulation showed no therapeutic efficacy in the absence of laser irradiation, thereby confirming its lack of intrinsic anticancer properties.

The laser-induced anticancer therapeutic efficacy was further evaluated using the Colon26 tumor-bearing mouse model. The Lacto–LM + laser group demonstrated significant tumor volume reduction compared to both DSPE–PEG–LM + laser and PBS + laser groups (Figure 3.21), highlighting the potent anticancer effect of Lacto–LM-mediated PIT. Remarkably, in the Lacto–LM + laser group, irradiated tumors achieved complete regression within three days following a single injection and two laser treatments, achieving a 100% complete response rate

at the 20-day follow-up. This exceptional therapeutic outcome can be attributed to the synergistic combination of exceptional photothermal properties of LM and the potent immunostimulatory effects of Lacto components. These findings suggest that laser irradiation enhances immune activation through heat energy generated by natural photothermal conversion in biological tissues. Furthermore, the Lacto + laser group exhibited superior antitumor efficacy compared to the PBS + laser group, likely due to the immunostimulatory effects of Lacto, further supporting its role in promoting effective immune responses against tumors. Collectively, these results demonstrate that Lacto–LM + laser treatment elicits robust and durable antitumor efficacy through the combined contributions of LM-mediated photothermal heating and Lacto-induced immune activation.

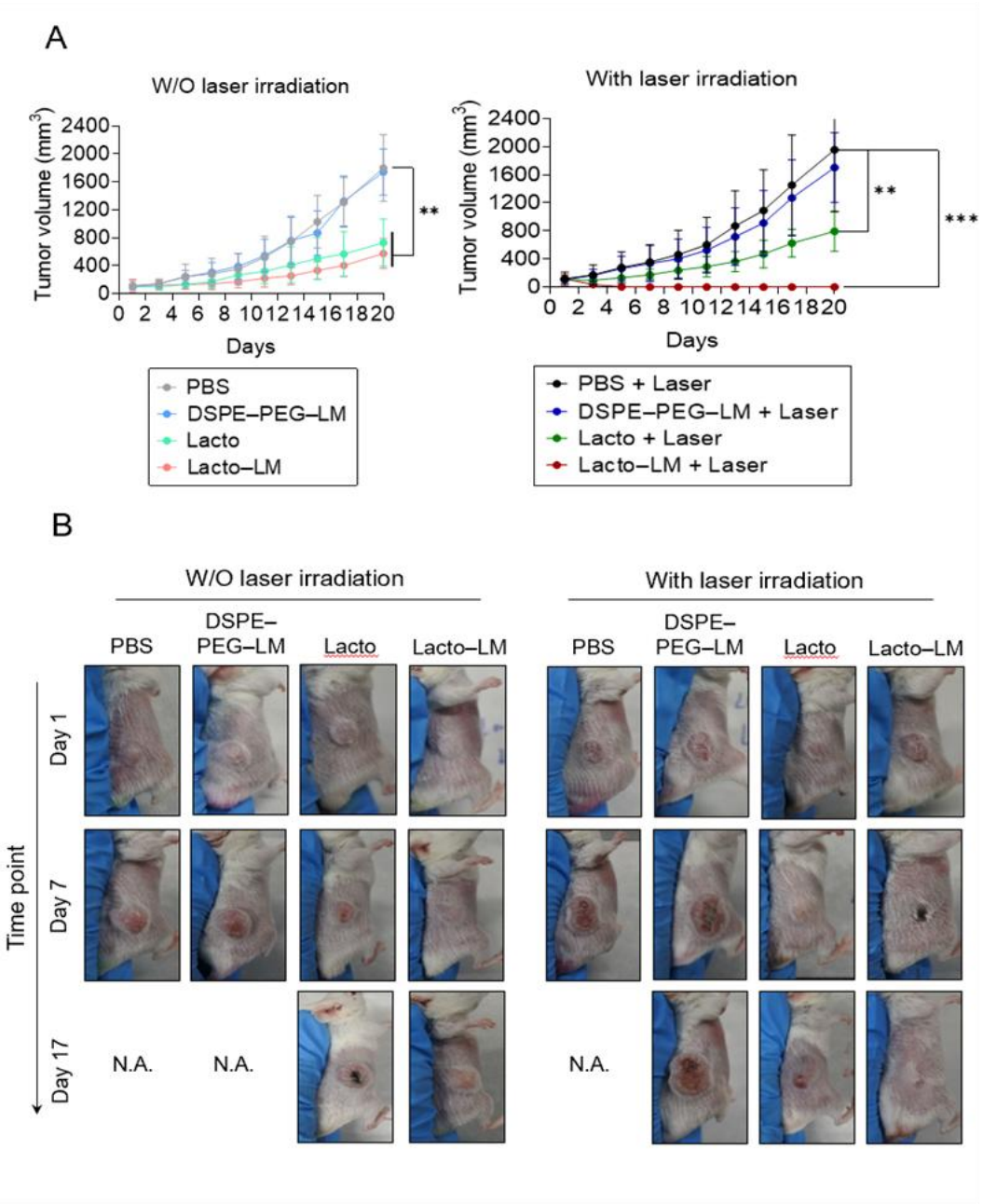

Figure 3.21 Enhanced in vivo antitumor effect of Lacto–LM-mediated PIT. A) In vivo anticancer efficacy of various samples with and without laser irradiation. PBS or dispersion of DSPE–PEG–LM, Lacto and Lacto–LM were i.v. injected into mice. After 24 h, the tumors were treated with 808 nm laser irradiation (laser power = 0.6 W [ca. 30.6 mW/mm2]; irradiation time = 5 min/day [total two times irradiation]). Data are expressed as mean ± standard error of the mean (SEM) (n = 5 biologically independent tests). **p < 0.01, ***p < 0.001, by Student's t-test. The black arrow indicates the time point of sample administration. B) Images of mice after each treatment.

Body weights of mice in all treatment groups, with and without laser irradiation, remained stable throughout the experimental period, indicating the absence of significant adverse effects (Figure 3.22A).

Moreover, laser-induced Lacto–LM treatment significantly prolonged survival, consistent with its potent anticancer efficacy (Figure 3.22B). The Lacto + laser, Lacto without laser, and Lacto–LM without laser groups also displayed moderate survival benefits, which can be ascribed to the intrinsic immunological activity of the Lacto component. In contrast, the PBS control and DSPE–PEG–LM groups showed no therapeutic advantage in extending survival. Overall, these results corroborate the robust anticancer potential of the Lacto–LM formulation.

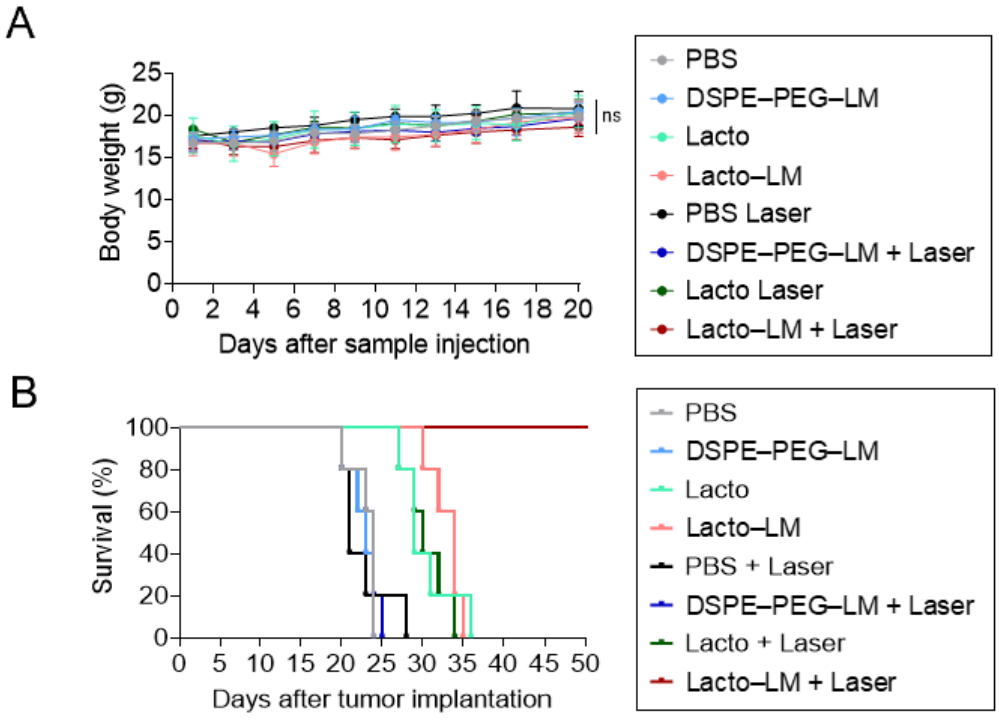

Figure 3.22 In vivo antitumor efficacy of laser-induced Lacto–LM nanocomposites. A) Average mouse body weight after each treatment. B) Kaplan–Meier survival curves of Colon26 tumor-bearing mice (n = 5 biologically independent mice) after treatment for 40 d. Statistical significance was calculated in comparison with the PBS group. The Lacto–LM + laser group showed a 100% survival rate for at least 50 d.

We further conducted blood biochemical analyses in mice to evaluate the safety profile of the Lacto–LM nanocomposite. The results revealed no significant alterations in blood cell counts or biochemical parameters after 7 days of intravenous administration of either Lacto–LM or PBS (Table 10). These findings demonstrate the favorable biocompatibility and safety of the Lacto–LM nanocomposite system.

Table 10. Complete blood counts (CBCs) and biochemical parameters of the BALB/c mice injected with PBS or Lacto–LM dispersion after 7 days.

Measured value	Entry	Unit	PBS (n = 6)	Lacto–LM (n = 6)	*p* value
CBC	WBC	$\times 10^2$ /μL	75.5 ± 18.77	75.5±18.77	> 0.05
	RBC	$\times 10^4$ /μL	875.5 ± 47.18	875.5±47.18	> 0.05
	HGB	g/dL	15.53 ± 0.54	15.53±0.54	> 0.05
	HCT	%	45.42 ± 2	45.42±2	> 0.05
	MCV	fL	51.88 ± 0.86	51.88±0.86	> 0.05
	MCH	pg	17.75 ± 0.41	17.75±0.41	> 0.05
	MCHC	g/dL	34.22 ± 0.62	34.22±0.62	> 0.05
	PLT	$\times 10^4$ /μL	73.72 ± 13.24	73.72±13.24	> 0.05
Biochemical parameters	TP	g/dL	4.3±0.15	4.31±0.09	> 0.05
	ALB	g/dL	3.02±0.08	3.09±0.07	> 0.05
	BUN	mg/dL	19.43±2.83	23.37±3.89	> 0.05
	CRE	mg/dL	0.09±0.01	0.1±0.01	> 0.05

Measured value	Entry	Unit	PBS (n = 6)	Lacto–LM (n = 6)	*p* value
	Na	mEq/L	146.5±2.59	145.43±1.72	> 0.05
	K	mEq/L	22.58±0.87	23.14±2.91	> 0.05
	Cl	mEq/L	103.67±0.82	105±1.91	> 0.05
	AST	IU/L	45.5±3.56	44±6.27	> 0.05
	ALT	IU/L	22.33±3.67	21.71±4.68	> 0.05
	LDH	IU/L	145.17±85.78	150.86±77.99	> 0.05
	AMY	IU/L	2033±171.39	2085.43±144.19	> 0.05
	CK	IU/L	55.33±9.77	50.29±9.34	> 0.05

Data are represented as means ± standard errors of the mean (SEM); n = 6 biologically independent mice. Statistical analyses comprise the one-way ANOVA).

Abbreviations: ALB, albumin; ALT, alanine transaminase; AMY, amylase; AST, aspartate aminotransferase; BUN, blood urea nitrogen; Cl, chlorine; CK, creatine kinase; CRE, creatinine; HCT, hematocrit; HGB, hemoglobin; K, potassium; LDH, lactate dehydrogenase; MCH, mean corpuscular hemoglobin; MCHC, mean corpuscular hemoglobin concentration; MCV, mean corpuscular volume; Na, sodium; PLT, platelet; RBC, red blood cell; TP, total protein; WBC, white blood cell.

Moreover, H&E staining of major organs, including the heart, liver, lungs, kidneys, and spleen, revealed no evidence of histological abnormalities in the Lacto–LM–treated group (Figure 3.23).

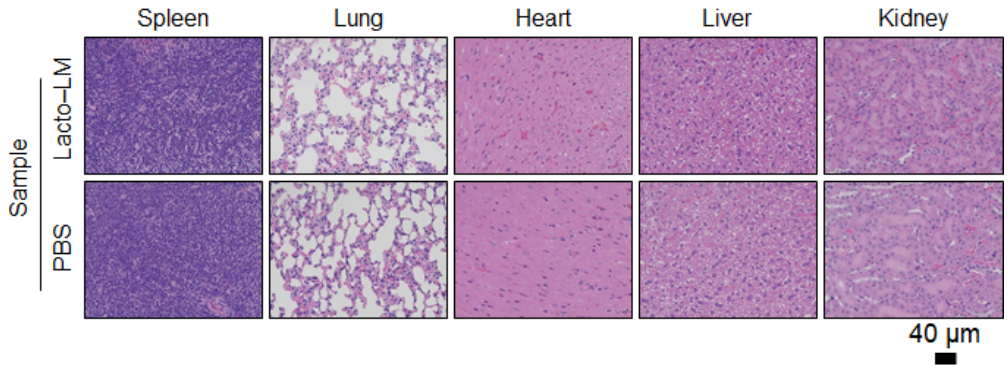

Figure 3.23 Hematoxylin and eosin (H&E) staining of major organs sectioned after intravenous injection of Lacto–LM or PBS after 7 d.

H&E and immunohistochemical (IHC) staining were further performed to assess the cellular-level suppressive effects. Tumor tissues were harvested 24 hours after sample administration and subjected to H&E, TUNEL, and cleaved caspase-3 staining. As shown in the representative images and quantitative analyses (Figure 3.24A and B), the Lacto–LM + laser group exhibited extensive tumor destruction and pronounced intracellular fragmentation, in stark contrast to the DSPE–PEG–LM + laser and PBS + laser groups. The Lacto–LM without laser group also displayed clear apoptotic features, albeit to a lesser extent, consistent with its intrinsic anticancer activity. Similarly, the Lacto and Lacto + laser groups demonstrated regions of necrosis, though less pronounced than those observed in the Lacto–LM groups, likely due to the enhanced tumor accumulation of Lacto–LM. By contrast, the PBS and DSPE–PEG–LM groups showed no discernible necrotic or apoptotic regions, in agreement with their negligible therapeutic effects. Collectively, these histological findings corroborate the potent antitumor efficacy of the Lacto–LM nanocomposite under laser irradiation.

The TUNEL assay further corroborated the H&E staining results, revealing widespread apoptotic regions in the Lacto–LM + laser group, thereby confirming that laser-irradiated Lacto–LM induced pronounced cell death (Figure 3.24A and B). Consistently, cleaved caspase-

3 staining closely mirrored the TUNEL findings, with the most prominent apoptotic areas observed in the Lacto–LM + laser–treated tumors. Notably, Lacto–LM administration followed by two rounds of laser irradiation led to marked tumor regression, which can be attributed to the synergistic contributions of photothermal ablation, the intrinsic immunostimulatory activity of the Lactococcus component, and the high photothermal conversion efficiency of the liquid metal core. Collectively, these results demonstrate that Lacto–LM–mediated photothermal immunotherapy represents an effective and safe multimodal therapeutic strategy, in which photothermal conversion and immune activation act synergistically to amplify anticancer efficacy.

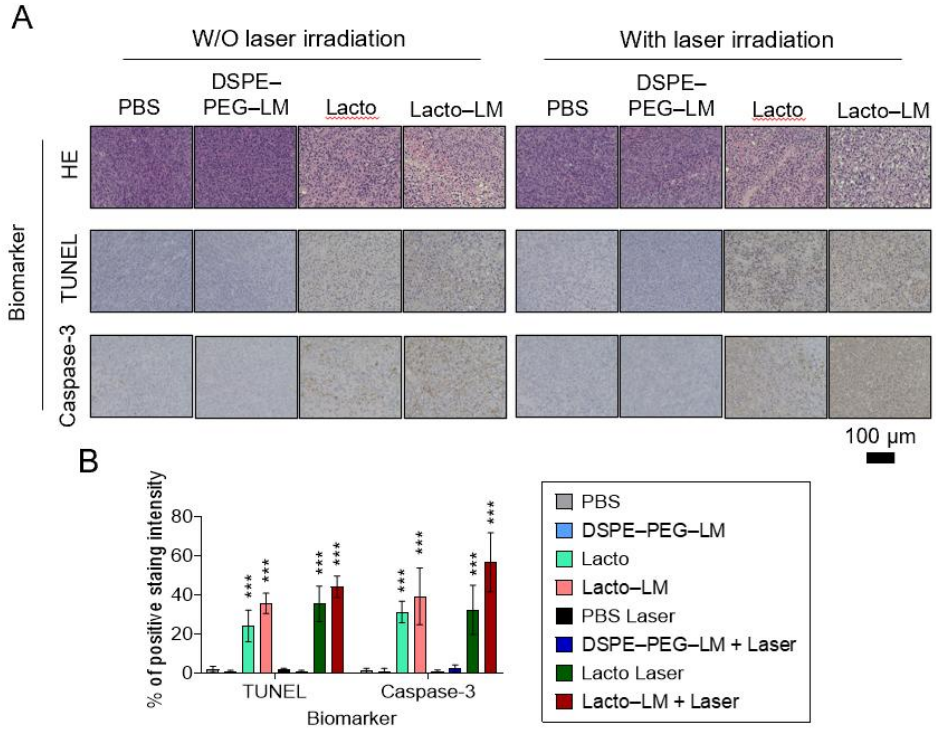

Figure 3.24 Representative histological and immunohistochemical analyses of tumor sections. A) Representative images of H&E, terminal deoxynucleotidyl transferase-mediated dUTP nick-end labeling (TUNEL), and caspase-3 stained tumor sections in the indicated groups. B) Statistical analyses of TUNEL and caspase-3 stained tumor tissues. Data are represented as mean ± standard error of the mean (SEM); n = 10 independent areas (regions of interest) in each tumor tissue collected from the groups of mice on day 1 after treatments. Statistical significance was calculated in

comparison with the PBS group. ***, $p < 0.001$, by Student's t-test.

3.4.4 Mechanism of action

Although PTT has shown outstanding efficacy in tumor treatment, recurrence and metastasis remain major challenges in cancer therapy[31-32]. These limitations are primarily attributed to the insufficient immune response during conventional PTT, which fails to establish a "hot" tumor microenvironment to prevent relapse and metastatic dissemination. To address this limitation, we engineered LM with Lactobacillus-derived components to enhance its immunogenicity, thereby addressing the inadequate therapeutic efficacy of traditional LM-based PTT systems.

To validate that Lacto-derived PAMPs drive both innate and adaptive immune activation, we first performed immunohistochemical (IHC) staining of key immunogenic cell death (ICD) markers and immune cell markers in tumor tissues following treatment with Lacto–LM nanocomposites. Specifically, we analyzed calreticulin and HMGB1 (ICD hallmarks), CD11c (mature dendritic cells), perforin and granzyme B (activated NK cells), as well as CD8 (cytotoxic T cells) and CD4 (helper T cells). Compared with the PBS and DSPE–LM groups, Lacto–LM treatment markedly enhanced ICD marker expression and significantly increased the activation and infiltration of adaptive immune cell populations within the tumor microenvironment (Figure 3.25). These comprehensive findings demonstrate that incorporation of Lacto-derived PAMPs enables Lacto–LM nanocomposites to elicit potent local and systemic antitumor immune responses.

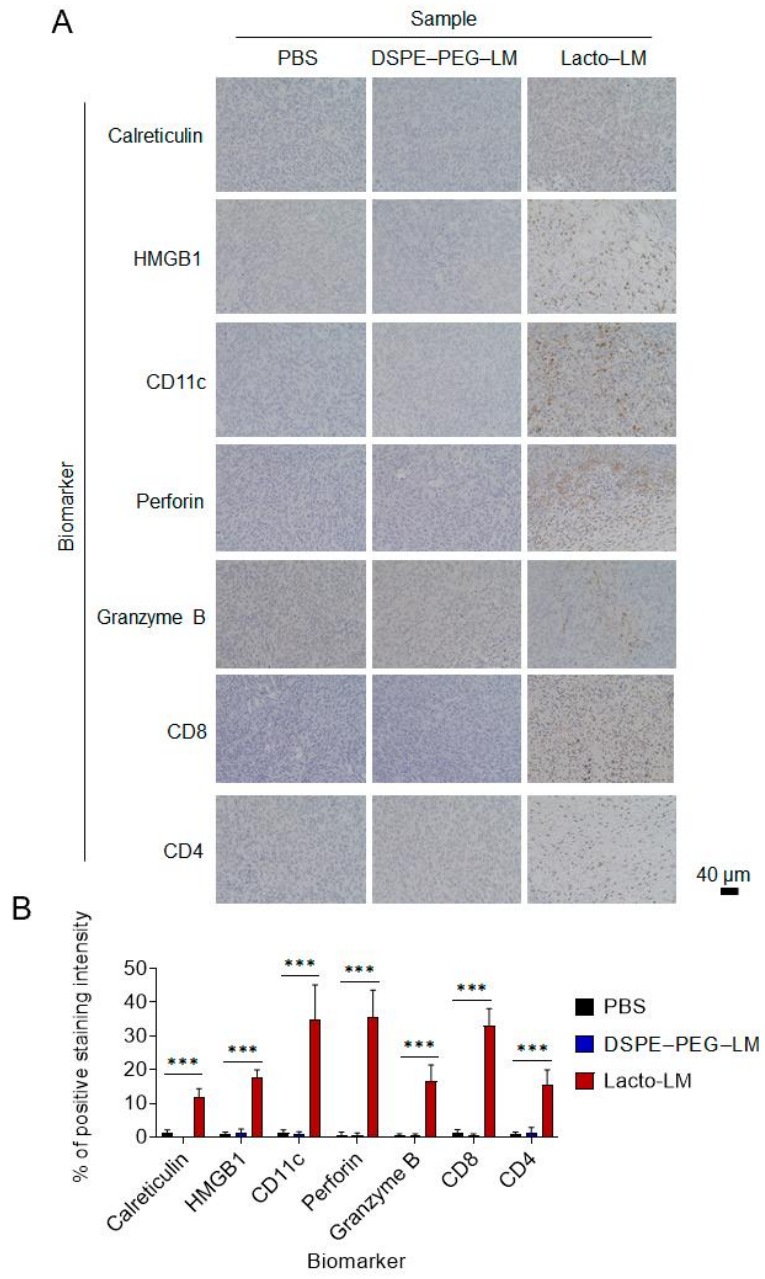

Figure 3.25 Immunohistochemical analysis of immune cell infiltration and immune-related marker expression in tumor tissues. A) Representative immunohistochemical (IHC) images of tumor sections collected 24 h after treatment with PBS, DSPE–PEG–LM, or Lacto–LM. Sections were stained for calreticulin and HMGB1 [immunogenic cell death (ICD) markers], CD11c (dendritic cell marker), perforin and granzyme B (cytotoxic effector molecules from NK cells), and CD8 and CD4 (T cell infiltration). B) Quantification of positive staining intensity. Data are presented as mean ± SD. Statistical significance was evaluated by one-way ANOVA followed by Tukey's post hoc test. ***$p < 0.001$; $N = 10$.

To clarify the underlying mechanism of the robust therapeutic effects, we performed polymerase chain reaction PCR analysis to evaluate immune cell populations and cytokine secretion within the tumor microenvironment 24 hours post-injection. The LM–Lacto formulation significantly enhanced the activation and infiltration of multiple immune cell subsets, including neutrophils, T cells, B cells, and macrophages (Figure 3.26A).. Moreover, pro-inflammatory cytokines such as TNF-α and IFN-γ were remarkably upregulated in the LM–Lacto group. This broad-spectrum immune activation highlights the capacity of LM–Lacto to function as an efficient immunostimulatory adjuvant in antitumor therapy. Importantly, the simultaneous activation of both innate immune cells (neutrophils, NK cells, macrophages) and adaptive immune cells (T and B lymphocytes) indicate the potential of LM–Lacto to bridge innate and adaptive immunity, thereby eliciting a coordinated and robust antitumor response against both primary and metastatic tumors.

As shown in Figure 3.26B and C, histological staining of key immune cell markers, including CXCR4 (neutrophils), F4/80 (macrophages), NKp49 (NK cells), CD19 (B cells), and CD3 (T cells), revealed that Lacto–LM under laser irradiation most significantly activated diverse immune cell populations and promoted the expression of anticancer cytokines. This robust immunological response can be attributed to the dual contribution of the photothermal effect from the LM core and the presence of Lacto-derived pathogen-associated molecular patterns (PAMPs), which engage pattern recognition receptors (PRRs) to initiate innate immune signaling. Notably, immunological activation was also observed in the Lacto and

Lacto–LM groups without laser irradiation, reflected by moderate but significant expression of immune biomarkers. This effect likely arises from the intrinsic immunostimulatory properties of Lacto components, which activate PRRs on antigen-presenting cells (APCs) to evoke systemic immune responses. In contrast, no evident immune activation was detected in the PBS or DSPE–PEG–LM groups, confirming that the observed immune stimulation originates from the Lacto components rather than the LM carrier itself.

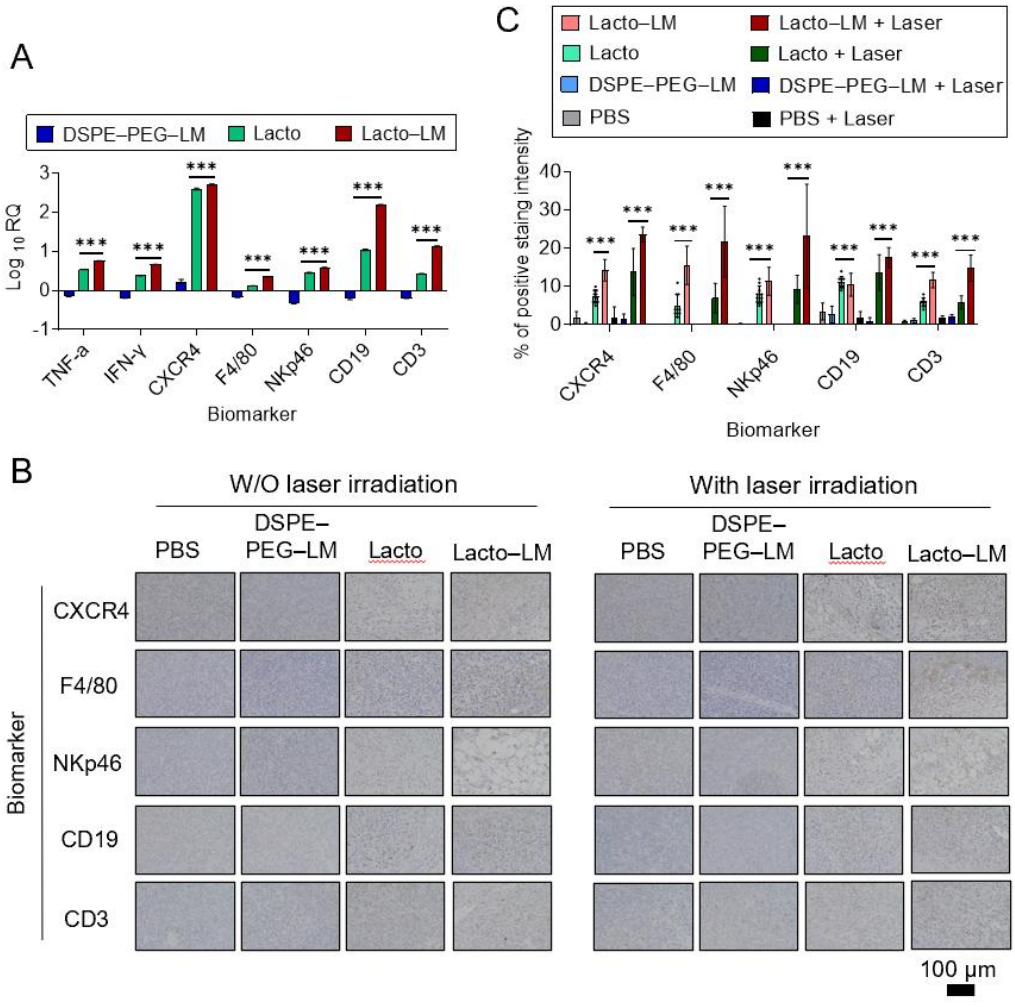

Figure 3.26 Mechanism of action of laser-induced Lacto–LM nanocomposites. A) Quantification of markers related to immune cells and cytokines by quantitative PCR (qPCR) after intravenous administration with Lacto–LM for 24 h. The mRNA expression of cytokines (IFN-γ and TNF-α), CXCR4 (neutrophil), F4/80 (macrophage), NKp46 (NK cell), CD19 (B cell), and CD3 (T cell) markers are shown as fold change (log10 relative quantification [RQ]) compared to that of the control

group (no-treatment). GAPDH gene expression was used as an internal control. N = 3 independent tumor tissues. B) Representative IHC images showing tumor-infiltrating various immune cells in the tumors of the indicated group. C) IHC analysis for the expression of CXCR4 (neutrophil), F4/80 (macrophage), NKp46 (NK cell), CD19 (B cell), and CD3 (T cell) in the tumors collected from different groups of mice at 24 h after laser irriadiation (n = 10 independent areas [region of interest] in each tumor tissue). Data are represented as mean ± standard error of the mean (SEM); Statistical significance was calculated in comparison with the PBS group. ***, $p < 0.001$, by Student's two-sided t-test.

Overall, the evidence of enhanced antitumor immunity can be attributed to several complementary mechanisms (Figure 3.27). First, laser-induced hyperthermia facilitates the release of damage-associated molecular patterns (DAMPs) and tumor-associated antigens from dying cancer cells, generating an inflammatory microenvironment conducive to immune cell recruitment and activation. Second, the Lacto-derived PAMPs provide persistent immunological stimulation to sustain long-term immune activation. Third, these processes establish a positive feedback loop that amplifies and prolongs antitumor immunity, ultimately leading to robust systemic immune responses.

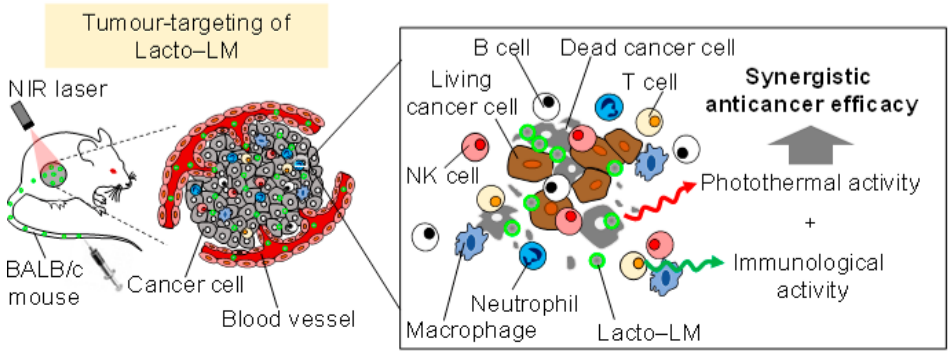

Figure 3.27 Schematic of the proposed mechanism of tumor targeting of Lacto-LM.

However, antitumor immune responses triggered by phototherapy alone remain suboptimal due to the weak immunogenicity of autologous tumor antigens, which limits their ability to prevent tumor recurrence and metastasis[32-33]. This limitation represents a critical therapeutic bottleneck that has hindered the clinical translation of PTT-based cancer treatments.

Consequently, we designed a laser-driven LM–Lacto platform specifically to elicit robust and sustained immune responses that address this fundamental limitation. Our experimental results demonstrated that Lacto–LM effectively induces an inflammatory and immunogenic tumor microenvironment, as evidenced by increased cytokine secretion and enhanced infiltration of diverse immune cell populations. This comprehensive immune activation creates a tumor-hostile microenvironment that not only facilitates primary tumor destruction but also establishes immunological surveillance against residual cancer cells and potential metastatic foci.

Collectively, these findings underscore the exceptional potential of Lacto–LM to enhance antitumor immunity through multiple complementary immunomodulatory mechanisms. The synergistic effects of immunological activation and photothermal properties establish Lacto–LM as a highly effective NIR PIT system with broad therapeutic applications across diverse cancer types. Moreover, the versatility of this platform suggests that Lacto–LM can be employed as a monotherapy for localized tumors or in combination with conventional immunotherapies to further amplify anticancer immune responses for systemic disease management.

3.4.5 Long-term immune memory

Given the potent immune-stimulating capacity of Lacto–LM, we hypothesized that it may also induce long-term immunological memory capable of preventing tumor recurrence. To evaluate this possibility, we performed a comprehensive tumor rechallenge experiment in which mice previously cured of primary tumors received a second subcutaneous inoculation of

Colon26 cells on day 76 after the initial treatment (Figure 3.28). This experimental design enables the assessment of protective memory responses under physiologically relevant conditions, closely mimicking the clinical scenario of cancer recurrence.

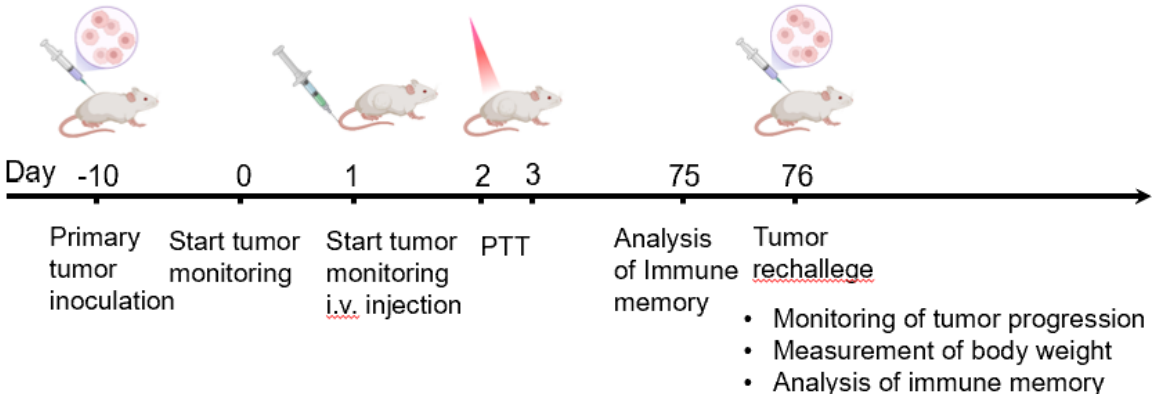

Figure 3.28 Schematic of memory effects analysis and tumor growth detection following secondary inoculation.

CD127 is a canonical marker of memory T cells, whose presence enables a rapid antigen-specific response, while CD27 serves as a marker of memory B cells, facilitating accelerated antibody production. Prior to the second tumor inoculation, we assessed the proportions of $CD127^+$ memory T cells and $CD27^+$ memory B cells in the spleen using flow cytometry to evaluate immunological memory induced by Lacto–LM. Compared with control mice, laser-activated Lacto–LM treatment significantly increased both $CD127^+$ memory T cells and $CD27^+$ memory B cells (Figure 3.29) indicating robust activation of the immunological memory system[34-35]. The concurrent induction of cellular and humoral immunity establishes a formidable barrier against tumor recurrence.

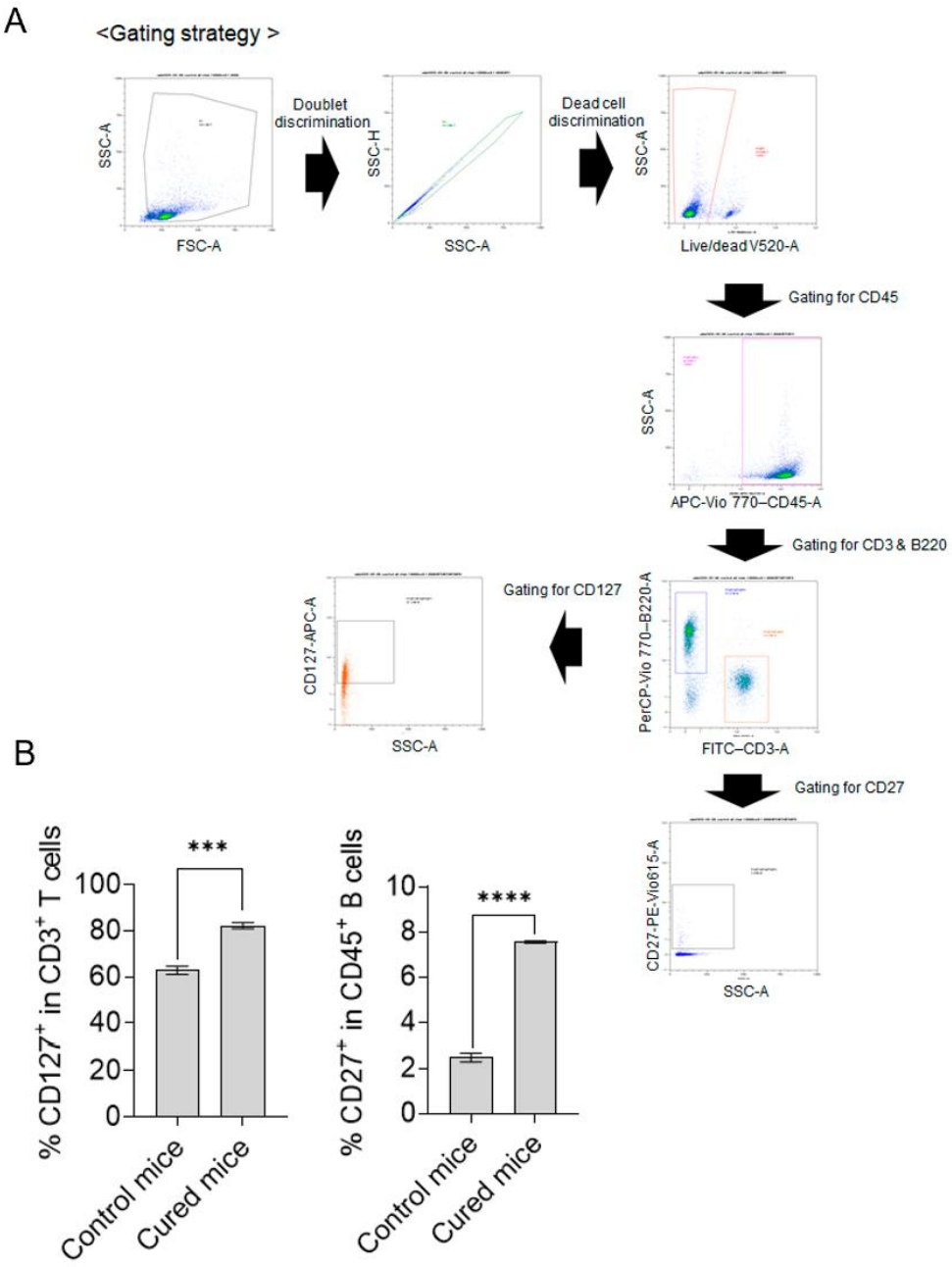

Figure 3.29 Flow cytometric analyses of expression of Memory T cells and B cells in the cured BALB/c mice after the treatment of laser-induced Lacto–LM nanocomposites. A) Gating strategy for flow cytometric analyses of expression of CD127+ in CD3+ T cells and CD27+ in CD45+ B cells in spleen of the mice The gating strategy shows representative examples for identification of memory T anc B cells. B) Flow cytometric analyses of CD127+ T cells and CD27+ B cells in the cured mice after treatment (n = 3 biologically independent tests). Data are presented as mean ± standard error of the mean (SEM); Statistical significance was calculated by comparing with the no-treatment group. ***, $p < 0.001$ and ****, $p < 0.0001$ by Student's two-sided t test.

Following the second tumor inoculation, tumor growth was monitored over a 16-day period to assess the functional efficacy of the established immune memory. Mice previously treated with Lacto–LM + laser exhibited complete tumor rejection with no detectable tumor growth after the second challenge (Figure 3.30). This remarkable protective effect demonstrates that the initial Lacto–LM treatment established robust and functionally competent immune memory capable of preventing tumor establishment upon re-exposure. By day 16, the average tumor volume in the control group exceeded 400 mm^3, whereas no tumor recurrence was observed in cured mice following laser-induced Lacto–LM treatment, highlighting the profound and durable nature of the treatment-induced immune protection.

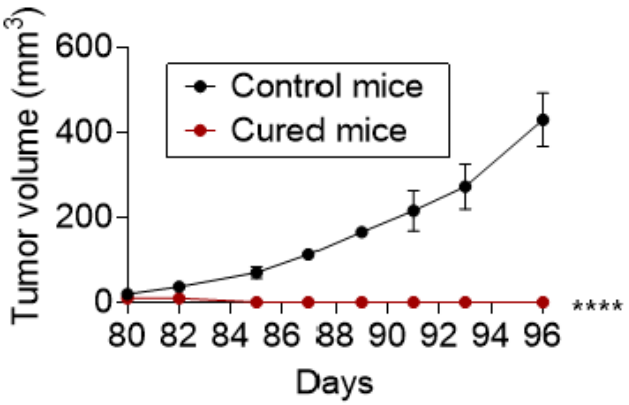

Figure 3.30 Tumor growth curve for each group after the second tumor inoculation. (n = 3 biologically independent tests). Data are presented as mean ± SEM. Statistical significance was calculated by comparison with the control group. ****, $p < 0.0001$ by Student's two-sided t test.

The mechanism underlying this potent photothermal immune memory can be attributed to three complementary aspects. First, the immunostimulatory constituents of Lacto reshape the tumor microenvironment into an immunogenic state, thereby enhancing antigen recognition and presentation. Second, photothermal destruction of tumor cells induces the release of diverse damage-associated molecular patterns (DAMPs), with tumor-associated antigens serving as critical stimuli for the development of immune memory. Third, Lacto-derived

PAMPs not only augment conventional immune activation but also directly promote the differentiation of memory cell populations. Collectively, these synergistic effects result in the establishment of systemic, long-term immune memory capable of preventing tumor regrowth.

The body weight of mice remained stable throughout the experiment (Figure 3.31), indicating the absence of adverse effects and further demonstrating the safety of Lacto–LM–mediated PIT. This stability is particularly important in long-term immune memory studies, as chronic inflammation or autoimmune responses could compromise both safety and efficacy. The negligible changes in body weight suggest that the immune memory established by Lacto–LM treatment is specifically directed against tumor antigens, rather than inducing generalized autoimmune activation.

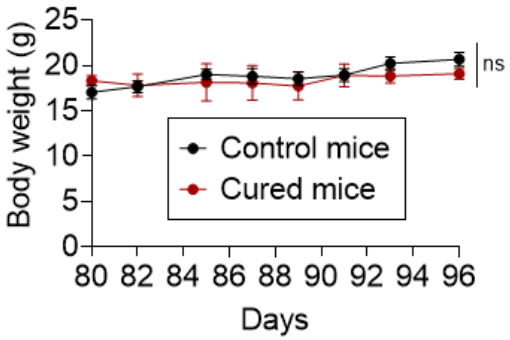

Figure 3.31 Average body weight of mice after tumor rechallenge. (n = 3 biologically independent tests). Data are presented as mean ± SEM. Statistical significance was calculated by comparing with the control group. ns, not significant by Student's two-sided t test.

This comprehensive investigation demonstrates that Lacto–LM under laser irradiation induces a robust and durable immune response capable of preventing both tumor relapse and metastasis upon secondary rechallenge, in addition to rapidly eradicating primary tumors. These findings highlight a substantial advantage of the Lacto–LM–mediated PIT platform over

conventional PTT, which generally achieves only transient ablation of solid tumors without providing long-lasting immunological surveillance or protection. The durable immune memory elicited by Lacto–LM positions this approach as a transformative therapeutic strategy to overcome two of the most fundamental challenges in oncology—tumor recurrence and metastatic dissemination—through sustained immune surveillance

3.5 Conclusion

We have developed a biomimetic liquid metal (LM) nanocomposite through a straightforward one-step sonication of LM with Lactobacillus-derived bioactive components. This strategy enables the functional coating of LM with bacterial ingredients, thereby enhancing both the aqueous dispersibility and immunogenicity of the nanocomposite.

In summary, this facile approach provides two major advantages. First, the incorporation of Lactobacillus components markedly improves the aqueous dispersibility of LM, which enhances its biocompatibility, promotes tumor accumulation, and ultimately achieves exceptional photothermal conversion efficiency at the tumor site. Second, the lacto-derived ingredient itself acts as an immune adjuvant, amplifying antitumor immune responses by stimulating tumor-associated antigens released during LM-mediated photothermal therapy. Beyond these individual contributions, the synergistic integration of LM and bacterial components enables both effective primary tumor ablation and the induction of long-term systemic immune memory.

Our in vivo experiments demonstrated that Lacto–LM precisely localized to tumors and mediated efficient photothermal ablation under laser irradiation (Figure 3.32). During this process, both the *Lactobacillus*-derived PAMPs and the tumor-derived fragments and necrotic cells generated by hyperthermal stress synergistically trigger the innate and adaptive immune responses. This was evidenced by the upregulation of ICD markers (calreticulin and HMGB1), increased secretion of pro-inflammatory cytokines such as TNF-α and IFN-γ, and enhanced immune cell infiltration, including neutrophils, NK cells, T cells, B cells, and memory subsets.

Furthermore, IHC analysis revealed an elevated presence of $CD11c^+$ dendritic cells, $perforin^+$/granzyme B^+ NK cells, and both $CD8^+$ cytotoxic and $CD4^+$ helper T cells within the tumor microenvironment. Collectively, these findings demonstrate that Lacto–LM possesses the capacity to reprogram the immunosuppressive tumor microenvironment and to establish durable protective immunity, thereby preventing metastasis and recurrence.

While the outcomes of this study are encouraging, several limitations should be noted. First, the antitumor effects were evaluated in a subcutaneous tumor model, which may not fully recapitulate the complex characteristics of tumors in the clinical setting. Second, although pronounced immune activation was observed and preliminary safety was confirmed after a single injection, the precise molecular pathways underlying the immune response remain to be elucidated. Finally, the long-term toxicity and biosafety of the nanocomposite require further systematic investigation. However, given the superior photothermal performance of LM, the accessibility and low cost of *Lactobacillus* components, and the simplicity of the one-step sonication synthesis, this platform holds strong potential for translation into clinical trials as an immune-activating nanotherapeutic. We anticipate that this work will lay the foundation for future research aimed at developing more efficient, adaptable, and practical photothermal immunotherapy systems.

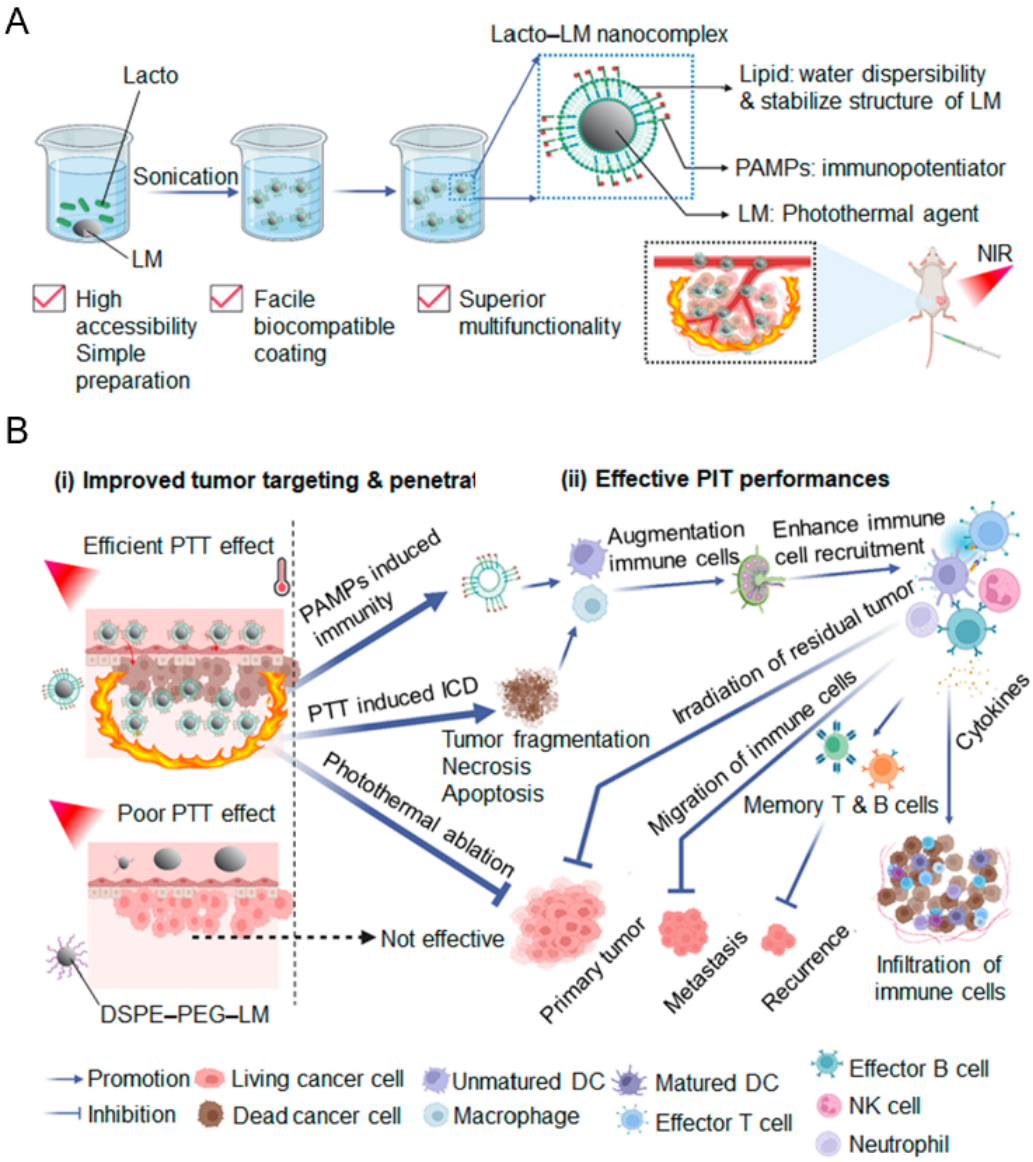

Figure 3.32 Schematic of photothermal immunotherapy (PIT) using biomimetic Lacto–LM nanocomposites. A) Facile synthesis of Lacto–LM nanocomposites. Lacto–LM is synthesized via a single-step sonication of LM with Lacto for 10 min. B) Schematic of the anticancer mechanism of laser-induced Lacto–LM. Lacto–LM exhibits enhanced tumor accumulation and penetration capabilities, which are crucial for effective PIT. Beyond the photothermal ablation of the primary tumor, laser-induced Lacto–LM induces abundant hyperthermia-triggered immunogenic cell death (ICD) while also promoting the release of pathogen-associated molecular patterns (PAMPs). These processes synergistically enhance dendritic cell (DC) maturation, thereby eliciting diverse immune cell infiltration. This amplified immune activation not only targets residual primary and metastatic tumors but also establishes durable immune memory, effectively preventing tumor recurrence. Conversely, DSPE–PEG–LM exhibits inferior tumor accumulation and penetration, resulting in limited PIT efficacy.

3.6 Reference

[1] G. Pagona, G. E. Zervaki, A. S. D. Sandanayaka, O. Ito, G. Charalambidis, T. Hasobe, A. G. Coutsolelos, N. Tagmatarchis, *J. Phys. Chem. C.* **2012**, *116*, 9439.

[2] Y. Yu, E. Miyako, *iScience.* **2018**, *3*, 134.

[3] Y. Yu, E. Miyako, *Chemistry (Easton).* **2018**, *24*, 9456.

[4] Y. Li, G. Bai, S. Zeng, J. Hao, *ACS Appl Mater Interfaces.* **2019**, *11*, 4737.

[5] J. Li, K. Pu, *Acc. Chem. Res.* **2020**, *53*, 752.

[6] Y. Ma, S. Yu, S. Ni, B. Zhang, A. C. F. Kung, J. Gao, A. Lu, G. Zhang, *Frontiers in cell and developmental biology.* **2021**, *9*, 626910.

[7] W. Xie, F. M. Allioux, J. Z. Ou, E. Miyako, S. Y. Tang, K. Kalantar-Zadeh, *Trends Biotechnol.* **2021**, *39*, 624.

[8] Q. Yun, A. Kimura, M. Taguchi, E. Miyako, *Appl. Mater. Today.* **2022**, *26*, 101302.

[9] J. J. Hu, M. D. Liu, F. Gao, Y. Chen, S. Y. Peng, Z. H. Li, H. Cheng, X. Z. Zhang, *Biomaterials.* **2019**, *217*, 119303.

[10] P. Zhu, S. Gao, H. Lin, X. Lu, B. Yang, L. Zhang, Y. Chen, J. Shi, *Nano Lett.* **2019**, *19*, 2128.

[11] Y. Goto, S. Iwata, M. Miyahara, E. Miyako, *Adv. Sci.* **2023**, *10*, 2301679.

[12] S. Chintalapati, S. Iwata, M. Miyahara, E. Miyako, *Biomed. Pharmacother.* **2024**, *170*, 116041.

[13] B. Routy, E. Le Chatelier, L. Derosa, C. P. M. Duong, M. T. Alou, R. Daillère, A. Fluckiger, M. Messaoudene, C. Rauber, M. P. Roberti, M. Fidelle, C. Flament, V. Poirier-Colame, P. Opolon, C. Klein, K. Iribarren, L. Mondragón, N. Jacquelot, B. Qu, G. Ferrere, C. Clémenson, L. Mezquita, J. R. Masip, C. Naltet, S. Brosseau, C. Kaderbhai, C. Richard, H. Rizvi, F. Levenez, N. Galleron, B. Quinquis, N. Pons, B. Ryffel, V. Minard-Colin, P. Gonin, J. C. Soria, E. Deutsch, Y. Loriot, F. Ghiringhelli, G. Zalcman, F. Goldwasser, B. Escudier, M. D. Hellmann, A. Eggermont, D. Raoult, L. Albiges, G. Kroemer, L. Zitvogel, *Science.* **2018**, *359*, 91.

[14] L. F. Mager, R. Burkhard, N. Pett, N. C. A. Cooke, K. Brown, H. Ramay, S. Paik, J. Stagg, R. A. Groves, M. Gallo, I. A. Lewis, M. B. Geuking, K. D. McCoy, *Science.* **2020**, *369*, 1481.

[15] K. L. Bersch, K. E. DeMeester, R. Zagani, S. Chen, K. A. Wodzanowski, S. Liu, S. Mashayekh, H. C. Reinecker, C. L. Grimes, *ACS Cent Sci.* **2021**, *7*, 688.

[16] P. A. Bron, M. Kleerebezem, *Front. Microbiol.* **2018**, *9*, 1821.

[17] R. Tenchov, J. M. Sasso, Q. A. Zhou, *Bioconjug. Chem.* **2023**, *34*, 941.

[18] W. Hu, A. Mao, P. Wong, A. Larsen, P. J. Yazaki, J. Y. C. Wong, J. E. Shively, *Bioconjug. Chem.* **2017**, *28*, 1777.

[19] C. M. Hessel, V. P. Pattani, M. Rasch, M. G. Panthani, B. Koo, J. W. Tunnell, B. A. Korgel, *Nano Lett.* **2011**, *11*, 2560.

[20] G. Modugno, C. Ménard-Moyon, M. Prato, A. Bianco, *Br. J. Pharmacol.* **2015**, *172*, 975.

[21] J. Yan, X. Zhang, Y. Liu, Y. Ye, J. Yu, Q. Chen, J. Wang, Y. Zhang, Q. Hu, Y. Kang, M. Yang, Z. Gu, *Nano Res.* **2019**, *12*, 1313.

[22] X. Sun, M. Sun, M. Liu, B. Yuan, W. Gao, W. Rao, J. Liu, *Nanoscale.* **2019**, *11*, 2655.

[23] L. Pirkkala, P. Nykänen, L. Sistonen, *FASEB J.* **2001**, *15*, 1118.

[24] S. Fulda, A. M. Gorman, O. Hori, A. Samali, *Int. J. Cell Biol.* **2010**, *2010*, 214074.

[25] S. N. Bhatia, X. Chen, M. A. Dobrovolskaia, T. Lammers, *Nat. Rev. Cancer.* **2022**, *22*, 550.

[26] Q. Jin, Y. Deng, X. Chen, J. Ji, *ACS Nano.* **2019**, *13*, 954.

[27] R. Ma, N. Alifu, Z. Du, S. Chen, Y. Heng, J. Wang, L. Zhu, C. Ma, X. Zhang, *Int. J. Nanomed.* **2021**, *16*, 4847.

[28] L. Chen, D. B. Flies, *Nat. Rev. Immunol.* **2013**, *13*, 227.

[29] J. H. Esensten, Y. A. Helou, G. Chopra, A. Weiss, J. A. Bluestone, *Immunity.* **2016**, *44*, 973.

[30] C. Yunna, H. Mengru, W. Lei, C. Weidong, *Eur. J. Pharmacol.* **2020**, *877*, 173090.

[31] L. Sun, F. Shen, L. Tian, H. Tao, Z. Xiong, J. Xu, Z. Liu, *Adv. Mater.* **2021**, *33*, 2007910.

[32] C. Zhao, C. Wang, W. Shan, Z. Wang, X. Chen, H. Deng, *Acc. Chem. Res.* **2024**, *57*, 905.

[33] E. S. Vitetta, M. T. Berton, C. Burger, M. Kepron, W. T. Lee, X. M. Yin, *Annu. Rev. Immunol.* **1991**, *9*, 193.

[34] T. Chu, J. Berner, D. Zehn, *Nat. Immunol.* **2020**, *21*, 1484.

[35] K. Agematsu, *Histol. Histopathol.* **2000**, *15*, 573.

Chapter 4 Blood-camouflaged liquid metal nanoplatform mediates Treg depletion and STING-amplified photothermal immunity for metastatic TNBC therapy

4.1 Introduction

Breast cancer (BC) the most common malignancy and a leading cause of cancer-related mortality worldwide, with triple-negative breast cancer (TNBC) accounting for approximately 15–20% of all cases[1-2]. TNBC, defined by the absence of HER2 expression and the lack of both estrogen and progesterone receptors, represents the most aggressive and heterogeneous subtype of breast cancer[3]. It is clinically characterized by rapid progression, poor prognosis, and limited therapeutic options. TNBC patients exhibit a nearly three-fold higher risk of metastasis within five years of diagnosis compared with non-TNBC cases, with the lungs being the most common sites of recurrence and distal metastasis[4-5].

Despite the use of chemotherapy, surgery, and radiotherapy as standard treatment modalities, TNBC remains highly prone to therapeutic resistance, early relapse, and metastatic dissemination, resulting in dismal clinical outcomes[6]. Immunotherapy has recently emerged as a promising strategy for TNBC management. Immune checkpoint inhibitors (ICIs) targeting cytotoxic T-lymphocyte–associated antigen 4 (CTLA-4) and programmed cell death protein 1 (PD-1)/ligand 1 (PD-L1) have demonstrated improved survival in subsets of patients with solid tumors, including TNBC[7]. Unfortunately, less than 20% of TNBC patients exhibit beneficial responses to ICIs, likely due to the profoundly immunosuppressive tumor microenvironment (TME)[8-11]. Substantial evidence indicates that, compared with other breast cancer subtypes,

TNBC is more prone to immune evasion, therapy resistance, and early recurrence, primarily attributed to the extensive infiltration of regulatory T cells (Tregs) within the TME[12-15].

Regulatory T cells (Tregs) serve as the central regulatory governing the immunosuppressive tumor microenvironment (TME). They directly inhibit cytotoxic $CD8^+$ T-cell activation, restrain dendritic cell maturation, and induce M2-like macrophage polarization through cytokine- and chemokine receptor – mediated signaling. By secreting immunosuppressive mediators such as IL-10 and TGF-β, Tregs establish a profoundly tolerant milieu that promotes tumor immune evasion and metastatic dissemination while impeding antitumor immune responses[16]. Clinically, elevated intratumoral densities of $FOXP3^+$ Tregs are strongly correlated with reduced relapse-free and overall survival in breast cancer patients, highlighting their critical role in immune escape and disease progression[17]. Therefore, selective depletion of Tregs effectively "releases the immunological brake," which is pivotal for reprogramming the suppressive TME and restoring cytotoxic immunity, thereby achieving robust and durable immunotherapeutic efficacy in triple-negative breast cancer (TNBC).

Nanomaterial-based photothermal therapy (PTT) has been extensively explored in both clinical cancer treatment and fundamental research owing to its high efficiency, precise controllability, and minimally invasive nature[18-20]. By utilizing photothermal conversion agents that transform laser energy into localized heat, PTT can induce rapid thermal ablation of tumor tissues and effectively suppress the growth of primary tumors. However, PTT alone cannot completely eradicate malignant tumors, as in situ recurrence and distant metastasis after hyperthermia ablation remain the leading causes of cancer-related mortality[21] [22-24]In addition

to direct tumor eradication, PTT also induces immunogenic cell death (ICD) through heat-induced stress and pyroptosis. During this process, tumor cells release abundant damage-associated molecular patterns (DAMPs) and tumor-associated antigens (TAAs), which promote dendritic cell (DC) maturation, enhance cytotoxic T lymphocyte (CTL) infiltration, and initiate potent antitumor immune responses[25-26]. However, the immune stimulation triggered by PTT-induced ICD is typically transient and limited, primarily due to the insufficient responsiveness of antigen-presenting cells (APCs) and the rapid attenuation of the inflammatory signaling cascade. Consequently, PTT alone rarely achieves systemic or long-lasting immune protection.

Recent investigations have demonstrated that the stimulator of the cGAS (cyclic GMP-AMP synthase)-STING (stimulator of interferon genes) pathway plays pivotal roles in initiating anti-tumor immunity, thereby emerging as a promising therapeutic target for tumor immunotherapy[27]. The cGAS-STING signaling pathway facilitates the maturation and activation of various immune cells, including T cells, dendritic cells (DCs), and natural killer cells (NK cells), through the induction of pro-inflammatory cytokine expression, particularly, type I interferon (IFN-I), thereby stimulating and augmenting both innate and adaptive immune responses to elicit potent anti-tumor immune effects[28]. To overcome the limitations of PTT-induced transient immunity, integrating PTT with a STING agonist represents a rational strategy to amplify innate immune signaling, enhance the utilization of tumor-derived antigens, and synergistically induce robust and durable antitumor immunity.

Gallium-based liquid metals (LMs) have recently gained significant attention as promising photothermal materials owing to their excellent biocompatibility, intrinsic fluidity,

and superior photothermal conversion efficiency[29-36]. However, their poor aqueous dispersibility, high tendency to aggregate, and rapid clearance by the immune system greatly limit their therapeutic applicability[37-38]. Red blood cell (RBC) membrane–camouflaging strategies have been widely used to prolong systemic circulation of nanoparticles and reduce immune clearance[39-40]. However, these approaches typically require complex membrane extraction and purification steps, which can compromise the structural integrity and bioactivity of membrane components[41-42]. To overcome these obstacles, we instead innovatively adopt a facile whole-blood–biomimetic approach to engineer liquid-metal (LM) nanoparticles, whereby the nanoplatform directly interfaces with whole blood to preserve the natural protein corona and dynamic plasma constituents, thereby enhancing LM colloidal stability, conferring immune-evasion capability, and improving tumor-accumulation efficiency.

4.2 The objective of this chapter

We present a whole-blood-camouflaged liquid-metal nanoplatform that integrate Treg depletion and STING activation for TNBC photothermal immunotherapy. Through a facile one-step ultrasonication method with whole blood, the solubility and colloidal stability of liquid metal nanoparticles were markedly improved, enabling their efficient accumulation at tumor sites and the generation of robust photothermal ablation under NIR irradiation. By integrating anti-CD25 antibodies and the STING agonist DMXAA, this multifunctional platform was designed to simultaneously relieve immune suppression and remodel the tumor immune microenvironment, thereby eliciting potent antitumor immunity Mechanistically, The conjugated anti-CD25 effectively depleted the abundant Treg population in TNBC, while the

released DMXAA acted synergistically with heat-induced tumor-associated antigens to ignite strong and durable systemic antitumor immune responses. Ultimately, this biomimetic Blood-LM nanoplatform achieved effective eradication of primary TNBC tumors and significant inhibition of pulmonary metastasis. This work not only establishes a new paradigm for liquid-metal-based photothermal immunotherapy but also presents an effective therapeutic strategy against fatal TNBC.

4.3 Materials and methods

4.3.1 Preparation of B–LM–DMXAA–αCD25 nanocomposites

Preparation of B–LM–DMXAA

Gallium–indium eutectic alloy (Ga:In = 75.5:24.5 wt%; Alfa Aesar) was dispersed in phosphate-buffered saline (PBS) containing 1 mg mL^{-1} DSPE–PEG–NH_2 and 1 mg mL^{-1} DMXAA (5,6-dimethylxanthenone-4-acetic acid; CAS No. 117570-53-3; Lot No. TLW2JNF; Tokyo Chemical Industry Co., Ltd., Tokyo, Japan). Subsequently, 500 μL of freshly collected murine whole blood was added, and the mixture was subjected to probe-type sonication (VCX-600, Sonics, USA; 10 min, ice bath) to generate blood membrane–camouflaged liquid metal nanoparticles (B–LM–DMXAA). The final concentrations of liquid metal and DMXAA were 3 mg mL^{-1} and 1 mg mL^{-1}, respectively.

Conjugation of αCD25 Antibody

DSPE–PEG–NHS (1 mg) and anti-CD25 monoclonal antibody (1 mg) were mixed and incubated overnight at 4 °C to enable covalent conjugation. The reaction mixture was purified using a 100 kDa Amicon® centrifugal filter to remove excess DSPE–PEG–NHS. The obtained

DSPE–PEG–anti-CD25 conjugate was then added to the preformed B–LM–DMXAA suspension, followed by gentle vortexing and incubation at 4 °C for 30 min to produce the final B–LM–DMXAA–αCD25 nanocomposites. The concentration of conjugated anti-CD25 was maintained at 1 mg mL^{-1}.

Similarly, DSPE–PEG–LM nanoparticles were prepared by dispersing 30 mg of LM in 10 mL of PBS containing 3 mg of DSPE–PEG_{2000}–NH_2 (Yuka Sangyo Co., Ltd, Tokyo, Japan), followed by sonication under identical conditions.

ICG–B–LM-DMX-αCD25, 0.2 mg of ICG (Tokyo Chemical Industry, Tokyo, Japan) was added to 1 mL of the synthesized B–LM-DMX-αCD25 solution, followed by vertexing for 1 min in the dark. ICG–DSPE–PEG–LM was prepared using the same method as that used for the addition of DSPE–PEG–LM. Additionally, a highly concentrated ICG–Lacto–LM suspension was obtained by proportionally increasing the amounts of Lacto–LM and ICG.

4.3.2 Structural and optical characterization

The morphology and composition of B–LM-DMX-αCD25, DSPE–PEG–LM, and pristine LM were meticulously analyzed using high-resolution TEM (Model JEM-2010; JEOL Ltd., Tokyo, Japan) at an acceleration voltage of 200 kV. TEM analyses were conducted at Hanaichi Ultra Structure Research Institute Co., Ltd., Aichi, Japan. The hydrodynamic diameter of the nanoparticles was determined using DLS (Zetasizer Nano ZS; Malvern Panalytical, UK). Additionally, the optical properties including absorbance and FL were characterized using UV–vis–NIR (Model V-730 BIO; Jasco Corporation, Tokyo, Japan) and fluorescence (Model FP-6500; Jasco Corporation) spectrometers, respectively.

The encapsulation efficiency (EE) of DMXAA was quantified by UV absorbance at 380 nm using a standard calibration curve, calculated as

$$EE(\%) = \frac{W_{\text{loaded}}}{W_{\text{total}}} \times 100\%.$$

The encapsulation efficiency (EE) of anti-CD25 in B–LM–DMXAA–αCD25 nanocomposites was determined after purification through a 200 kDa ultrafiltration units (Item No. USY-20, Lot No. 50513U12; Tokyo Roshi Kaisha, Ltd., Tokyo, Japan) to remove unbound antibodies. The protein content was quantified using a bicinchoninic acid (BCA) assay kit (Thermo Fisher Scientific, USA) according to the manufacturer's protocol. The EE (%) was calculated using the equation:

$$EE(\%) = \frac{W_{\text{loaded}}}{W_{\text{total}}} \times 100\%,$$

where W_{loaded} represents the amount of antibody encapsulated in the nanoparticles and W_{total}denotes the total amount of antibody initially added.

To evaluate the photothermal-responsive release behavior of DMXAA, 1 mL of the B–LM–DMXAA suspension was exposed to an 808 nm near-infrared (NIR) laser (1.0 W cm^{-2}) for varying durations (0–15 min). At predetermined time points, aliquots were withdrawn and ultracentrifuged using Amicon® 10 kDa ultrafiltration tubes (Cat. No. UFC501096, Lot No. 0000391056, Merck Millipore Ltd, Burlington, MA, USA) to separate the released fraction. The filtrates were subsequently analyzed spectrophotometrically to quantify the concentration of released DMXAA. The cumulative release percentage was calculated and plotted as a function of laser irradiation time.

4.3.3 Photothermal conversion efficiency

The photothermal transduction of B–LM–DMXAA–αCD25 nanocomposite dispersion was assessed by irradiating the solution (Milli-Q water served as a control) with an 808 nm NIR laser (Civil Laser, Hangzhou, Zhejiang, China) at varying power outputs of 0.5 W (ca. 25.5 mW/mm^2, spot diameter ~5 mm), 1.0 W (ca. 51 mW/mm^2), or 1.5 W (ca. 76.5 mW/mm^2). The thermal responses of the solutions were continuously monitored *in situ* using a high-precision temperature sensor (Model AD-5601A; A&D Co.), and infrared thermographic imaging (Model i7; FLIR Systems, Nashua, NH, USA) was employed to visually capture the thermal distribution patterns. The photothermal conversion efficiency (η) of B–LM–DMXAA–αCD25 was determined following previously established methods [13–15]. using the equation:

$$\eta = hS(T_{Max} - T_{Surr}) - Q_{Dis} / I(1 - 10^{-A808}) \quad (1)$$

Where η is the photothermal conversion efficiency of nanoparticles, h is the heat transfer coefficient, S is the surface area of the container, and the value of hS is obtained from the Eq. 2. T_{max} is the maximum steady temperature of the nanoparticle solution, and T_{Surr} is the environmental temperature. I and A_{808} represent the laser power and absorbance, respectively, at a laser wavelength of 808 nm. Q_{Dis} represents the heat dissipated from the light absorbed by the solvent and container.

$$hS = m_D C_D / \tau_s \quad (2)$$

where, m_D and C_D are the mass and heat capacities of the solvent, respectively. A sample system time constant τ_s can be calculated by Eq.3.

$$t = -\tau_s \ln(\theta) \quad (3)$$

A dimensionless parameter θ is introduced as followed:

$$\theta = T - T_{Surr} / T_{Max} - T_{Surr} \quad (4)$$

To assess the photothermal stability of the nanocomposites, B–LM–DMXAA–αCD25 samples (500 μg mL^{-1}) were subjected to five consecutive cycles of 808 nm laser irradiation (1.5 W cm^{-2}, ≈76.5 mW mm^{-2}; laser spot diameter ~5 mm) with alternating 5 min on/off intervals. The temperature variation during each cycle was continuously recorded using an infrared thermal camera to monitor the reproducibility of the heating–cooling process. The UV–vis–NIR absorption spectra of the samples before and after repeated laser exposure were measured using a UV–vis spectrophotometer (V-770, JASCO, Japan) to evaluate potential structural or optical changes in the nanocomposites.

4.3.4 Cell culture and viability

Murine breast cancer (4T1-Luc), murine macrophage (RAW 264.7), and human lung fibroblast (MRC-5) cell lines were obtained from the Japanese Collection of Research Bioresources (JCRB) Cell Bank (Tokyo, Japan). Drug-resistant murine mammary tumor (EMT6/AR1) cells were purchased from KAC Co., Ltd. (Tokyo, Japan). 4T1-Luc cells were cultured in Roswell Park Memorial Institute (RPMI) 1640 medium (Gibco, Grand Island, NY, USA) supplemented with 10% fetal bovine serum (FBS), 2 mM L-glutamine, 1 mM sodium pyruvate, gentamicin (50 μg mL^{-1}), and 100 IU mL^{-1} penicillin–streptomycin. MRC-5 and RAW 264.7 cells were maintained in Minimum Essential Medium (MEM, NACALAI TESQUE, Inc., Kyoto, Japan) containing the same supplements. All cells were incubated at 37 °C in a humidified atmosphere with 5% CO_2.EMT6/AR1 cells were cultured in Cell Growth

Medium No. 104 (KAC Co., Ltd., Tokyo, Japan) containing doxorubicin (1 μg mL^{-1}) and 100 IU mL^{-1} penicillin–streptomycin. All cells were incubated at 37 °C in a humidified atmosphere containing 5% CO_2. To prevent genetic drift and maintain phenotypic stability, cells were periodically revived from low-passage cryopreserved stocks stored in liquid nitrogen.

Cell viability was evaluated using a Cell Counting Kit-8 (CCK-8) assay (Dojindo Laboratories, Kumamoto, Japan) following the manufacturer's protocol. Briefly, 1×10^4 cells/well were seeded in 96-well plates and allowed to adhere overnight before exposure to nanoparticles and laser irradiation, as specified. Following treatment, the cells were washed with fresh medium and incubated with CCK-8 solution for 2 h at 37 °C. The absorbance was measured at 450/690 nm using a microplate reader to quantify cell viability.

4.3.5 Intracellular penetration of nanocomposites

Fluorescence spectral analysis:

ICG–B–LM–DMX–αCD25 nanocomposites (LM concentration = 300 μg mL^{-1}, ICG concentration = 12.5 μg mL^{-1}) were dispersed in phosphate-buffered saline (PBS) and analyzed using a fluorescence spectrometer (excitation wavelength: 750 nm). The fluorescence spectra were compared among free ICG, B–LM, and ICG–B–LM formulations.

Cellular uptake in EMT-6 tumor cells:

1×10^5 cells mL^{-1}EMT-6 murine mammary carcinoma cells were seeded in glass bottolm dishes (Matsunami Glass, Osaka, Japan) and incubated overnight at 37 °C. Cells were then co-cultured with ICG-B-LM or ICG-DSPE-LM nanocomposites (ICG = 12.5 μg mL^{-1}) for 12 h. After incubation, cells were washed three times with PBS and imaged under a fluorescence

microscope (BZ-X800, Keyence, Tokyo, Japan). Fluorescence images were acquired using CH3 channel at excitation wavelength of 633 nm and an emission range of 650-750 nm. Differential interference contrast (DIC) images were collected under identical conditions. The fluorescence and DIC channels were merged using a light microscopy system (BZ-X800) and fluorescence intensity was quantified using Keyence software. Regions of interest were selected around individual cells, and the mean fluorescence intensity was measured.

Temperature-dependent endocytosis in RAW 264.7 macrophages:

RAW 264.7 cells were seeded under the same conditions and incubated with ICG–B–LM nanocomposites for 1.5 h at 4 °C or 12 h at 37 °C to distinguish passive adsorption from active endocytosis. After washing with PBS, cells were imaged by Keyence as described above. Quantitative analysis of intracellular fluorescence intensity was performed using ImageJ. 3D confocal reconstruction further confirmed efficient internalization of ICG–B–LM at physiological temperature.

4.3.6 Direct observation of laser-induced cancer cell destruction

EMT-6 cells were seeded in glass-bottom dishes at a density of 3×10^5 cells mL^{-1} and cultured overnight to allow adhesion. The medium was then replaced with fresh medium containing either DSPE–LM or ICG-B-LM-DMX-αCD25 (final LM concentration: 300 μg mL^{-1}) and incubated for 12 h. After incubation, the medium was removed and the cells were washed three times with PBS to eliminate unbound nanocomposites. A customized laser-microscopy system was employed to directly visualize laser-triggered cell damage. An 808 nm continuous-wave near-infrared (NIR) diode laser (output power = 254 mW, corresponding to

~129 mW mm^{-2}) was coupled to an inverted microscope (IX73, Olympus, Tokyo, Japan). The laser beam was focused onto the cell monolayer through a 40× objective lens (NA = 0.95, UPLSAPO40X, Olympus), producing an irradiation spot approximately 50 μm in diameter. Laser exposure was performed at room temperature for 4 s. Real-time microscopic images before and during irradiation were captured using an electron-multiplying charge-coupled device (EMCCD) camera (DP80, Olympus).

4.3.7 *In vivo* bioimaging

All animal experiments were conducted in accordance with protocols approved by the Institutional Animal Care and Use Committee of the Japan Advanced Institute of Science and Technology (JAIST) (Approval No. 06–003). To investigate the tumor-targeting capability of ICG–B–LM nanocomposites, an orthotopic triple-negative breast cancer (TNBC) model was established by inoculating 4T1-luc cells into the left fourth mammary fat pad of female BALB/c mice (5 weeks old, average weight ≈ 18 g; Japan SLC, Hamamatsu, Japan). When the average tumor volume reached approximately 100 mm^3, the mice were intravenously administered with 200 μL of PBS (control) or 200 μL of PBS containing ICG–DSPE–LM or ICG–B–LM nanocomposites (ICG = 2 mg mL^{-1}, ≈20 mg kg^{-1}; LM = 3 mg mL^{-1}, ≈30 mg kg^{-1}). At predetermined time points (0, 5, 10, 17, and 24 h post-injection), the mice were euthanized, and the major organs (heart, lungs, liver, spleen, and kidneys) as well as tumor tissues were harvested for *ex vivo* NIR-FL imaging to assess biodistribution and tumor accumulation. FL signals were captured using an in vivo bioimaging system (VISQUE InVivo Smart-LF, Vieworks, Anyang, Republic of Korea) with a 3-s exposure time and an ICG filter (excitation: 740–790 nm, emission: 810–860 nm). Image acquisition and analysis were

performed using the CleVue software (Vieworks).

4.3.8 *In Vivo* anticancer therapy

In vivo anticancer therapy was performed on orthotopic 4T1-Luc tumor-bearing BALB/c mice (female, 5 weeks old, average weight 15–20 g; Japan SLC, Hamamatsu, Japan). Orthotopic triple-negative breast cancer (TNBC) models were generated by injecting a 1:1 mixture of Matrigel® (Corning, NY, USA) and PBS containing 1.7×10^7 4T1-Luc cells into the left fourth mammary fat pad. When tumors reached approximately 100 mm^3, mice were intravenously administered 200 µL of one of the following formulations: PBS (control), DSPE–PEG–LM (LM = 3 mg mL^{-1}, ≈ 30 mg kg^{-1}), DMXAA (1 mg mL^{-1}, ≈ 10 mg kg^{-1}), anti-CD25 (1 mg mL^{-1}, ≈ 10 mg kg^{-1}), or ICG–B–LM–DMX–αCD25 (LM = 3 mg mL^{-1}, ≈ 30 mg kg^{-1}; DMXAA = 1 mg mL^{-1}, ≈ 10 mg kg^{-1}; αCD25 = 1 mg mL^{-1}, ≈ 10 mg kg^{-1}).

For laser-treated groups, Orthotopic 4T1 tumors were irradiated with an 808 nm NIR laser (600 mW, ≈30.6 mW mm^{-2}) for 5 min at 24 h post-intravenous injection, and the treatment was repeated every other day for two sessions. The surface temperature of the tumor region was monitored in real time using an infrared thermal imaging camera (i7; FLIR, Nashua, NH, USA) during laser irradiation. Tumor growth and body weight were recorded every two days. Tumor volume (V) was calculated as $V = L \times W^2 / 2$, where L and W represent tumor length and width, respectively. Mice were euthanized when tumor volume exceeded 1,800 mm^3 according to the JAIST IACUC guidelines.

4.3.9 In Vivo antimetastatic therapy evaluation

To further assess the antimetastatic potential of the formulations, a secondary lung metastasis model was established using the treated mice from the primary anticancer study.

Following one treatment cycle of the above therapeutic regimen, mice were intravenously injected with 4T1-Luc cells (2×10^5 cells per mouse) to induce pulmonary metastasis.

For laser-treated groups, tumors were irradiated 24 h post-injection with an 808 nm laser (1.0 W cm^{-2}, 5 min). After the metastatic progression period, mice were euthanized, and the lungs were collected, imaged, and weighed to evaluate metastatic burden. Visible metastatic nodules on the lung surface were counted manually by visual inspection, and representative photographs were taken for documentation. Lung samples were subsequently fixed in 4% paraformaldehyde and subjected to hematoxylin and eosin (H&E) staining for histopathological evaluation, as described in Section 4.1.9

4.3.10 qPCR assay

Female 4T1 tumor-bearing BALB/cCrSlc mice (approximately 7 weeks old, n = 3 per group, average body weight ≈ 18 g, average tumor volume ≈ 200 mm^3; Japan SLC, Hamamatsu, Japan) were euthanized 24 h after intravenous administration of the respective formulations, as described in the *in vivo* anticancer therapy section. Tumor tissues were excised, immediately homogenized using a handheld tissue homogenizer (Thermo Fisher Scientific, Waltham, MA, USA), and processed for quantitative real-time PCR (qPCR) analysis. qPCR was performed on a QuantStudio™ 1 Real-Time PCR System (Thermo Fisher Scientific) using TaqMan™ chemistry to quantify the relative mRNA expression of **IFN-γ**, **TNF-α**, **Ly6g**, **ADGRE1**, **NCR1**, **CD19**, and **CD3**. Gene-specific primer–probe sets (Thermo Fisher Scientific) used in this study are listed in **Table 11.** Endogenous control was determined using the TaqMan™ Array Mouse Endogenous Control Plate 96-well (Thermo Fisher Scientific). GAPDH served as the internal reference. Reactions were run in triplicate and thermal cycling conditions were

as follows: 50 °C for 2 min (AmpErase UNG activation), 95 °C for 2 min (AmpliTaq Gold DNA polymerase activation), followed by 40 cycles of 95 °C for 1 s (denaturation), and 60 °C for 20 s (annealing and extension). PCR efficiency was determined by running 10-fold serial dilutions of the test genes and endogenous control standards, with percentage efficiency ranging between 90% and 100%. The results were analyzed and presented as fold change (log_{10} relative quantification) relative to the control group.

Table 11.TaqManTM Primers for qPCR.

Target	Assay ID	Gene Symbol	Source
STING	Mm01158117_m1	Tmem173	Thermo Fisher Scientific
TBK1	Mm00447775_m1	Tbk1	Thermo Fisher Scientific
TGF-β	Mm01178820_m1	Tgfb1	Thermo Fisher Scientific
IFN-β	Mm00439552_s1	Ifnb1	Thermo Fisher Scientific
CD8a	Mm01182107_g1	Cd8a	Thermo Fisher Scientific
Foxp3	Mm00475162_m1	Foxp3	Thermo Fisher Scientific
CD3	Mm00442746_m1	Cd3d	Thermo Fisher Scientific
CD19	Mm00515420_m1	Cd19	Thermo Fisher Scientific
NKp46	Mm01337324_g1	Ncr1	Thermo Fisher Scientific
IFN-γ	Mm01168134_m1	Ifng	Thermo Fisher Scientific
TNF-α	Mm00443258_m1	Tnf	Thermo Fisher Scientific
GAPDH	Mm99999915_g1	Gapdh	Thermo Fisher Scientific

4.3.11 Hematoxylin–Eosin (H&E) and Immunohistochemical (IHC) analyses

Female 4T1 tumor-bearing BALB/cCrSlc mice (approximately 7 weeks old, n = 4 per group, average body weight ≈ 18 g, average tumor volume ≈ 200 mm^3; Japan SLC, Hamamatsu, Japan) were euthanized one day after intravenous administration of the respective formulations and laser irradiation. Tumor tissues from each treatment group were collected for histological and immunohistochemical analyses. In addition, the major organs—including the heart, liver, kidneys, spleen, and lungs—were excised, fixed in 4% paraformaldehyde, and submitted for H&E staining to evaluate the systemic biosafety of the nanohybrids. IHC analysis was performed by the Biopathology Institute Co. Ltd. (Oita, Japan) according to standard protocols. Briefly, primary tumors were surgically excised, fixed in 10% formalin, processed for paraffin embedding, and sectioned into 3–4 μm slices. After incubation with the primary antibodies (Table 12), the sections were stained with H&E and examined under a light microscope (IX73). Positively stained areas within the tumor tissues were analyzed using a light microscope (BZ-X800, Keyence,) and the hybrid cell and microcell count software (Keyence). The color development in 10 independent regions of interest was quantified for each treated tumor tissue.

Table 12. Antibodies used in the IHC staining.

Antibody	Type	Source	Catalog No.	Application
F4/80	Mouse Monoclonal	BMA Biomedicals	T-2028	IHC (1:50)
CD3	Rabbit Monoclonal	Abcam	ab16669	IHC (1:100)

Antibody	Type	Source	Catalog No.	Application
CD19	Rabbit Polyclonal	Bioss	bs-0079R	IHC (1:100)
CXCR4	Goat Polyclonal	Abcam	ab1670	IHC (1:100)
NKp46	Rabbit Polyclonal	Affinity Biosciences	DF7599	IHC (1:100)
Caspase-3	Rabbit Polyclonal	Cell Signaling Technology	9661S	IHC (1:100)
TNF-α	Rabbit Polyclonal	Abcam	ab6671	IHC (1:100)
CD8	Rabit Monoclonal	Cell Signaling Technology	S7100	IHC (1:200)
CD25	Rabit	Cell Signaling	98941	IHC (1:100)
CD11c	Rabit Polyclonal	Protein Tech	17342-1-AP	IHC (1:200)
Anti-digoxigenin-peroxidase	Sheep Polyclonal	Merck Millipore	S7100	Tunel

4.3.12 Blood tests

The complete blood count (CBC) of mice was obtained using a blood cell counting machine (Microsemi LC 712; Horiba Medical, Japan). The biochemical parameters were

investigated by Japan SLC and Oriental Yeast Co. (Tokyo, Japan). Female BALB/c mice (6 weeks old, n = 6, average weight: 18 g; Japan SLC) were i.v. injected in the tail vein with 200 μL of B–LM–DMX–αCD25 (LM at 3 mg mL^{-1}, ≈30 mg kg^{-1}; DMXAA at 1 mg mL^{-1}, ≈10 mg kg^{-1}; anti-CD25 at 1 mg mL^{-1}, ≈10 mg kg^{-1}) or 200 μL of PBS as a control. Blood samples were collected from the inferior vena cava 7 d post-injection for analysis.

4.3.13 Statistical analyses

All experiments were performed in triplicate and independently repeated at least three times. Quantitative data are expressed as the mean ± standard deviation (SD) or standard error of the mean (SEM), as indicated. Statistical analyses were conducted using Student's two-tailed *t*-test or one-way analysis of variance (ANOVA) followed by Tukey's post hoc test, where appropriate. Survival data were analyzed using the log-rank (Mantel–Cox) test. All statistical analyses were performed using GraphPad Prism software (version 9.4.0; GraphPad Software, Boston, MA, USA). A p-value < 0.05 was considered statistically significant.

4.4 Results and discussion

4.4.1 Characterization of B–LM–DMXAA–αCD25 nanoplatform

The morphology and surface modification of liquid metal (LM) nanoparticles were systematically characterized. As shown in Figure 4.1, pristine LM exhibited severe aggregation owing to its high surface tension and absence of surface stabilization. After PEGylation with DSPE–PEG, the resulting DSPE–LM displayed improved dispersion but still showed aggregation with irregular spherical morphology, suggesting insufficient structural stability. In contrast, biomimetic modification with blood-derived components yielded B–LM

nanoparticles exhibiting a distinctive red color and uniform, well-dispersed morphology. The TEM image of B–LM revealed a clear core–shell architecture, confirming the presence of a biomimetic membrane coating on the LM surface, which demonstrates the successful construction of a biologically camouflaged nanoplatform.

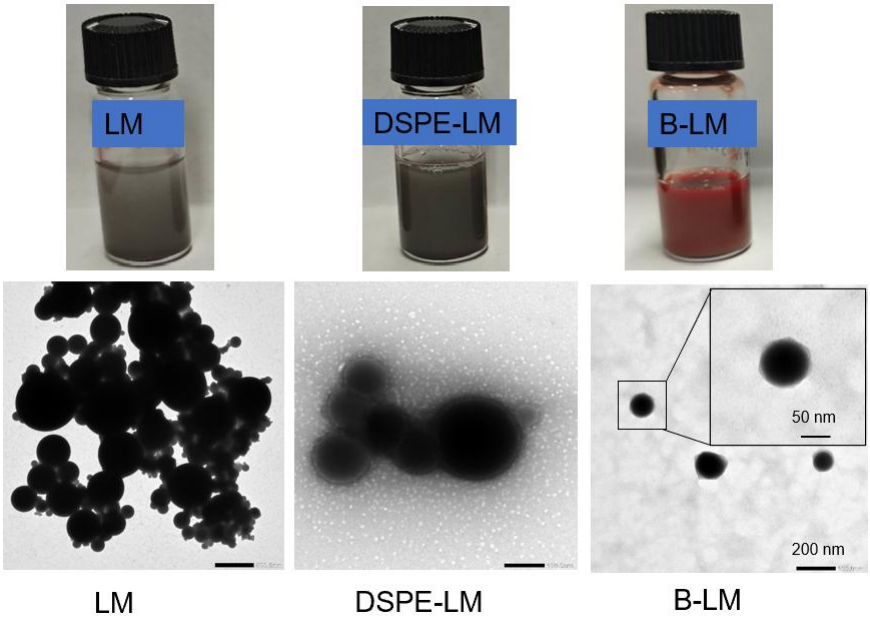

Figure 4.1 Visual and TEM characterization of LM, DSPE–LM, and B–LM.

The hydrodynamic size distribution (Figure 4.2A) revealed that both B–LM–DMXAA (~155 nm) and B–LM–DMXAA–αCD25 (~171 nm) maintained nanoscale dimensions with narrow polydispersity, confirming excellent colloidal stability. The slight increase in hydrodynamic diameter (~17 nm) after αCD25 conjugation further indicated the successful surface modification of B–LM–DMXAA with the antibody. UV–vis–NIR absorption spectra (Figure 4.2B) exhibited characteristic absorption peaks of both Blood-LM and DMXAA, validating the successful co-assembly of all components. The broad absorption of B–LM–DMXAA–αCD25 in the near-infrared region suggests excellent photothermal conversion

capability, which is beneficial for subsequent light-triggered immunotherapy.

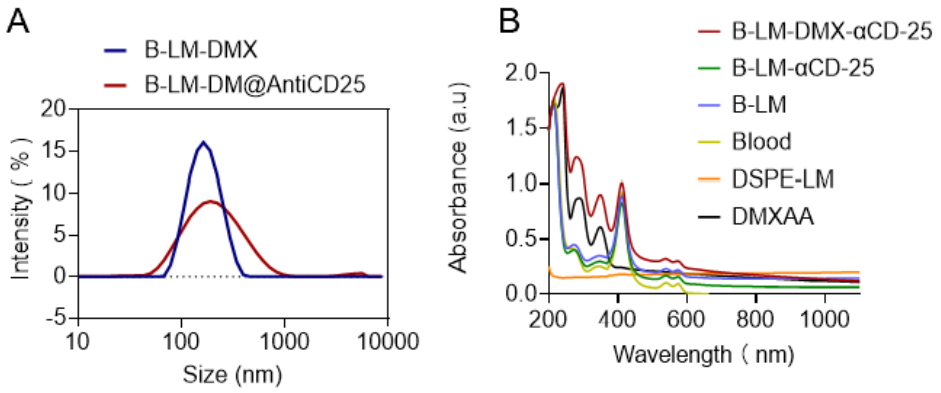

Figure 4.2 Characterization of the size and optical features of B–LM–DMX–αCD25 nanoplatform. A) Dynamic light scattering (DLS) size distribution of B–LM-DMX and B–LM-DMX-αCD25 Measurement of the average size of the nanocomposites on days 7. B) UV–vis–NIR absorbance spectra of PBS suspension of B–LM-DMX-αCD25 (LM concentration = 60 μg/Ml, DMXAA = 20 μg/mL, αCD25 = 20 μg/mL).

Although DMXAA exhibits potent immunostimulatory activity within the tumor microenvironment, its strong hydrophobicity severely limits systemic administration, and most reported antitumor effects have been achieved only via intratumoral injection. In this study, DMXAA was encapsulated within a biomimetic nanoplatform to enhance its therapeutic efficiency and to integrate the STING agonist with photothermal (PTT) therapy. The loading efficiency of DMXAA was determined by UV–vis spectrophotometry and calculated to be 95.65 ± 3.6%, further confirming the successful encapsulation of the hydrophobic STING agonist within the blood-engineered nanoparticles, thereby ensuring a high drug-loading capacity. Upon laser irradiation, B–LM–DMXAA–αCD25 showed a rapid and sustained release of DMXAA, reaching nearly 90% within 12 min (Figure 4.3). This NIR-induced burst release is attributed to the photothermal heating of the LM core, which facilitates on-demand drug diffusion. Collectively, these results confirm that the B–LM–DMXAA–αCD25 platform

integrates excellent structural stability, high drug-loading efficiency, and laser-responsive release behavior, providing a solid foundation for subsequent in vitro and in vivo photothermal–immunotherapeutic studies.

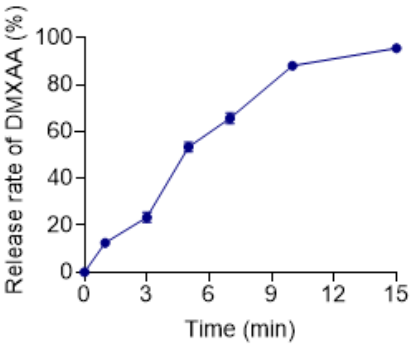

Figure 4.3 DMXAA release profile from laser-induced B–LM-DMX-αCD25. Data are presented as means ± standard error of the mean (SEM) (n = 3; independent tests).

The photothermal conversion properties of the B–LM–DMXAA–αCD25 nanocomposites were systematically investigated under 808 nm laser irradiation at various power densities and LM concentrations. As shown in Figure 3A, the temperature of the suspensions increased in both a power- and concentration-dependent manner, whereas negligible heating was observed for Milli-Q water. At an LM concentration of 500 μg mL^{-1}, the temperature rapidly rose to approximately 70 °C within 5 min under 1.5 W irradiation, highlighting the excellent light-to-heat conversion capability of the nanoplatform. The corresponding infrared thermographic images (Figure 3B) further corroborated this finding, displaying a clear temperature transition from blue to red as laser power and LM concentration increased.

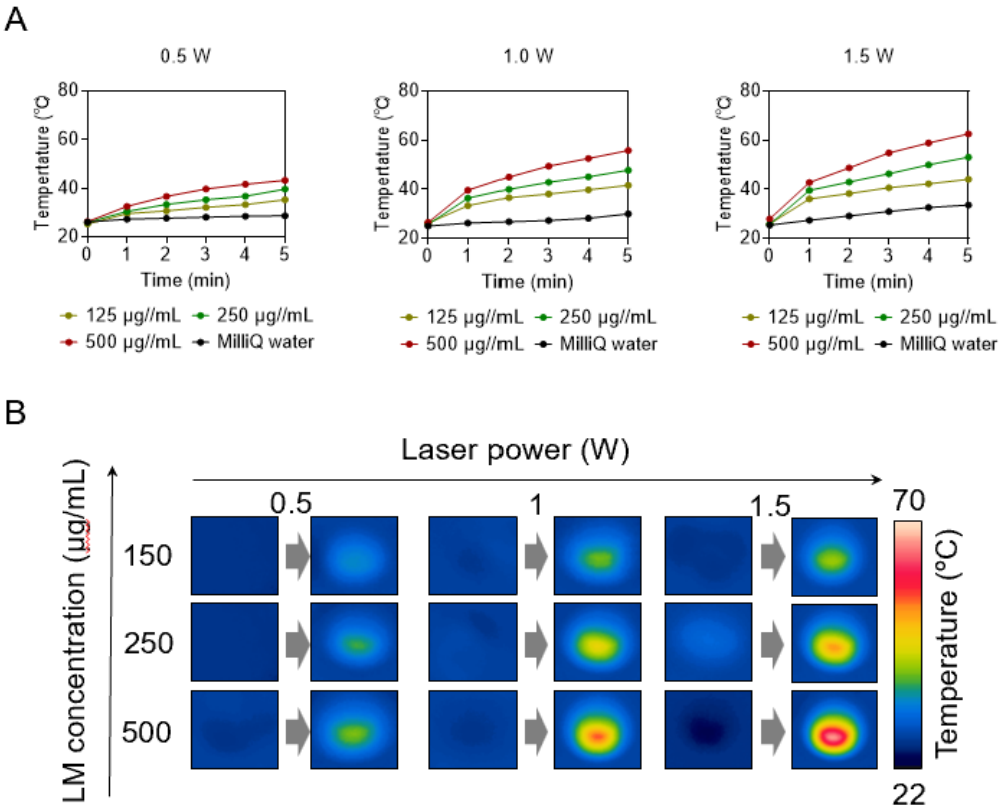

Figure 4.4 Photothermal activity of B–LM-DMX-αCD25 nanocomposites. A) Photothermal heating curves, and B) corresponding thermographic images after 5 min of laser irradiation in Milli-Q water (control) and B–LM-DMX-αCD25 at different LM concentrations by 808 nm laser irradiation at 0.5 W (ca. 25.5 mW/mm2), 1.0 W (ca. 51 mW/mm2), or 1.5 W (ca. 76.5 mW/mm2) power.

The optical stability of the nanocomposites was next evaluated. The UV–vis–NIR absorption spectra recorded before and after laser exposure (Figure 4.5A) exhibited no significant spectral shifts or intensity attenuation, indicating robust photostability and structural integrity of the LM-based nanocomposites. Furthermore, the heating–cooling cycling test (Figure 4.5B) revealed highly reproducible thermal curves across multiple on/off cycles, confirming excellent photothermal durability under repetitive irradiation.

Together, these results demonstrate that B–LM–DMXAA–αCD25 nanocomposites possess exceptional and tunable photothermal performance, exceptional optical stability, and reliable thermal endurance, thereby providing a robust foundation for their use in

photothermal–immunotherapeutic applications.

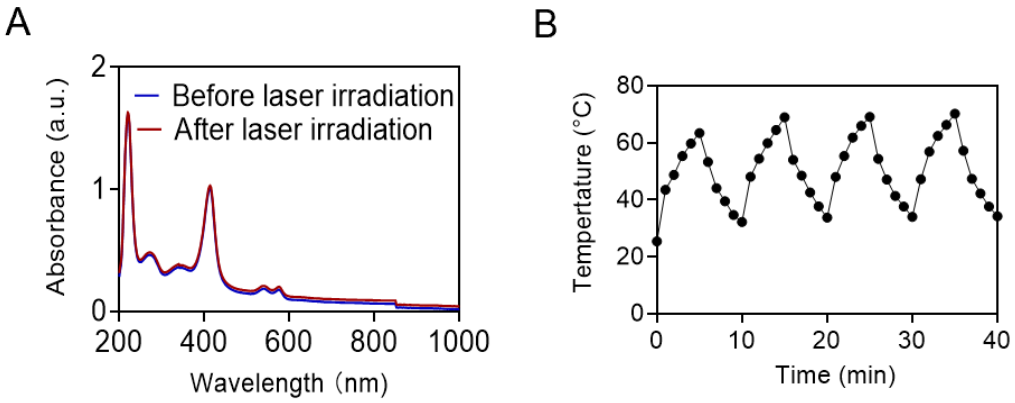

Figure 4.5 Optical absorption and photothermal durability of LM nanoplatforms. A) UV–vis–NIR absorbance spectra of Lacto–LM before and after laser irradiation for 5 min at 1.5 W (ca. 76.5 mW/mm2). B) Stability testing B–LM-DMX-αCD25 under repetitive photothermal heating and natural cooling cycles by 808 nm laser irradiation at 1.5 W (ca. 76.5 mW/mm2). LM concentration: 500 mg/mL in 0.5 mL PBS.

4.4.2 Laser-induced cytotoxicity of B–LM–DMXAA–αCD25 nanocomposites

The cytotoxicity of the B–LM–DMXAA–αCD25 nanocomposites was first evaluated in EMT-6 tumor cells and normal MRC-5 fibroblasts without laser irradiation. As shown in Figure 4.6A, both cell lines maintained high viability after 24 h of incubation with the nanocomposites at LM concentrations up to 500 μg mL^{-1}, indicating negligible cytotoxicity. In contrast, upon 808 nm laser irradiation (1.0 W, approximately 30.6 mW/mm^2), cell viability decreased in a concentration-dependent manner (Figure 4.6B). Notably, laser-activated B–LM–DMXAA–αCD25 exhibited preferential cytotoxicity toward EMT-6 cancer cells compared to normal MRC5 cells, indicating favorable therapeutic selectivity. This differential response can be attributed to fundamental differences in cellular physiology between malignant and normal cells. Cancer cells typically exhibit higher metabolic activity, reduced heat shock protein expression, and accelerated proliferation rates, rendering them more susceptible to heat-

induced DNA and protein damage. In contrast, normal cells maintain elevated heat shock protein levels, which provide enhanced thermal protection through mechanisms including protein refolding, macromolecular stabilization, and apoptosis inhibition during hyperthermia exposure[43-44] This inherent selectivity represents a significant advantage for clinical translation, as it may minimize collateral damage to healthy tissues during treatment.

Microscopic imaging further provided visual evidence of laser-induced cell destruction (Figure 4.6C). Upon laser exposure, rapid bubble formation and membrane disruption were observed in the irradiated region, confirming the efficient photothermal conversion of the B–LM–DMXAA–αCD25 nanocomposites and their ability to induce acute and potent thermal damage at the cellular level. Together, these results demonstrate that B–LM–DMXAA–αCD25 exhibits excellent biocompatibility under non-irradiated conditions and potent photothermal cytotoxicity under NIR laser exposure, enabling precise, controllable, and tumor-selective ablation for subsequent immunotherapeutic applications.

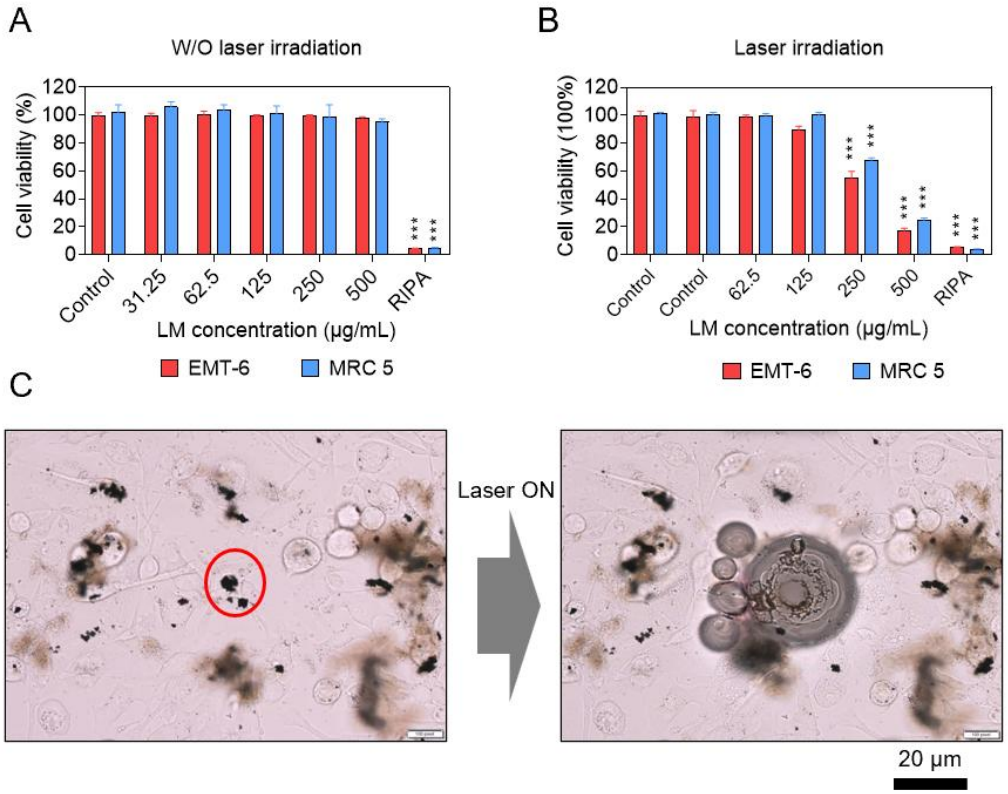

Figure 4.6 Laser-induced cytotoxicity of B–LM nanocomposites. A) Viability of EMT-6 and MRC5 cells after coculturing for 24 h with B–LM-DMX-αCD25 at various LM concentrations or radioimmunoprecipitation assay (RIPA) buffer. B) Cytotoxicity assay with EMT-6 and MRC5 cells after B–LM at various LM concentrations for 24 h and laser irradiation (1.0 W [ca. 51 mW/mm2]) for 5 min. Data are presented as mean ± SEM (n = 5; biologically independent tests). ***, $p < 0.001$, versus control without nanoparticles by Student's t-test. C) Photothermal cytotoxicity of B–LM–DMX–αCD25 nanocomposites. EMT-6 cells were incubated with B–LM–DMX–αCD25 for 12 h, followed by irradiation with an 808 nm near-infrared (NIR) laser (564 mW, ≈287 mW mm^{-2}). The irradiation area and focal position were indicated by a red circular region in the captured images, corresponding to the laser-exposed zone.

4.4.3 Enhanced cellular internalization of blood-biomimetic LM nanocomposites via active endocytic pathways

The cellular uptake behavior of ICG–B–LM–DMXAA–αCD25 nanocomposites was investigated to evaluate the effect of the blood-biomimetic coating on intracellular accumulation. As shown in Figure 4.7A, the nanocomposites displayed strong fluorescence emission centered around 810 nm under 750 nm excitation, confirming the successful

integration of ICG within the LM matrix and its stability in the near-infrared region.

To assess cellular uptake, EMT-6 cells were incubated with ICG–B–LM or ICG–DSPE–LM for 12 h. As shown in Figure 4.7B, pronounced intracellular fluorescence was observed in the ICG–B–LM group, whereas minimal signal was detected in the ICG–DSPE–LM group. Quantitative analysis (Figure 4.7C) revealed that the fluorescence intensity in the ICG–B–LM–treated cells was significantly higher than that in the DSPE–LM group, indicating that the blood-derived biomimetic interface markedly enhanced nanoparticle internalization. The 3D confocal reconstruction (Figure 4.7D) further verified the strong intracellular localization of B–LM nanocomposites within tumor cells.

To elucidate the mechanism of cellular uptake, Raw 264.7 macrophages were incubated with B–LM at different temperatures. As shown in Figure 4.7E, significantly weaker fluorescence was observed at 4 °C, whereas robust intracellular signals were detected after 12 h of incubation at 37 °C, suggesting an active, energy-dependent endocytic process. Quantitative fluorescence analysis (Figure 4.7F) corroborated these findings, showing a significant increase in mean intensity at physiological temperature. The 3D fluorescence imaging (Figure 4.7G) confirmed extensive intracellular distribution and endosomal accumulation. Collectively, these results demonstrate that the whole-blood–camouflaged LM nanoplatform possesses enhanced cell–nanoparticle interactions and active uptake capacity, leading to efficient intracellular accumulation—a prerequisite for subsequent photothermal and immune activation processes.

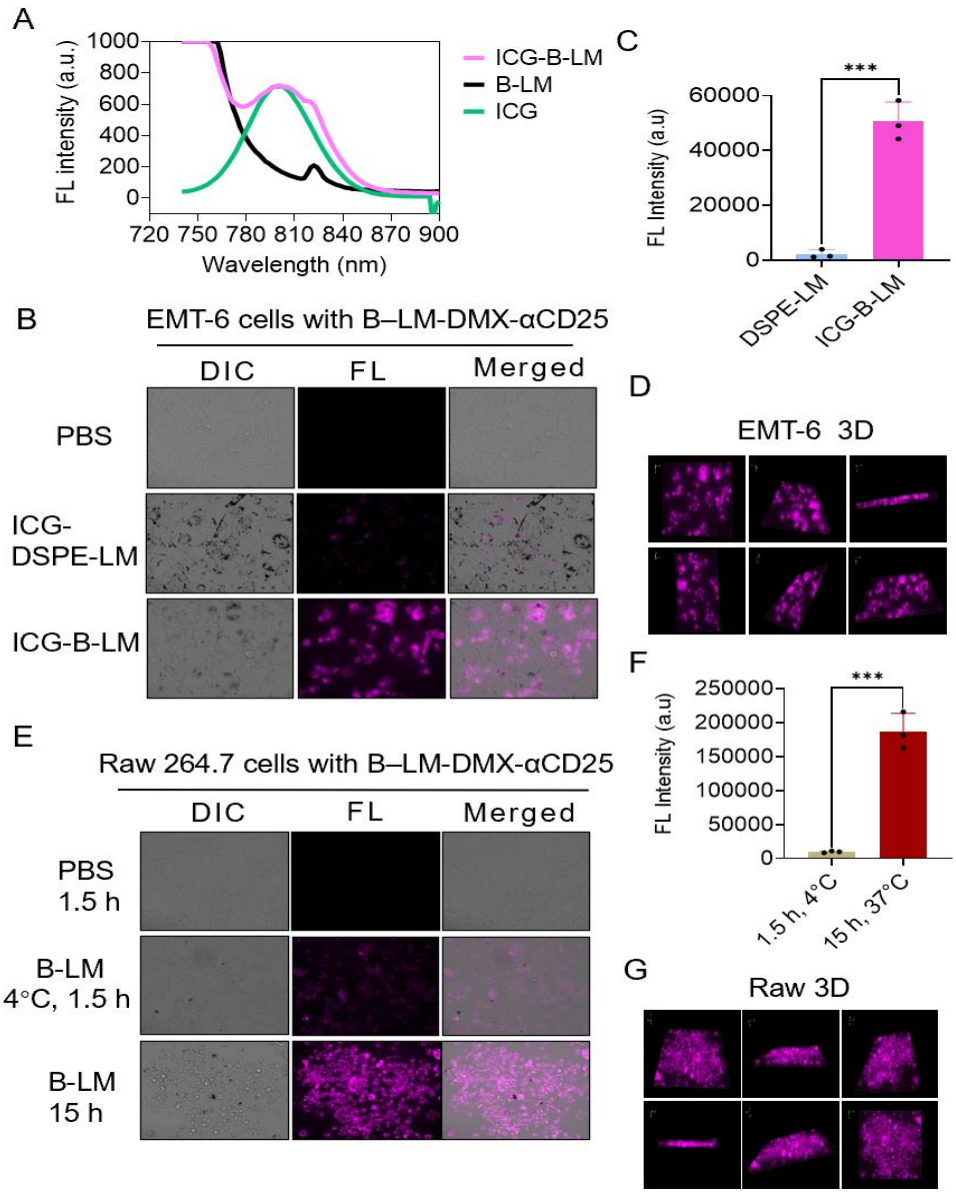

Figure 4.7 Intracellular distribution of indocyanine green (ICG) – B–LM nanocomposites. A) Fluorescence (FL) spectra of ICG– B–LM (LM concentration = 300 µg/mL and ICG concentration = 12.5 µg/mL) at 750 nm excitation wavelength. B) Near-infrared (NIR) FL bioimaging of EMT-6 cells after coculturing with ICG–B–LM or ICG–DSPE–LM for 12 h. Pink and black particles represent B–LM. C) Quantitative analysis of intracellular ICG fluorescence intensity at 12 hours. Data represent mean ± SD (n = 3). ***$p < 0.001$ compared to DSPE-LM groups. D) Three-dimensional (3D) images of EMT-6 cells after coculturing with ICG–B–LM for 12 h E) Near-infrared (NIR) FL bioimaging of Raw 264.7 cells after coculturing with ICG–B–LM for 1.5h at 4 °C or 12 h at 37 °C. F) Quantitative analysis of intracellular ICG fluorescence intensity. Data represent mean ± SD (n = 3). ***$p < 0.001$ compared to group incubated for 1.5h at 4 °C G) Three-dimensional (3D) images of Raw 264.7 cells after coculturing with ICG–B–LM for 15 h at 37 °C

The biodistribution and tumor-targeting performance of the B–LM–DMXAA–αCD25 nanocomposites were assessed by near-infrared (NIR) fluorescence imaging in orthotopic 4T1 tumor–bearing mice. As shown in Figure 6, the fluorescence signal in the ICG–B–LM group gradually accumulated at the tumor site and reached its peak intensity at approximately 17–24 h post-injection, while no fluorescence was detected in the PBS group. In contrast, the ICG–DSPE–LM group exhibited a more transient and nonspecific distribution, with most of the fluorescence confined to the liver region, indicating rapid clearance by the reticuloendothelial system (RES). Ex vivo imaging of the dissected organs and tumors further corroborated these findings, revealing markedly stronger fluorescence intensity in the tumor tissues of the ICG–B–LM group compared with other groups. The relatively lower signal observed in the liver and spleen further suggests that the blood-biomimetic coating effectively reduced opsonization and immune clearance, thereby facilitating prolonged circulation and enhanced tumor accumulation through both EPR (enhanced permeability and retention) and biomimetic immune evasion effects. Collectively, these results demonstrate that the B–LM–DMXAA–αCD25 nanoplatform exhibits excellent in vivo stability and tumor-homing capability, ensuring efficient delivery of therapeutic payloads to the tumor microenvironment—an essential prerequisite for the subsequent photothermal–immunotherapeutic cascade.

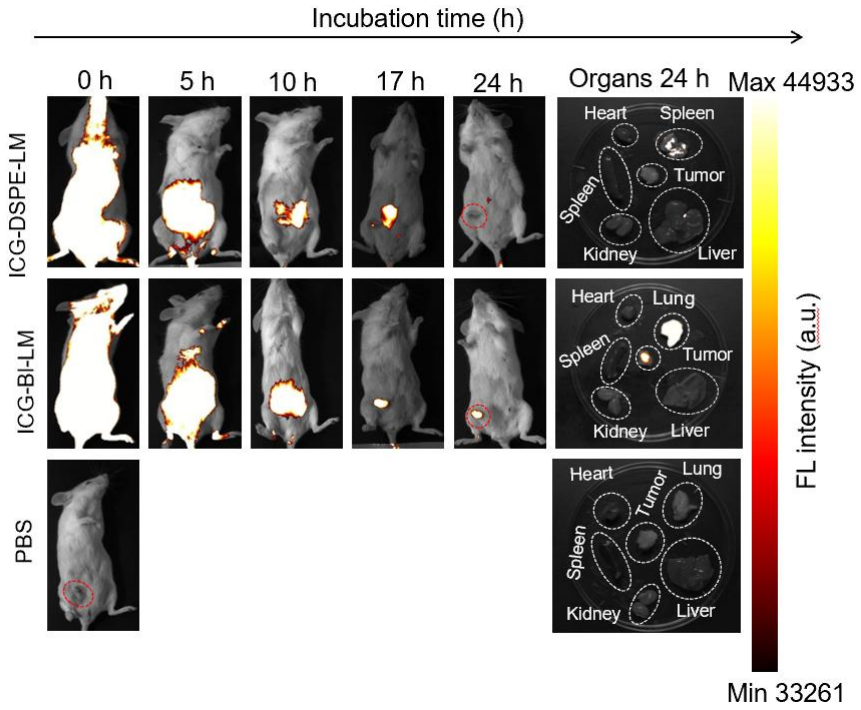

Figure 4.8 Tumor targeting of B–LM-DMX-αCD25 nanocomposites. Near-infrared (NIR) fluorescence bioimaging of the whole body, excised tumors, and major organs was performed in orthotopic 4T1 tumor–bearing mice following intravenous injection of ICG–B–LM–DMXAA–αCD25, PBS, or ICG–DSPE–PEG–LM via the tail vein. The doses of ICG and LM were 20 mg kg^{-1} and 30 mg kg^{-1}, respectively.

4.4.4 In Vivo photothermal performance of B–LM–DMXAA–αCD25 nanocomposites

To evaluate the in vivo photothermal conversion performance, orthotopic 4T1 tumor–bearing mice were intravenously administered with different formulations followed by 808 nm laser irradiation. As illustrated in Figure 4.9A, the tumor temperature in the B–LM–DMXAA–αCD25–treated group rapidly and markedly increased upon laser exposure, demonstrating efficient photothermal conversion. In contrast, only negligible temperature elevations were observed in the PBS, DSPE–LM, αCD25, and DMXAA groups, likely due to the limited optical absorption of endogenous biological components in tissue.

Quantitative thermal profiles (Figure 4.9B) revealed that the surface temperature of

tumors treated with B–LM–DMXAA–αCD25 rose sharply to nearly 58 °C within 5 min of irradiation, significantly higher than those of all control groups ($p < 0.001$). In contrast, tumors in the PBS and DSPE–LM groups remained below 40 °C, which is insufficient for effective thermal ablation. The remarkable temperature elevation in the B–LM–DMXAA–αCD25 group can be attributed to the efficient NIR absorption and superior photothermal conversion of the liquid-metal core, coupled with enhanced tumor accumulation facilitated by the whole-blood biomimetic coating.

These findings confirm that the B–LM–DMXAA–αCD25 nanoplatform achieves potent in vivo photothermal heating under clinically relevant laser power densities, enabling precise and efficient thermal ablation of tumor tissue while minimizing off-target heating—providing a strong foundation for subsequent immunotherapeutic activation.

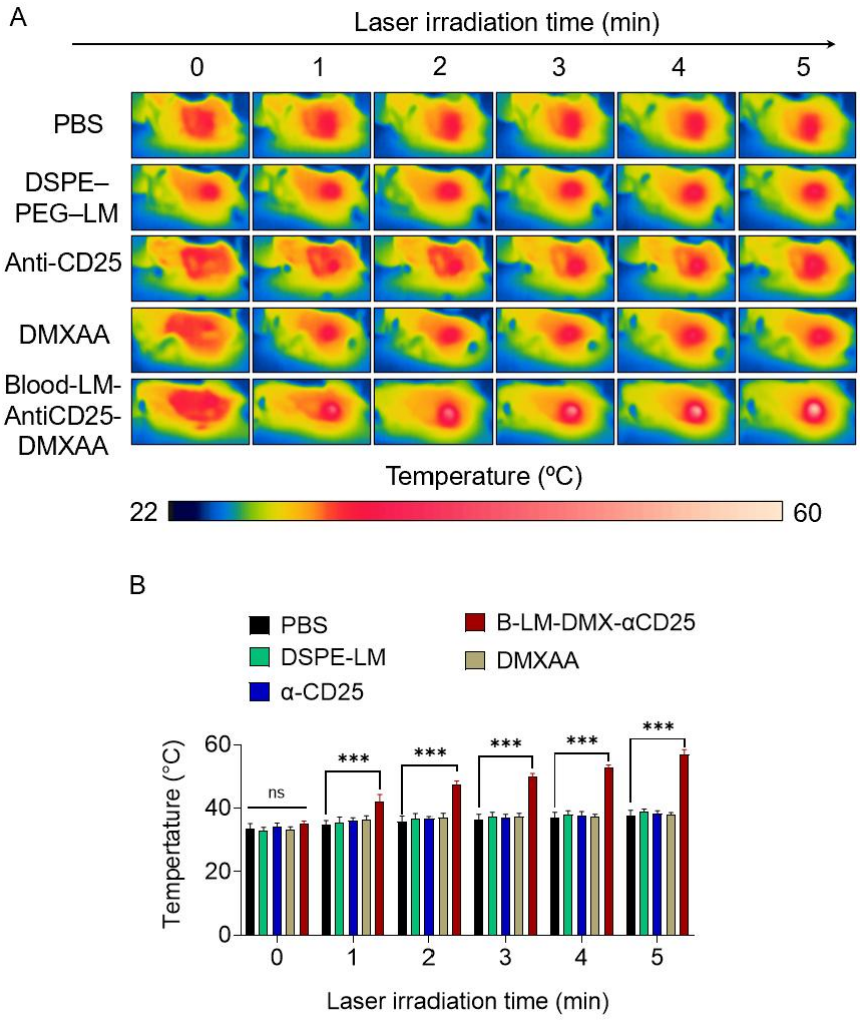

Figure 4.9 In vivo photothermal performance of B–LM–DMXAA–αCD25 under NIR irradiation. A) Infrared thermal images of orthotopic 4T1 tumor–bearing mice recorded during 808 nm laser irradiation (1.0 W cm^{-2}, 5 min) at 24 h post intravenous injection of different formulations B) Corresponding temperature changes at tumor sites, showing that B–LM–DMXAA–αCD25 induced a rapid and significant temperature increase compared with other groups. Data are presented as mean ± SEM (n = 5, ***p < 0.001).

4.4.5 In vivo therapeutic efficacy of the Blood-LM-DMX-αCD25

To evaluate the in vivo therapeutic efficacy of the Blood-LM-DMX-αCD25 nanoplatform, orthotopic 4T1 breast-tumor-bearing mice were established and intravenously injected with various formulations followed by near-infrared (808 nm, 1.0 W ≈ 30.6 mW mm^{-2}, 5 min day^{-1}) irradiation (Figure 4.10A). As shown in Figure 4.10B, tumors in the PBS control group grew

rapidly, confirming the highly aggressive nature of the orthotopic 4T1 model. Treatment with DSPE-LM displayed no inhibitory effect on tumor growth, attributable to its limited photothermal conversion efficiency and absence of immune modulation. In contrast, administration of DMXAA or αCD25 alone resulted in significantly improved therapeutic efficacy, indicating that partial STING activation or Treg depletion can enhance antitumor immunity. However, Blood-LM-DMX-αCD25 exhibited the most pronounced inhibition of tumor growth compared with DSPE-DMXAA or DSPE-αCD25, underscoring the synergistic benefits of integrating both the STING agonist DMXAA and the Treg-targeting αCD25 antibody within a single nanoplatform. Furthermore, under laser irradiation, the B-LM-DMX-αCD25 + L group achieved complete tumor eradication throughout the observation period ($p < 0.001$ vs PBS + L), confirming a potent synergistic enhancement derived from the combined effects of photothermal ablation, STING-pathway activation, and Treg-mediated immune relief. Representative tumor photographs (Figure 4.10C) visually corroborate these findings. Upon laser irradiation, tumors treated with B-LM-DMX-αCD25 exhibited rapid regression and complete disappearance throughout the observation period. The absence of recurrence in the B-LM-DMX-αCD25 + L group highlights the potent and durable therapeutic efficacy of this multifunctional nanoplatform in combating the highly aggressive and refractory nature of TNBC. The superior therapeutic efficacy of B–LM–DMXAA–αCD25 can be attributed to the concerted action of its three functional modules. The liquid-metal core ensures efficient photothermal conversion, inducing localized ablation and immunogenic cell death. Concurrently, αCD25 selectively depletes intratumorally regulatory T cells, thereby releasing the immunological brakes on cytotoxic immunity. Meanwhile, DMXAA activates the STING

signaling pathway and promotes the uptake and cross-presentation of tumor-associated antigens (TAAs) generated from PTT-induced immunogenic cell death, ultimately amplifying antitumor immune responses. Collectively, these synergistic interactions establish a potent photothermal–immunological cooperation that enables rapid, complete, and durable tumor regression in TNBC.

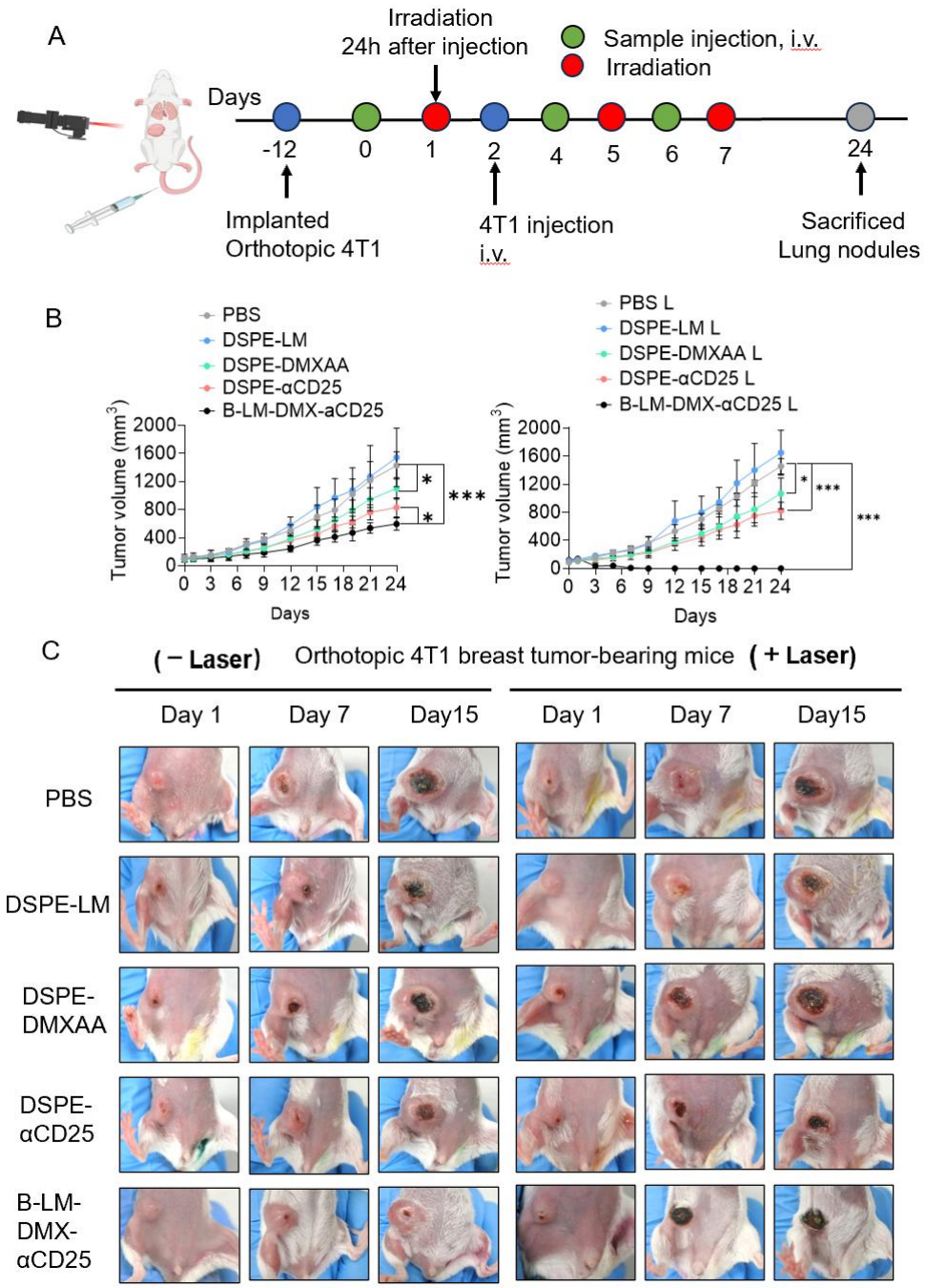

Figure 4.10 . In vivo therapeutic evaluation of B–LM–DMX–αCD25 nanocomposites under NIR laser irradiation. A) Schematic illustration of the in vivo treatment procedure. Tumor-bearing mice were intravenously injected with PBS, DSPE-LM, DSPE-DMXAA, DSPE-αCD25, or B-LM-DMX-αCD25, and laser irradiation (808 nm, 1.0 W ≈ 30.6 mW mm^{-2} , 5 min day^{-1} , four times in total) was applied 24 h after injection. B) Tumor-volume growth curves of mice treated with various formulations with (+ L) or without (– L) laser irradiation. Data are expressed as mean ± SEM (n = 4 biologically independent tests). *p < 0.05, **p < 0.01, ***p < 0.001, by one-way ANOVA. C) Representative photographs of orthotopic 4T1 tumor–bearing mice recorded on days 1, 7, and 15 after treatment, showing tumor progression under different therapeutic conditions (– Laser / + Laser).

Throughout the 21-day treatment period (Figure 4.11), the body weights of mice in the B–LM–DMXAA–αCD25 treatment groups remained stable, with no noticeable fluctuations or reductions compared to the PBS control. This finding indicates that the B–LM–DMXAA–αCD25 formulations possess biosafety and tolerability, demonstrating that the multifunctional nanocomposite can be safely applied during repeated photothermal–immunotherapy sessions

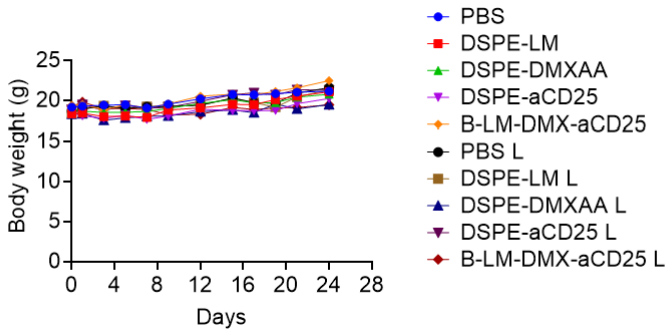

Figure 4.12 Body weight variations of 4T1 tumor–bearing mice during the 21-day treatment period following intravenous administration of different formulations with or without NIR laser irradiation (808 nm, 1.0 W cm^{-2}, 5 min per session). Data are presented as mean ± SD (n = 4).

4.4.6 In vivo inhibition of breast cancer lung metastasis

Clinically, triple-negative breast cancer (TNBC) is recognized as a highly aggressive and refractory malignancy, largely due to its profoundly immunosuppressive tumor microenvironment (TME). The lung represents one of the most common sites of distant dissemination in TNBC. Therefore, after confirming the potent therapeutic efficacy of B–LM–DMXAA–αCD25 in orthotopic 4T1 primary tumor models, we next sought to evaluate its ability to prevent distant metastasis. Specifically, we examined whether systemic administration of B–LM–DMXAA–αCD25 could effectively inhibit metastatic colonization in the lungs. To this end, after completing the first course of primary tumor treatment, mice were intravenously injected with 4T1 cells via the tail vein to establish an experimental pulmonary

metastasis model. This sequential design allowed evaluation of whether the systemic immune activation induced by the B–LM–DMX–αCD25 nanoplatform could effectively suppress secondary metastatic colonization in distant organs such as the lungs. As shown in Figure 4.13A, the lungs of mice treated with PBS or DSPE–LM exhibited numerous visible metastatic nodules, indicating extensive secondary metastasis. In contrast, mice treated with DSPE–DMXAA or DSPE–αCD25 alone exhibited a moderate reduction in metastatic burden, indicating that either STING activation or Treg depletion alone was insufficient to prevent systemic tumor dissemination. Remarkably, mice receiving B–LM–DMXAA–αCD25 with laser irradiation displayed nearly normal lung morphology with minimal residual nodules, demonstrating that the B–LM–DMXAA–αCD25–mediated photothermal–immunotherapy synergistically suppressed metastatic colonization.

Quantitative analysis (Figure 4.13B) revealed that the number of metastatic nodules in the B–LM–DMX–αCD25 + Laser group was significantly reduced compared with all other groups ($p < 0.001$). Consistent with these findings, this group also exhibited the lowest lung weights, which were nearly identical to those of healthy mice (Figure 4.13C). This finding clearly demonstrates that the therapeutic benefits of B–LM–DMXAA–αCD25 extend beyond local tumor ablation, effectively eliciting systemic antitumor immunity that prevents secondary tumor colonization and recurrence.

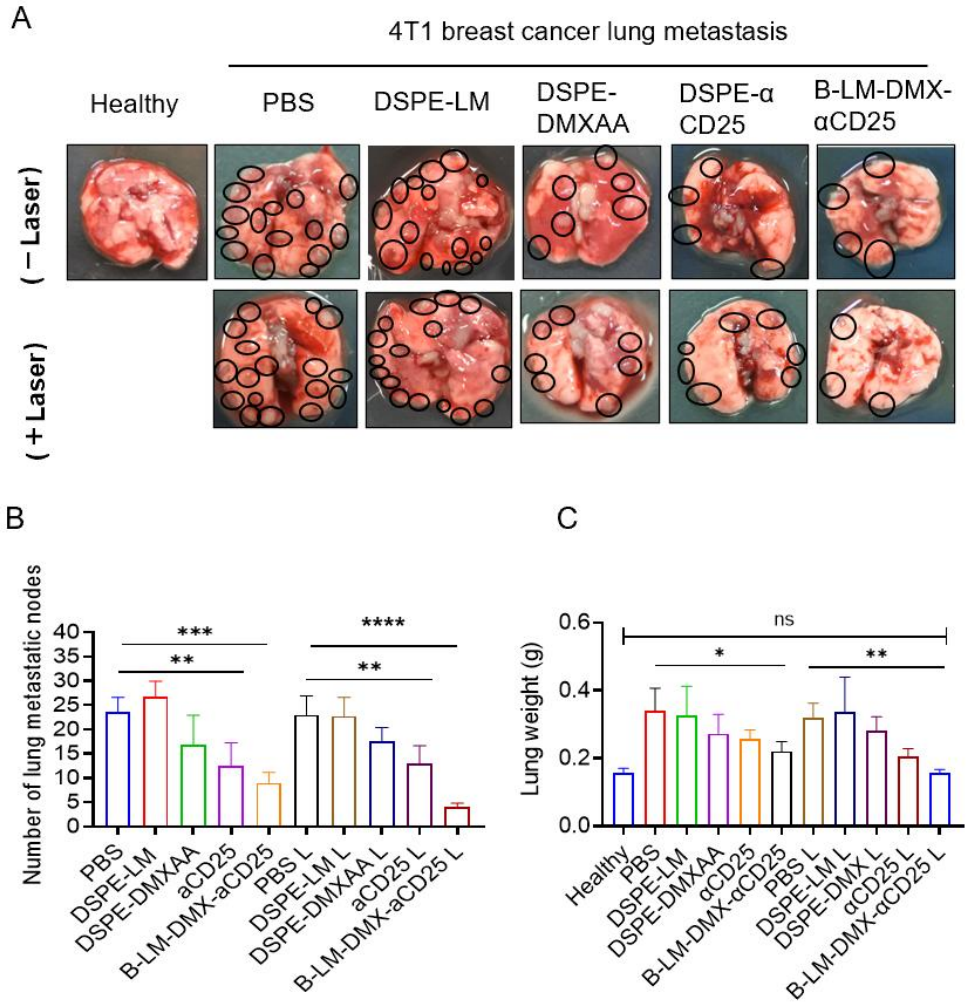

Figure 4.13 In vivo inhibition of 4T1 breast cancer metastasis by B–LM–DMX–αCD25 nanocomposites. A) Representative photographs of lungs collected from healthy mice and 4T1 tumor–bearing mice treated with PBS, DSPE-LM, DSPE-DMXAA, DSPE-αCD25, or B-LM-DMX-αCD25, with or without 808 nm laser irradiation after 24 days of treatment. (1.0 W ≈ 30.6 mW mm^{-2}, 5 min). Metastatic nodules are circled in black. B) Quantitative analysis of lung metastatic nodules in each group. C) Lung weights of healthy and treated mice. Data are presented as mean ± SEM (n = 4 biologically independent samples per group). Statistical significance was analyzed using one-way ANOVA. *p < 0.05, **p < 0.01, ***p < 0.001, ****p < 0.0001; ns, not significant. Laser-irradiated groups are denoted with " L".

4.4.7 Anticancer mechanism of B–LM–DMXAA–αCD25

Due to the profoundly immunosuppressive tumor microenvironment (TME), TNBC generally exhibits poor responsiveness to immune checkpoint blockade therapy. Pathological analyses have revealed that the level of Treg infiltration in TNBC tissues is typically higher

than that in other breast-cancer subtypes, contributing to immune evasion and therapeutic resistance. In this study, we rationally engineered a LM nanocomposite conjugated with anti-CD25 antibodies to selectively deplete intratumoral Tregs during photothermal therapy (PTT). The targeted elimination of this immunosuppressive subset effectively releases the immunological brake and reprograms the local TME toward an immune-active state. In the B–LM–DMXAA–αCD25–treated group, a marked reduction in Tregs, together with increased antigen-presenting cells (DCs and macrophages) and T lymphocytes, clearly demonstrates the alleviation of immune restraint and reversal of the immunosuppressive TME.

Following this, during the potent PTT process, extensive pyroptosis-like cell death and immunogenic cell death (ICD) occur concurrently, releasing abundant tumor-associated antigens (TAAs) and danger-associated molecular patterns (DAMPs) that provide strong immunogenic “fuel” for subsequent immune activation. Building upon this antigen availability, the encapsulated STING agonist DMXAA activates the STING–TBK1–IRF3 signaling pathway in antigen-presenting cells, inducing type-I interferon production, promoting dendritic-cell (DC) maturation, and enhancing cross-presentation to T cells.

A complete tumor-specific immune response requires the coordinated progression of three key steps: the release of tumor-associated antigens, the maturation of dendritic cells, and the efficient cross-presentation of these antigens to T cells, ultimately leading to the generation of tumor-specific cytotoxic lymphocytes. Therefore, to efficiently induce TAA-specific killing, we integrated DMXAA into the platform to activate a sufficient number of dendritic cells while antigen release occurs. Consistent with this design, the B–LM–DMXAA–αCD25 + Laser

group exhibited markedly enhanced antigen uptake and dendritic-cell maturation, leading to efficient priming of TAA-specific $CD8^+$ T cells.

This coordinated immune cascade—combining Treg depletion, PTT-induced ICD, and STING activation—not only converts the immunosuppressive TME into an immune-permissive niche but also establishes a self-amplifying antitumor state. Beyond the expansion of cytotoxic $CD8^+$ T cells, the type-I interferon–enriched milieu further augments NK-cell cytotoxicity and stimulates B-cell responses, together contributing to a robust systemic antitumor immunity.

Collectively, the B–LM–DMXAA–αCD25 nanocomposite achieves complete eradication of primary TNBC tumors under NIR laser irradiation while synergistically converting cold tumors into hot ones, thereby eliciting robust systemic antitumor immunity that effectively prevents lung metastasis and tumor recurrence.

4.5 Conclusion

In this study, we innovatively camouflaged liquid metal (LM) nanoparticles with whole blood components to construct a multifunctional platform for photothermal therapy (PTT). The resulting B–LM nanocomposites exhibited markedly improved aqueous dispersibility, biocompatibility, and immune evasion capability, thereby achieving enhanced accumulation and retention at the tumor site. To further enhance the performance, the conjugation of anti-CD25 antibodies and encapsulation of the STING agonist DMXAA endowed the system with dual immunomodulatory functions.

The engineered B–LM–DMXAA–αCD25 nanocomposites achieved potent photothermal ablation of primary TNBC tumors under NIR irradiation, while simultaneously reprogramming the Treg-dominated immunosuppressive tumor microenvironment through selective Treg depletion. The photothermal process induced robust immunogenic cell death (ICD) and the release of abundant tumor-associated antigens (TAAs). Concurrently, laser-triggered DMXAA release activated the STING–TBK1–IRF3 signaling pathway, promoting dendritic-cell maturation and antigen cross-presentation to naïve T cells, thus facilitating TAA-specific T-cell priming.

Collectively, our findings demonstrate that the combination of PTT with STING activation functions as an immunological “ignition signal,” transforming localized photothermal ablation into a durable systemic antitumor immune response. Moreover, the simultaneous Treg clearance synergistically amplifies immune activation, effectively converting the immunosuppressive cold TME into a hot, immune-active state. This work

highlights the great potential of B–LM–DMXAA–αCD25 nanocomposites for combating highly aggressive TNBC and provides an advanced strategy for integrating nanotechnology with immunotherapy to achieve effective multimodal cancer treatment.

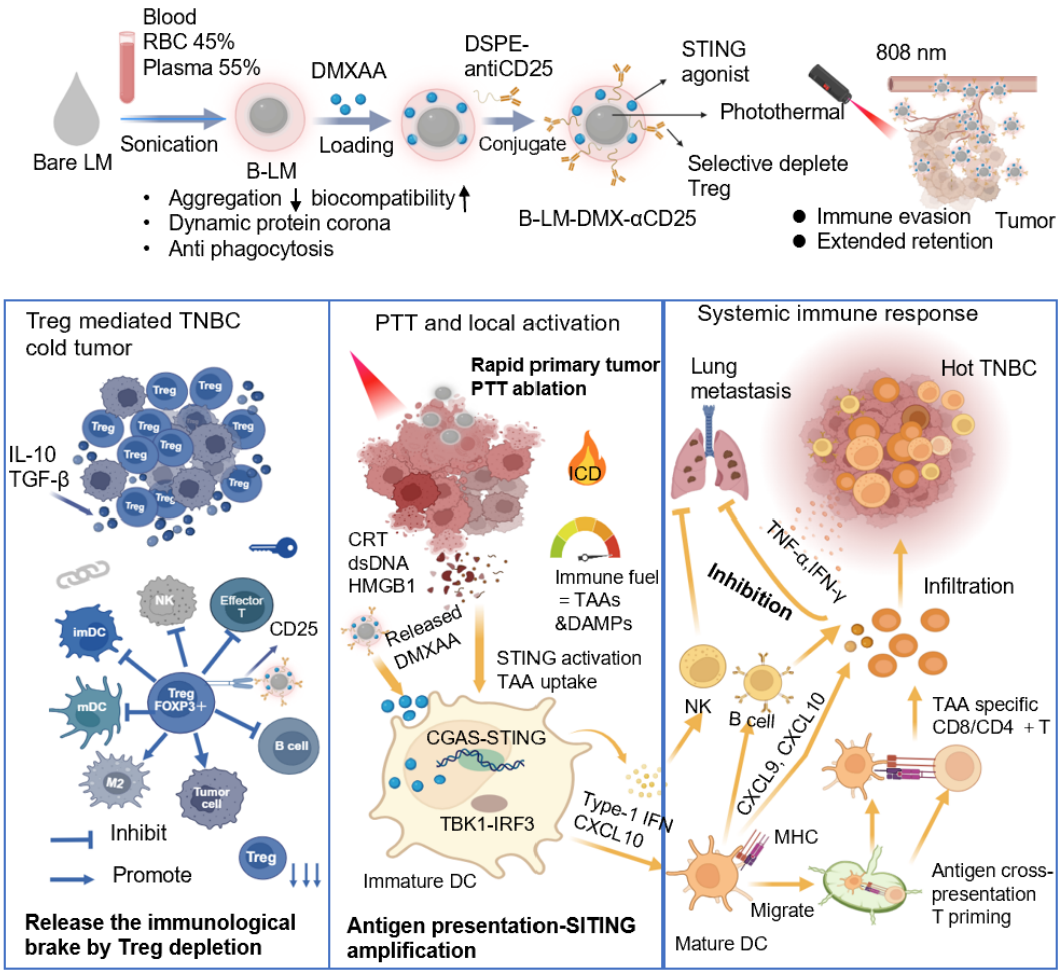

Figure 4.14 Schematic illustration of the B–LM–DMXAA–αCD25 nanoplatform for photothermal immunotherapy of TNBC.

Liquid metal (LM) nanoparticles were camouflaged with whole-blood components through sonication to form B–LM, exhibiting improved colloidal stability, biocompatibility, and enhanced tumor targeting. Subsequent loading of the STING agonist D DMXAA loading and conjugation with anti-CD25 antibodies produced multifunctional B–LM–DMXAA–αCD25 nanocomposites with selective Treg-depleting capability and STING-activating ability. Upon 808 nm laser irradiation, the nanoplatform achieved rapid photothermal ablation of primary TNBC tumors, accompanied by robust immunogenic cell death (ICD) and abundant release of tumor-associated antigens (TAAs). Taking advantage of this antigen availability, the released DMXAA activated the STING–TBK1–IRF3 pathway, inducing type-I interferon secretion, promoting dendritic-cell maturation, and enhancing cross-presentation to effectively prime TAA-specific T cells. By integrating Treg depletion, PTT-

induced ICD, and STING activation, the B–LM–DMXAA–αCD25 nanocomposite effectively "released the immunological brake," amplified antigen presentation, and remodeled the Treg mediated immunosuppressive cold TNBC into an immune-responsive, hot tumor microenvironment. This cascade immune activation elicited a potent systemic antitumor response, stimulating cytotoxic T-lymphocyte, NK-cell, and B-cell activity, thereby suppressing lung metastasis and preventing tumor recurrence.

4.6 Reference

[1] M.-Y. C. Polley, R. A. Leon-Ferre, S. Leung, A. Cheng, D. Gao, J. Sinnwell, H. Liu, D. W. Hillman, A. Eyman-Casey, J. A. Gilbert, *Breast Cancer Res. Treat.* **2021**, *185*, 557.

[2] D. C. Rigiracciolo, N. Nohata, R. Lappano, F. Cirillo, M. Talia, D. Scordamaglia, J. S. Gutkind, M. Maggiolini, *Cells.* **2020**, *9*, 1010.

[3] P. Zagami, L. A. Carey, *NPJ breast cancer.* **2022**, *8*, 95.

[4] R. Dent, M. Trudeau, K. I. Pritchard, W. M. Hanna, H. K. Kahn, C. A. Sawka, L. A. Lickley, E. Rawlinson, P. Sun, S. A. Narod, *Clin. Cancer Res.* **2007**, *13*, 4429.

[5] S. Reddy, C. Barcenas, A. Sinha, L. Hsu, S. Moulder, D. Tripathy, G. Hortobagyi, V. Valero, *Br. J. Cancer.* **2018**, *118*, 17.

[6] D. O'Reilly, M. Al Sendi, C. M. Kelly, *World J. Clin. Oncol.* **2021**, *12*, 164.

[7] T. E. Keenan, S. M. Tolaney, *J. Natl. Compr. Canc. Netw.* **2020**, *18*, 479.

[8] R. Nanda, L. Q. Chow, E. C. Dees, R. Berger, S. Gupta, R. Geva, L. Pusztai, K. Pathiraja, G. Aktan, J. D. Cheng, *J. Clin. Oncol.* **2016**, *34*, 2460.

[9] S. Adams, P. Schmid, H. Rugo, E. Winer, D. Loirat, A. Awada, D. Cescon, H. Iwata, M. Campone, R. Nanda, *Ann. Oncol.* **2019**, *30*, 397.

[10] S. Adams, S. Loi, D. Toppmeyer, D. Cescon, M. De Laurentiis, R. Nanda, E. Winer, H. Mukai, K. Tamura, A. Armstrong, *Ann. Oncol.* **2019**, *30*, 405.

[11] J. Cortés, O. Lipatov, S.-A. Im, A. Gonçalves, K. Lee, P. Schmid, K. Tamura, L. Testa, I. Witzel, S. Ohtani, *Ann. Oncol.* **2019**, *30*, v859.

[12] C. Denkert, G. von Minckwitz, S. Darb-Esfahani, B. Lederer, B. I. Heppner, K. E. Weber, J. Budczies, J. Huober, F. Klauschen, J. Furlanetto, *The lancet oncology.* **2018**, *19*, 40.

[13] M. D. Burstein, A. Tsimelzon, G. M. Poage, K. R. Covington, A. Contreras, S. A. Fuqua, M. I. Savage, C. K. Osborne, S. G. Hilsenbeck, J. C. Chang, *Clin. Cancer Res.* **2015**, *21*, 1688.

[14] L. Zhang, X. I. Wang, J. Ding, Q. Sun, S. Zhang, *Ann. Diagn. Pathol.* **2019**, *40*, 143.

[15] L. Fiori Lopes, R. Losi Guembarovski, A. L. Guembarovski, M. Okuyama Kishima, C. Z. Campos, J. M. M. Oda, C. B. Ariza, K. B. de Oliveira, S. D. Borelli, M. A. E. Watanabe, *BioMed research international.* **2014**, *2014*, 341654.

[16] W. Tan, W. Zhang, A. Strasner, S. Grivennikov, J. Q. Cheng, R. M. Hoffman, M. Karin, *Nature.* **2011**, *470*, 548.

[17] G. J. Bates, S. B. Fox, C. Han, R. D. Leek, J. F. Garcia, A. L. Harris, A. H. Banham, *J. Clin. Oncol.* **2006**, *24*, 5373.

[18] X. Yao, X. Niu, K. Ma, P. Huang, J. Grothe, S. Kaskel, Y. Zhu, *Small.* **2017**, *13*, 1602225.

[19] A. Espinosa, R. Di Corato, J. Kolosnjaj-Tabi, P. Flaud, T. Pellegrino, C. Wilhelm, *ACS nano.* **2016**, *10*, 2436.

[20] H. Yan, W. Shang, X. Sun, L. Zhao, J. Wang, Z. Xiong, J. Yuan, R. Zhang, Q. Huang, K. Wang, *Adv. Funct. Mater.* **2018**, *28*, 1705710.

[21] D. Gancberg, A. Di Leo, F. Cardoso, G. Rouas, M. Pedrocchi, M. Paesmans, A. Verhest, C.

Bernard-Marty, M. Piccart, D. Larsimont, *Ann. Oncol.* **2002**, *13*, 1036.

[22] C. Song, H. Phuengkham, Y. S. Kim, V. V. Dinh, I. Lee, I. W. Shin, H. S. Shin, S. M. Jin, S. H. Um, H. Lee, *Nat. Commun.* **2019**, *10*, 3745.

[23] N. Sang, S. Iwata, Y. Qi, E. Miyako, *Advanced Composites and Hybrid Materials.* **2025**, *8*, 1.

[24] H.-R. Jia, Y.-X. Zhu, X. Liu, G.-Y. Pan, G. Gao, W. Sun, X. Zhang, Y.-W. Jiang, F.-G. Wu, *ACS nano.* **2019**, *13*, 11781.

[25] D. V. Krysko, A. D. Garg, A. Kaczmarek, O. Krysko, P. Agostinis, P. Vandenabeele, *Nat. Rev. Cancer.* **2012**, *12*, 860.

[26] D. S. Chen, I. Mellman, *Immunity.* **2013**, *39*, 1.

[27] L. Motedayen Aval, J. E. Pease, R. Sharma, D. J. Pinato, *Journal of clinical medicine.* **2020**, *9*, 3323.

[28] L. Corrales, L. H. Glickman, S. M. McWhirter, D. B. Kanne, K. E. Sivick, G. E. Katibah, S.-R. Woo, E. Lemmens, T. Banda, J. J. Leong, *Cell Rep.* **2015**, *11*, 1018.

[29] M. Fu, Y. Shen, H. Zhou, X. Liu, W. Chen, X. Ma, *Journal of Materials Science & Technology.* **2023**, *142*, 22.

[30] W. Xie, F.-M. Allioux, J. Z. Ou, E. Miyako, S.-Y. Tang, K. Kalantar-Zadeh, *Trends Biotechnol.* **2021**, *39*, 624.

[31] Y. Hao, J. Gao, Y. Lv, J. Liu, *Adv. Funct. Mater.* **2022**, *32*, 2201942.

[32] S. A. Chechetka, Y. Yu, X. Zhen, M. Pramanik, K. Pu, E. Miyako, *Nat. Commun.* **2017**, *8*, 15432.

[33] D. Wang, X. Wang, W. Rao, *Acc. Mater. Res.* **2021**, *2*, 1093.

[34] E. Miyako, *Acc. Mater. Res.* **2021**, *2*, 858.

[35] Q. Yun, A. Kimura, M. Taguchi, E. Miyako, *Appl. Mater. Today.* **2022**, *26*, 101302.

[36] Y. Yu, E. Miyako, *Chemistry – A European Journal.* **2018**, *24*, 9456.

[37] J. J. Hu, M. D. Liu, F. Gao, Y. Chen, S. Y. Peng, Z. H. Li, H. Cheng, X. Z. Zhang, *Biomaterials.* **2019**, *217*, 119303.

[38] P. Zhu, S. Gao, H. Lin, X. Lu, B. Yang, L. Zhang, Y. Chen, J. Shi, *Nano Lett.* **2019**, *19*, 2128.

[39] Q. Xia, Y. Zhang, Z. Li, X. Hou, N. Feng, *Acta Pharmaceutica Sinica B.* **2019**, *9*, 675.

[40] Q. Jiang, Z. Luo, Y. Men, P. Yang, H. Peng, R. Guo, Y. Tian, Z. Pang, W. Yang, *Biomaterials.* **2017**, *143*, 29.

[41] G. Schwoch, H. Passow, *Mol. Cell. Biochem.* **1973**, *2*, 197.

[42] H. Liu, Y. Y. Su, X. C. Jiang, J. Q. Gao, *Drug delivery and translational research.* **2023**, *13*, 716.

[43] S. Fulda, A. M. Gorman, O. Hori, A. Samali, *Int. J. Cell Biol.* **2010**, *2010*, 214074.

[44] L. Pirkkala, P. Nykänen, L. Sistonen, *FASEB J.* **2001**, *15*, 1118.

Chapter 5 General conclusion and future scope

5.1 Overall summary

Cancer remains one of the greatest challenges to human health. Conventional therapeutic approaches, including surgery, radiotherapy, and chemotherapy, often fail to achieve complete tumor eradication and may lead to drug resistance, severe side effects, or even tumor progression. In recent years, PTT has emerged as a highly promising alternative strategy owing to its superior selectivity, high efficiency, low systemic toxicity, minimal side effects, and cost-effectiveness. Carbon-based and LM materials have attracted considerable attention in nanomedicine due to their strong absorption in the visible–near-infrared region, excellent photothermal stability, and good biocompatibility. However, these materials tend to aggregate in aqueous media and, as exogenous substances, are prone to rapid clearance by the reticuloendothelial system (RES) and antibody-mediated immune responses, thereby limiting their clinical translation. The introduction of functionalized cell membranes provides an effective solution: by inheriting the complex surface proteome of natural cell membranes from different biological sources, inorganic nanomaterials can acquire immune evasion, prolonged circulation, and enhanced tumor accumulation capabilities, enabling precise drug delivery, controlled release, and immune activation. Moreover, although immunotherapy has become a crucial strategy in recent years, the complex immunosuppressive TME often hinders the effective activation and infiltration of cytotoxic T lymphocytes, thereby limiting the efficacy of monotherapies. Therefore, the construction of nano platforms integrating photothermal and immunotherapeutic modalities offers a promising approach to overcome these limitations,

achieving enhanced tumor ablation while suppressing recurrence and metastasis.

This dissertation systematically investigates the in vitro and in vivo antitumor effects and mechanisms of three functionalized biomimetic nanoplatforms based on carbon nano horn and liquid metals.

In **Chapter 2**, a tumor cell membrane–functionalized carbon nanotube nanoplatform loaded with paclitaxel (PTX–CNH–CM) was successfully constructed via a one-step ultrasonication method for the treatment of colon carcinoma in mice. The homologous membrane coating endowed the platform with tumor-specific targeting ability, enabling efficient tumor accumulation and precise PTX delivery, thereby enhancing photothermal ablation efficacy. The inherent immunogenicity of the tumor membrane further stimulated an antitumor immune response. Experimental results confirmed that PTX–CNH–CM exhibited excellent water dispersibility, high photothermal conversion efficiency, and efficient cellular uptake. In vivo, under laser irradiation, PTX–CNH–CM achieved specific tumor accumulation, complete tumor eradication, and rapid wound healing. Meanwhile, multiple immune cells—including T cells, B cells, and NK cells—were activated, and TNF-α secretion was significantly increased, demonstrating the immunostimulatory potential of this biomimetic platform.

In **Chapter 3**, to further enhance the immunotherapeutic potency of photothermal nanoplatforms, a bacteria-membrane-coated LM nanocomplex (Lacto–LM) was developed via a facile sonication process using *Lactococcus* membranes derived from tumor tissue. This strategy not only improved the aqueous stability of LM but also introduced PAMPs on the nanoparticle surface, thereby augmenting immunogenicity. In Vivo studies demonstrated

efficient tumor accumulation and potent photothermal tumor ablation. Mechanistic investigations revealed significant upregulation of CRT exposure and HMGB1 release, elevated proinflammatory cytokine secretion, and dense infiltration of $CD11c^+$ dendritic cells, $perforin^+$/granzyme B^+ $CD8^+$ cytotoxic T cells, and $CD4^+$ helper T cells within the TME. These findings indicate that bacterial PAMPs, tumor-derived antigens, and PTT-induced ICD synergistically triggered robust innate and adaptive immune activation. Furthermore, tumor rechallenge experiments showed that mice cured by Lacto–LM treatment developed strong immunological memory, evidenced by increased $CD127^+$ memory T cells and $CD27^+$ memory B cells, and displayed complete resistance to tumor recurrence. Thus, Lacto–LM not only eliminated primary tumors but also reprogrammed the immunosuppressive TME, establishing durable immune memory to prevent relapse and metastasis.

Given the complexity of the tumor immune microenvironment, achieving optimal therapeutic efficacy requires not only activating antitumor immunity but also suppressing immunosuppressive cells within tumors. In **Chapter 4**, targeting the highly immunosuppressive triple-negative breast TNBC model characterized by abundant Tregs, a blood-membrane-coated LM nanoplatform co-loaded with the STING agonist DMXAA and anti-CD25 antibody (B–LM–DMX–αCD25) was constructed. The blood-derived membrane coating effectively reduced macrophage uptake, prolonged circulation, and enabled immune evasion. Meanwhile, αCD25 enabled selective depletion of Tregs, while DMXAA amplified PTT-induced ICD and tumor antigen release, collectively activating systemic immune cascades. In vivo results showed that under laser irradiation, B–LM–DMX–αCD25 induced rapid and complete regression of orthotopic TNBC tumors without recurrence. Mechanistically, this

platform significantly reduced FOXP3$^+$ Tregs, promoted DC maturation and proliferation, enhanced TAA cross-presentation, and triggered the activation and tumor infiltration of TAA-specific CD8$^+$ cytotoxic T lymphocytes. Moreover, Treg depletion and upregulation of IFN-β and CXCL10 further facilitated B and NK cell recruitment, establishing a potent and coordinated immune network. Consequently, the immunosuppressive TME was successfully reprogrammed into an immune-active state ("cold-to-hot" transformation). This synergistic strategy—combining photothermal ablation, STING activation, and Treg depletion—not only achieved complete elimination of primary TNBC but also effectively inhibited lung metastasis and markedly prolonged survival.

5.2 Outlook

The three biomimetic nanoplatforms developed in this study—based on homologous targeting, bacterial-membrane immune activation, and immunosuppressive microenvironment modulation—collectively validate the great potential of photothermal–immunotherapy for precise cancer treatment and immune regulation. Although the photothermal therapeutic efficacy of carbon nanotubes and liquid metal materials has been clearly demonstrated, further studies are required to comprehensively elucidate their pharmacokinetics, in vivo metabolic pathways, and biodistribution of carbon and LM elements across organs. Such investigations will be crucial to confirming the metabolic safety of these nanoplatforms and establishing a solid foundation for their future clinical translation.

This research can be further deepened and expanded in several aspects. First, in terms of material design, continuous efforts should be devoted to developing novel biomimetic

membrane materials and exploring the functionalization of nanocarriers with membranes derived from various cell sources—such as stem cells or immune cells—or even genetically engineered membranes. Such strategies could further enhance tumor-targeting efficiency while enabling in situ activation of long-lasting antitumor immunity. Meanwhile, the construction of multi-responsive and biodegradable "green" nanostructures is essential to improve therapeutic safety and clinical translatability.

Moreover, future studies should integrate multi-omics analyses with multimodal imaging technologies to systematically elucidate the dynamic processes of photothermal–immunotherapy across molecular, cellular, and systemic levels. For example, single-cell sequencing, spatial transcriptomics, and mass cytometry can be applied to trace the temporal and spatial evolution of immune cells within the tumor microenvironment, thereby revealing their activation, differentiation, and memory formation mechanisms following immunogenic cell death (ICD). Simultaneously, multimodal imaging techniques—such as photoacoustic imaging, near-infrared fluorescence imaging, and magnetic resonance imaging—can enable real-time monitoring of nanoparticle biodistribution, local temperature elevation, and immune-cell infiltration, thus providing data support for dynamic and personalized treatment optimization.

Furthermore, artificial intelligence can be leveraged to establish a digital tumor model that integrates patients multi-omics profiles, imaging characteristics, and immunological indicators. This model can simulate and predict the therapeutic efficacy of different nanomaterial combinations and immunotherapeutic regimens, thereby enabling precise prediction and

personalized optimization of photothermal–immunotherapy. Such an approach will facilitate the transition of this field from empirical exploration toward a systematic, controllable, and precision-driven paradigm in nanomedicine.

List of publications

Publications related to this dissertation

- **Sang N**, Qi Y, Nishimura S, et al. Biomimetic functional nanocomplexes for photothermal cancer chemoimmunotheranostics[J]. Small Science, **2024**, 4(10): 2400324. (Chapter 2)
- **Sang N** Iwata S, Qi Y, et al. Bacterial-adjuvant liquid metal nanocomposites for synergistic photothermal immunotherapy[J]. Advanced Composites and Hybrid Materials, **2025**, 8(5): 1-21. (Chapter 3)
- Other publications

- Chintalapati, S., **Sang, N**., Miyahara, M., Iwata, S., Nishida, K., & Miyako, E. (2025). Living drugs: A wonderful evolution for therapeutic applications. *Cell Biomaterials*.

Presentation

- Biomimetic functional nanocomplexes for photothermal cancer chemo-immunotheranostics. Best Poster Award, International Symposium on Exponential Biomedical DX 2024 (eMEDX-24)| Ishikawa, Japan, December 19th – 20th 2024
- Biomimetic functional nanocomplexes for photothermal cancer chemo-immunotheranostics. Materials Research Meeting 2025 (MRM)| Yokohama, Japan, December 11th-13th 2025

Acknowledgements

I would like to express my deepest gratitude to my supervisor, Professor Miyako, for his invaluable guidance, continuous encouragement, and generous support throughout my doctoral journey. It has been a great privilege and fortune to work with him and to be one of his students. His profound knowledge, inspiring vision, and rigorous attitude toward scientific research have been a constant source of motivation and enlightenment. I truly appreciate his patience, insightful discussions, and the freedom he has given me to explore and develop my research ideas. Without his mentorship, this dissertation would not have been possible.

I am also sincerely grateful to my second supervisor, Prof. Dr. Kazuaki Matsumura, and my minor supervisor, Prof. Dr. Takumi Yamaguchi, for their helpful advice and thoughtful guidance. Their suggestions and perspectives greatly enriched my research and guided me through many challenges during my PhD journey.

I would also like to extend my heartfelt thanks to all the members of our laboratory for their warm collaboration, technical assistance, and the pleasant working atmosphere they have created. The stimulating academic discussions and the countless hours we spent together in experiments have greatly enriched both my knowledge and my personal growth. I also appreciate the friendship and support from my friends at JAIST, which made my PhD life both productive and memorable.

Finally, my heartfelt thanks go to my parents for their unconditional love, endless understanding, and unwavering support throughout my studies and life. Their sacrifices, encouragement, and faith have always been my greatest strength and motivation to overcome

every challenge along the way.